

**Section Physics of Nuclear Reactors
Department Radiations, Radionuclides and Reactors
Faculty of Applied Sciences
Delft University of Technology
Mekelweg 15, 2629 JB Delft
The Netherlands**

The Liquid Salt Pebble Bed Reactor
A new high-temperature nuclear reactor

S.J. de Zwaan

PNR-131-2005-008

November 2005

Foreword

This report presents the final thesis of the Master of Science program in Applied Physics at the Delft University of Technology, performed at the section Physics of Nuclear Reactors of the faculty of Applied Sciences.

I would like to thank Brian Boer and Jan Leen Kloosterman for their guidance during the final stage of my master program, Danny Lathouwers for his help and guidance handling the code HEAT, Wilfred van Rooijen for answering many questions concerning SCALE and PERL and all other members of the section Physics of Nuclear Reactors for their inspiration and support.

I would also like to thank all people who helped and encouraged me in creating this thesis.

Sieuwert de Zwaan

Delft, November 2005

Summary

Several new nuclear power plants are currently being developed to be highly economical, to be passive (or inherently) safe, to produce a minimal waste, to be proliferation resistant and that to be able to produce hydrogen. A new reactor design, the Advanced High Temperature Reactor (AHTR), has recently been presented. It is a high temperature liquid salt cooled nuclear reactor with prismatic fuel blocks. The liquid salt coolant has excellent heat transfer properties. This provides several benefits, as lower maximum fuel temperatures, higher coolant outlet temperatures, increased core power density and increased total power due to increased decay heat removal capacity. However, reshuffling of the fuel, refueling and maintenance of the vessel needs to be done off-line at high temperatures to prevent the liquid salt coolant from freezing. A pebble bed system allows on-line refueling and reshuffling. This is a great advantage, since refueling will be easier and operation costs can be reduced. In return, a pebble bed has a restriction with regards to the coolant/fuel ratio.

In order to benefit from the on-line refueling capability of a pebble bed the Liquid Salt Pebble Bed Reactor (LSPBR) is proposed, a high temperature pebble bed reactor with liquid salt cooling. The fuel in this reactor is similar to the existing HTR pebble fuel. The objective of this thesis is to make a preliminary design for the LSPBR and to investigate its design possibilities by analysis of core physics and thermal hydraulics of the reactor core. This thesis includes an investigation on four different subjects: namely a selection of the preferred salt for the LSPBR, dimensioning of the reactor core, steady state performance and decay heat removal.

A selection for the first candidate liquid salt coolant in the LSPBR was made based on the effects of the coolant on the reactor neutronics. The liquid salt best fit to the LSPBR is LiF-BeF_2 . Among all the candidate salts it has the highest moderating ratio, the largest k -infinity values, a negative voiding reactivity coefficient and the strongest total temperature coefficient.

A preliminary design of the LSPBR was made. Two designs were proposed: an annular shaped core and a cylindrical shaped core. From the dimensioning investigations it was found that the size of the pebble bed core is not restricted by its pressure drop. Restrictions will be the ability to remove heat from the reactor core and the maximum available vessel size.

In order to investigate the temperatures and power profile in the proposed designs, steady state calculations were performed. These calculations consist of coupled thermal hydraulics and neutronics calculations. It was found that the flux profiles have their maximum in the center of the core and that the power density is largest in the center. Because the radial flux profile is more flat for the annular core, a lower maximum power density and a lower maximum fuel temperature is found in the annular core. Therefore, the annular core is the preferred shape for the LSPBR.

Finally, calculations were performed to investigate the capability to remove the decay heat in a loss of forced cooling accident. The maximum allowable power that can be produced with the LSPBR is hereby determined. When an additional salt plenum is added to the reactor core, extra thermal inertia is introduced. This leads to improved decay heat removal and higher permissible nominal powers. From decay heat removal calculations performed with HEAT, it was found that the maximum nominal power is 2000 MW without salt plenum and 4000 MW with salt plenum.

Contents

FOREWORD	I
SUMMARY	IV
CONTENTS	VI
1 INTRODUCTION	1
1.1 HIGH TEMPERATURE REACTORS.....	1
1.2 THE ADVANCED HIGH TEMPERATURE REACTOR (AHTR).....	3
1.3 OBJECTIVES OF THE THESIS AND SCOPE.....	9
2 SELECTION OF THE LIQUID SALT COOLANT	10
2.1 LIQUID SALT COOLANT CANDIDATES.....	10
2.1.1 <i>The void coefficient</i>	11
2.1.2 <i>Moderating power of the selected salts</i>	11
2.1.3 <i>Natural ⁶Li and Transmutation of Beryllium to ⁶Lithium during operation</i>	12
2.2 CALCULATIONS OF LIQUID SALT EFFECTS ON REACTIVITY.....	13
2.2.1 <i>K_∞ as a function of the moderator-fuel ratio and voiding of liquid salt coolant</i>	13
2.2.2 <i>K_∞ as a function of fuel and coolant temperature</i>	14
2.2.3 <i>K_∞ as a function of the packing fraction</i>	15
2.2.4 <i>Calculation scheme</i>	17
2.3 RESULTS OF LIQUID SALT REACTIVITY CALCULATIONS.....	18
2.3.1 <i>K_∞ as a function of 1/HM per pebble</i>	18
2.3.2 <i>Effect of liquid salt voiding on K_∞</i>	20
2.3.3 <i>K_∞ as a function of fuel temperature</i>	22
2.3.4 <i>K_∞ as a function of fuel and coolant temperature (Doppler and voiding combined)</i>	22
2.3.5 <i>K_∞ as a function of the packing fraction</i>	24
2.4 CONCLUSIONS ON SELECTION OF THE LIQUID SALT COOLANT.....	25
3 THE LIQUID SALT PEBBLE BED REACTOR (LSPBR)	27
3.1 FUEL.....	27
3.2 DIMENSIONING THE LSPBR.....	28
3.2.1 <i>Pressure drop</i>	28
3.2.2 <i>Maximum power</i>	30
3.2.3 <i>Core shape</i>	31
3.3 LSPBR PRECONCEPTUAL DESIGN PARAMETERS.....	31
4 STEADY STATE CALCULATIONS, THE LSPBR DURING NORMAL OPERATION	33
4.1 THERMIX EVENT COUPLING.....	33
4.2 STEADY STATE INPUT ANNULAR & CYLINDRICAL CORE.....	35
4.3 STEADY STATE RESULTS FOR THE CYLINDRICAL CORE SHAPE.....	37
4.3.1 <i>Flux profiles</i>	38
4.3.2 <i>Power density profiles</i>	40
4.3.3 <i>Temperature profiles</i>	41
4.3.4 <i>Comparison of steady state results with the AHTR</i>	42
4.4 CONCLUSIONS ON THE STEADY STATE CALCULATIONS.....	44
5 DECAY HEAT REMOVAL	46
5.1 DECAY HEAT CALCULATION METHODS.....	46
5.1.1 <i>Calculation of decay heat with decay heat groups (used in HEAT)</i>	46
5.1.2 <i>Analytical calculation of power profile in HEAT</i>	47

5.2	THERMAL HYDRAULICS CODE HEAT	48
5.2.1	<i>(Lack of) heat transport between coolant and reflector in THERMIX</i>	49
5.3	DECAY HEAT REMOVAL CALCULATION INPUT	49
5.4	RESULTS OF DECAY HEAT CALCULATIONS	52
5.4.1	<i>Results from decay heat calculations with original THERMIX input</i>	52
5.4.2	<i>Results of THERMIX and HEAT comparison calculations</i>	52
5.4.3	<i>HEAT results decay heat calculation pebble bed</i>	55
5.4.4	<i>Detailed results for 2000 MW initial power</i>	56
5.4.5	<i>HEAT results for the pebble bed reactor core with additional salt plenum</i>	60
5.4.6	<i>Comparison of the results for 2000 MW of both cases (with & without salt plenum)</i>	64
5.4.7	<i>Comparison of the HEAT results for 2400 MW with salt plenum with results from AHTR</i> ..	65
5.5	CONCLUSIONS ON THE DECAY HEAT REMOVAL CALCULATIONS	68
6	CONCLUSIONS	70
7	RECOMMENDATIONS	71
APPENDIX A, THE THERMAL HYDRAULICS CODE THERMIX		73
A.1	HEAT TRANSFER BY CONDUCTION, THE MAIN PROGRAM OF THERMIX	73
A.1.1	<i>Energy equations</i>	73
A.1.2	<i>The conductivity λ per region</i>	77
A.1.3	<i>Boundary Conditions Temperature Field Calculation</i>	78
A.2	CONVECTION PART OF THERMIX, FLOW FIELD AND CONVECTIVE HEAT SOURCES	79
A.2.1	<i>The (mass) flow field calculation</i>	80
A.2.2	<i>The Coolant temperatures, convective heat sources</i>	83
A.3	MODIFICATIONS OF THE SOURCE CODE OF THERMIX FOR THE APPLICATION OF LIQUID SALT COOLING	86
A.4	WAY-WIGNER DECAY HEAT CALCULATION (USED IN THERMIX)	87
APPENDIX B. EVEN PARITY NEUTRON TRANSPORT CODE EVENT		89
B.1	NEUTRON TRANSPORT EQUATION	89
B.2	DISCRETIZATIONS IN EVENT	90
B.2.1	<i>Multi group treatment</i>	90
B.2.2	<i>Time discretization</i>	90
B.2.3	<i>Angular discretization, spherical harmonics</i>	90
B.2.4	<i>Spatial discretization, finite elements</i>	91
B.3	SOLUTION PROCEDURE, EVEN PARITY METHOD	91
APPENDIX C. THE THERMAL HYDRAULICS CODE HEAT		93
C.1	MOMENTUM EQUATION USED IN HEAT	93
C.2	ENERGY EQUATIONS	94
C.3	HEAT BOUNDARY CONDITIONS	95
APPENDIX D, CROSS SECTIONS OF SALT CONSTITUENTS, MACROSCOPIC SCATTERING CROSS-SECTIONS OF CANDIDATE SALTS AND CARBON		97
APPENDIX E. THERMIX AND EVENT INPUT FOR THE CYLINDRICAL AND THE ANNULAR LSPBR		99
NOMENCLATURE		100
REFERENCES		102

1 Introduction

The demand for energy increases dramatically world wide. In the next 50 years the world population will expand from 6 to 9 billion people, all striving for a better quality of live. Especially in countries which are in early development like China and India energy consumption is expected to grow tremendously (Roadmap Generation IV, 2002).

Since the industrial revolution and the strong increase of the use of fossil fuels, especially coal and oil, the amount of greenhouse gases in the atmosphere has increased substantially. According to most scientists in the world, a global climate change is induced, which could have great consequences for biodiversity and civilizations.

Therefore, simply expanding energy production using today's mix of energy production options will continue to have potential long term consequences for global climate change. With carbon emissions threatening the very stability of the biosphere, the security of the world requires a massive transformation to cleaner energy supplies.

Among these clean supplies is nuclear energy. Nuclear energy has become an important factor in ensuring a secure clean energy supply now and will play an important role in the foreseeable future. Worldwide nuclear energy contributes for 16 % to the production of electricity, in Europe this share is even more than a third (Report on Green Paper, 2005). Renewable energy sources like solar, wind and biomass can help reducing emission and dependency on oil, but the contribution of these energy sources will remain modest. Nuclear fusion may once be an available option for energy production, but several obstacles stand in its way and therefore commercial production is decades away. Until now, nuclear energy is the only feasible energy production technique to satisfy the growing energy needs without further production of greenhouse gases.

Furthermore, nuclear energy can also be used to produce hydrogen. This could reduce the CO₂ emissions in the transport sector and the dependency on oil from politically unstable regions.

1.1 High Temperature Reactors

To continue the benefits from nuclear energy, new nuclear systems will be needed to replace plants as they retire. Several new nuclear power plants are currently developed (Generation IV or Next Generation Nuclear Power plants). Important goals in the new nuclear systems are that they should be highly economical, have enhanced safety systems as passive safety, produce a minimal waste and be proliferation resistant. To achieve the goals set for the next generation nuclear power plants (generation IV), earlier investigated reactor types have gained renewed interest. Several investigations are currently performed in High Temperature nuclear Reactors (HTRs).

Increased safety and efficiency

The next generation of nuclear reactors is being designed to be passively safe and to have high efficiency. Passive safety means that the reactor will automatically shutdown in case of an accident and remove heat inside the core without any active intervention from an operator.

Higher efficiency will lead to less waste per unit energy, reduced fuel consumption, less reject heat and improved economics. Power plant efficiency increases with temperature. This can be illustrated with the Carnot efficiency $\eta_{max} = 1 - T_C/T_H$, which is the maximum achievable efficiency in any power cycle between two thermal reservoirs at temperature T_H and T_C (Moran and Shapiro, 1998). Conventional power cycles will usually operate at ~60 % of the maximum achievable efficiency. Light Water Reactors (LWR's) deliver heat at ~300°C. High Temperature Reactors (HTR's) deliver heat at temperatures ranging from 700°C to 1000°C.

Hydrogen production

Another important goal for high-temperature reactors is hydrogen production. The use of hydrogen as a main energy carrier is promising, because the “combustion” of hydrogen in a fuel cell is efficient and without any negative by products. Decreased availability of light crude oils, with a corresponding increase use of heavy crude oils that need H₂ for conversion to gasoline, increases the worldwide demand of hydrogen. If the cost goals for automotive fuel cells are reached, the transportation section might ultimately be fuelled by H₂.

Hydrogen can be produced by processing fossil fuel or by processing water. The first option will always produce CO or CO₂ which is undesirable. Hydrogen can be produced from water with nuclear energy by electrolysis or using thermochemical (water splitting) cycles that require high temperatures to convert water into hydrogen and oxygen. At the most fundamental level, thermochemical production involves conversion of thermal energy to chemical energy stored in H₂ (Brown et. al. 2000), while electrolysis involves conversion of electricity to chemical energy. The additional conversion step adds costs and introduces additional inefficiencies (Forsberg et. al. 2004).

High Temperature Reactor types

For high temperature reactors different core geometries are possible. Different designs reflect different operational goals. The pebble bed core design allows online refueling by the slow movement of the pebbles through the reactor core, while hexagonal blocks allow wide latitude in the volumetric ratio of fuel, coolant and moderator. The optimal geometry of the fuel assembly will depend upon detailed design trade-offs between performance, fuel cost safety and other factors.

Several high temperature test reactors have been cooled with highly pressurized helium and were already built. The Arbeitsgemeinschaft Versuchreaktor Jülich (AVR) operated

in Jülich, Germany from 1967 to 1990, the Thorium High Temperature Reactor operated until 1989 in Hamm-Uentrop. These experimental reactors were both of the pebble bed type and cooled with helium.

Recently new helium cooled high temperature reactors are developed in Japan, China and South Africa. The construction of the 30 MW(t) High Temperature Test Reactor (HTTR) with hexagonal fuel blocks was successfully completed in 1987 by the Japan Atomic Research Institute (JAERI). The High-Temperature Reactor 10 MW(t) (HTR-10) with a pebble bed geometry is currently operational in China, and in South Africa the 110 MW(t) Pebble Bed Modular Reactor (PBMR) is under development (Boer, 2004). Similar to the PBMR is the Gas-Turbine Modular High-temperature Reactor (GT-MHR). It is being designed in the USA and Russia and has a prismatic core design. Other investigations currently performed into new (generation IV) gas cooled reactor concepts are the Gas Cooled Fast Reactor System (GCFR) which is highly sustainable because of the closed fuel cycle and the Very High Temperature Reactor which is highly economic because of its Hydrogen production efficiency (Roadmap Generation IV, 2002).

While high-pressure helium gas is the traditional coolant for high temperature nuclear reactors, there is also an option to cool high temperature nuclear reactor systems with low-pressure liquids. Molten Fluoride salts are the traditional low-pressure coolant in high temperature reactor systems with boiling points above the peak coolant temperatures. Also, compared to helium, liquid salts have far more superior heat transfer properties (comparable to those of water at 75 bar). This provides several potential benefits, as cooler maximum fuel temperatures, higher coolant outlet temperatures, increased core power density and increased total power by increased decay heat removal capacity.

Two experimental liquid salt cooled test reactors were built and successfully operated. The 2.5 MW(t) Aircraft Reactor Experiment (ARE) was the first Molten Salt Reactor, and operated in 1954 using a sodium-zirconium fluoride salt (NaF-ZrF_4). This was followed by the 1965 Molten Salt Reactor Experiment (MSRE), a 8 MW(t) reactor that used a lithium-beryllium fluoride salt (Li_2BeF_4 , which is referred to as FLiBe). In both reactors the nuclear fuel was dissolved in the salt. Because the Molten Salt Reactor's (MSR) high potential, the MSR is still being investigated. Recently, new research in the liquid salt cooled reactor has resulted in a new reactor concept, the AHTR (Forsberg, 2004), which is a high temperature reactor with solid fuel and a liquid salt coolant.

1.2 The Advanced High Temperature Reactor (AHTR)

The Oak Ridge National Laboratory (ORNL) has recently presented the Advanced High Temperature Reactor (AHTR), a design of a *liquid salt*-cooled nuclear reactor. This new concept has been developed by three participating organizations: Oak Ridge National Laboratory (ORNL), Sandia National Laboratories (SNL) and the University of California at Berkeley (UCB).

Because of the superior heat capacity and heat transport characteristics of molten salts compared to helium, a new design of a high temperature reactor with molten salt as the primary coolant was developed as an alternative to gas-cooled reactors for high temperature applications (efficient hydrogen and electricity production). The AHTR has been developed to reach the following goals (Forsberg et. al. 2004):

1. High temperatures hydrogen production, efficient energy (Brayton)
improved economics, less waste
2. Passive safety passive reactivity control, low pressure,
reduced operation cost, improved public acceptance
3. Large power output improved economics

In the following table, the preconceptual design parameters are shown of the reference AHTR.

Table 1. AHTR preconceptual design parameters

Power level	2400 MW(t)	Electrical output	1300MW(e)
Core inlet/outlet temperature	900 °C/ 1000 °C	Power cycle	3 stage multi reheat Brayton
Coolant	Li ₂ BeF ₄	Power cycle working fluid	Nitrogen (Helium long term option)
Mass flowrate	12070 kg/s	Core inlet pressure	0.230 MPa
Volumetric flow rate	5.54 m/s	Core outlet pressure	0.101 MPa
Channel diameter	0.95 cm	Pressure drop	0.129 MPa
Volume Fraction (core)	6.56 %	Core shape	Annular
Velocity	2.32 m/s	Core outer diameter	7.8 m
Fuel kernel	Uranium carbide/oxide	Core annulus	2.3 m
Enrichment	10.36 wt % ²³⁵ U	Core height	7.9 m
Form	Prismatic	Pumping power	716 kW
Block diameter	0.36 m (across flats)	Power density	8.3 MW/m ³
Block height	0.79 m	Reflector (outer)	138 columns
Columns	324	Reflector (inner)	55 columns
Mean temperature	1050 °C	Vessel diameter	9.2 m
Peak temperature	1168 °C	Vessel height	19.5 m
		Vessel thickness	10.0 cm

The reference primary liquid salt coolant is Li₂BeF₄ (FliBe), which was used in the MSR and related test loops. The volumetric heat capacity of FliBe is 4540 kJ/m³K, which is similar to that of water, four times that of sodium and more than 200 times that of helium at 70 bar (20 kJ/m³K). FliBe has a low vapor pressure; the melting point of FliBe lays at 459 °C, while its boiling point lays at 1430 °C. The reactor core is a pool type reactor, extra liquid salt is present inside the reactor vessel, in the top and bottom plenum. This salt introduces extra thermal inertia.

The AHTR uses the same TRISO coated fuel particles as used in helium-cooled nuclear reactors. Instead of incorporating the TRISO particles in graphite pebbles, the particles are incorporated into a graphite matrix fuel compact, which is loaded into a graphite matrix fuel assembly.

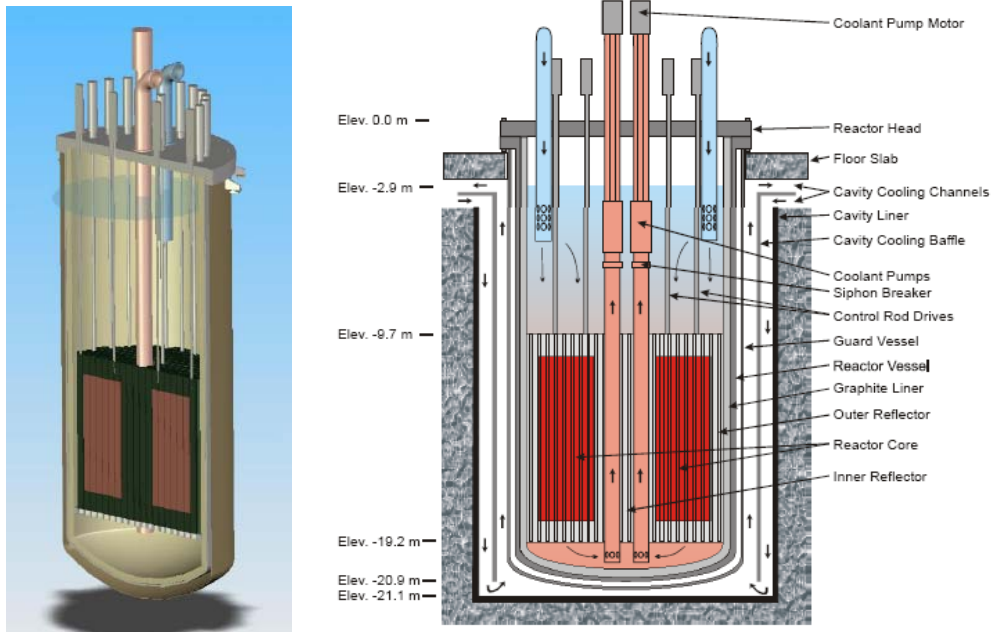


Figure 1. Left an impression model of the AHTR reactor vessel, right an elevated view of the AHTR core, vessels and internals.

The annular reactor core of the AHTR is designed with a hexagonal block (prismatic) fuel configuration and is similar to the GT-MHR core design. It was selected for the AHTR, in order to provide control of the fuel and coolant volume fractions and geometry. With a reactor vessel diameter of 9.2 m, a core configuration was selected that uses 324 fuel blocks and a power density of 8.3 MW/m^3 . At the top and bottom of the reactor core, reflector columns are placed.

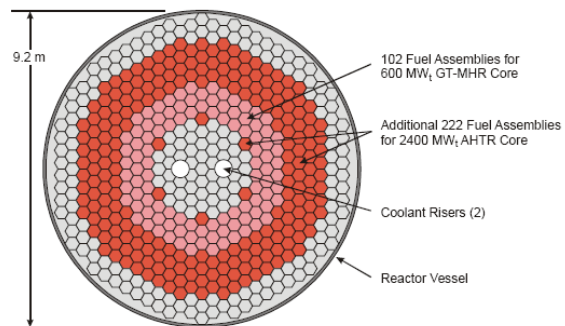


Figure 2. plan view of the annular AHTR core showing 324 columns of fuel assemblies and the inner and outer reflector columns.

The liquid salt coolant flows down the reactor core and up through a pair of central coolant risers. The vessel thickness is 10 cm, which is significantly less than the 22 cm of the GT-MHR vessel because of the low pressure of the liquid salt coolant of the AHTR compared with the high-pressure helium of the GT-MHR.

Steady state thermal hydraulics

For the AHTR an analysis of the steady state thermal hydraulics was made. It was expected that the superior thermal hydraulic qualities of the liquid salt coolant, as compared to a gas coolant, will lead to reduced temperature gradients inside the core and cooler fuel temperatures. The result of this analysis is shown in Figure 3, where a comparison of the axial centerline fuel and coolant temperatures is made of the 2400 MW AHTR and a design of the gas cooled 600 MW(t) next generation nuclear power plant

(NGNP) (both prismatic core designs). The figure shows as expected a lower temperature transient in the core for the AHTR and as well a lower fuel peak temperature.

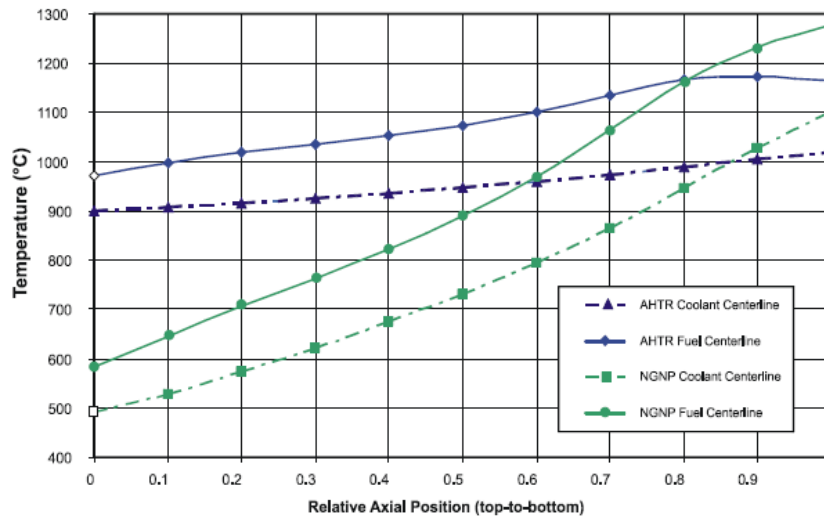


Figure 3. A comparison of the axial temperature profiles in the core of a 600MW(t) gas cooled Next Generation Nuclear Power plant (NGNP) design and the 2400 MW(t) AHTR (Forsberg et. al. 2004).

Decay heat removal

Passive safety is a key functional requirement for next generation nuclear power plants. The AHTR has the potential to provide such a robust safety case because of various inherent and passive safety characteristics. These characteristics include moderate core power densities, high temperature-margin fuel, a high thermal inertia core, efficient decay-heat removal and atmospheric pressure operation. The reactor power is intrinsically limited by the negative fuel temperature feedback (Doppler effect) (Forsberg et. al. 2004).

In a loss of forced cooling (LOFC) accident with scram, the thermal inertia of the reactor core and auxiliary cooling systems will remove the decay heat effectively. A LOFC accident with scram was simulated to determine the peak core temperature and the decay heat removal capacity of the natural circulating liquid salt and the auxiliary cooling systems. The results of the preliminary simulations are shown in Figure 4 and Figure 5. For this transient, the decay heat removal capacity exceeds the decay heat at approximately 35h and the peak core temperature is ~ 1160 °C and occurs approximately at 30h into the transient. During the transient the vessel temperature does not exceed 750°C. These preliminary results indicate that with passive decay heat removal and a cooling boiling point of 1430 °C there is a considerable safety margin for a LOFC accident. An additional calculation performed by the University of California at Berkeley for a 4000 MW(t) core yields a peak core temperature of 1325 °C, still more than 100 °C below the salt boiling limit (Forsberg et. al. 2004).

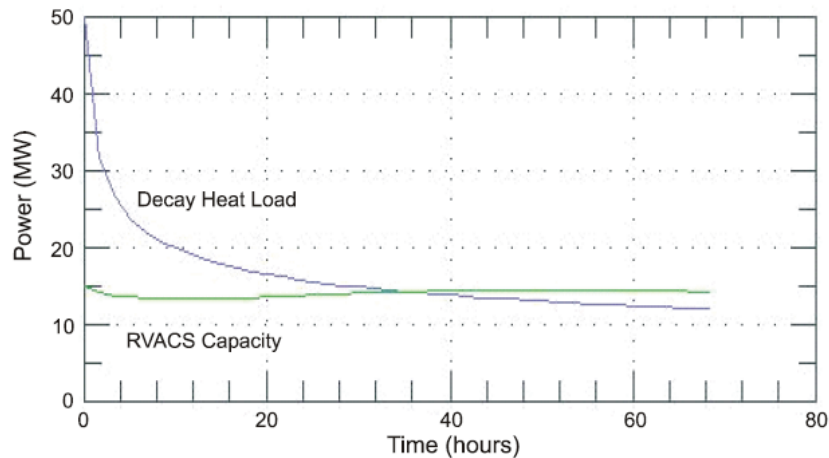


Figure 4. Comparison of the Reactor Vessel Auxiliary Cooling System (RVACS) decay heat removal capacity and heat load generated after a LOFC accident (with scram) (Forsberg et. al. 2004).

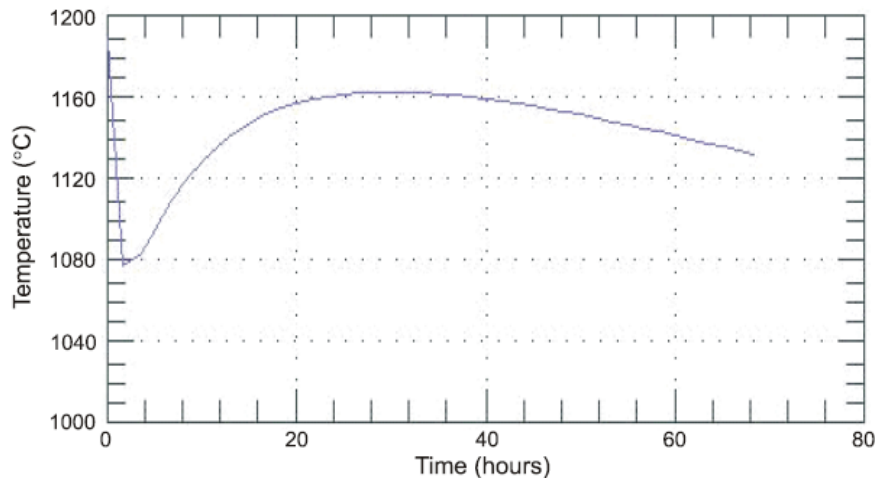


Figure 5. Maximum core temperature as a function of time after an LOFC accident (with scram) (Forsberg et. al. 2004).

In a beyond-design-basis accident, it's assumed significant failures (vessel failure etc.) have occurred and that any auxiliary cooling system has failed. To prevent catastrophic events the fuel temperature must be kept below failure temperature. Absorption of decay heat in the reactor and silo structure and transfer of decay heat through the silo walls to the environment will prevent these high temperatures.

In case of loss of decay heat cooling the reactor vessel will heat up, which ultimately can cause the vessel to fail. The molten salt coolant will fill the bottom of the silo while keeping the core flooded. The circulating salt will efficiently transfer the heat from the reactor core to the silo wall. When the salt reaches the silo wall it will freeze and unlike water cannot leak out the silo. Furthermore, no chemical reactions that generate gases or heat will occur. The silo wall consists of low cost thick steel rings that, following vessel failure will conduct heat to the earth and up the silo wall and distribute it above the coolant

salt layer. Near the top is an annular ring of a secondary solidified salt. As the temperature of the secondary salt increases, it will melt, flow into the silo and provide a significant source of thermal inertia.

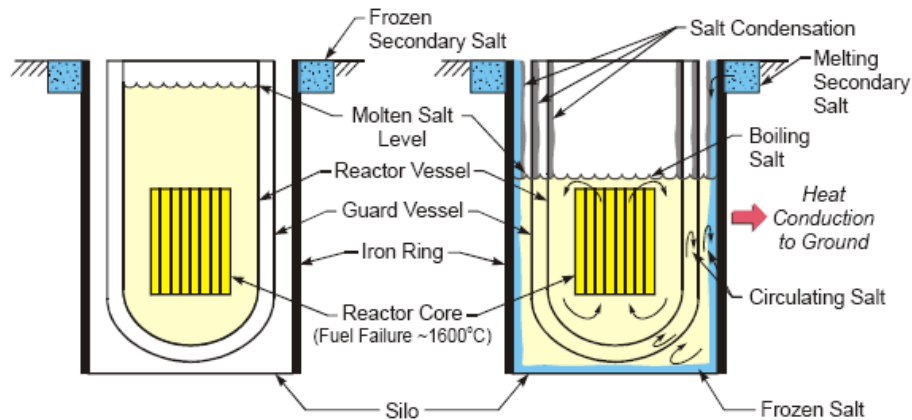


Figure 6. Normal and beyond-design-basis accident states for the AHTR

It can be concluded that the superior heat transfer coefficients for molten salts can lead to advantages over gas cooled reactors such as lower temperature differences between in- and outlet, low pressure, better decay heat removal and larger power output and therefore improved economics and high passive safety. There is great potential for high temperature liquid salt-cooled reactors. Molten salt can deliver heat for production of electricity and/or hydrogen production at high efficiencies.

Pebble bed and liquid salt?

The AHTR has a hexagonal prismatic core-geometry based on the GT-MHR core. This prismatic core design provides wide latitude in the volumetric ratio of fuel coolant and moderator. The control of the fuel and coolant volume fractions in this geometry is an advantage. However, reshuffling of the fuel, refueling and maintenance of the vessel needs to be done at very high temperatures. During a reactor stop the vessel needs to be opened and the fuel block must be taken out of the core for refueling or reshuffling. To prevent freezing of the liquid salt coolant, this has to be done at temperatures above the melting point of FLiBe (459°C). Although the liquid salt FLiBe is a transparent liquid, this is a difficulty which still is a large engineering challenge (Forsberg et. al. 2004).

A pebble bed system allows on-line refueling by the slow movement of pebbles through the reactor core. In a pebble bed reactor the core can also be reshuffled during operation by recycling of fuel pebbles. This is a great advantage, since refueling will be easier, operation costs will be reduced and reactor stops will be needed less. In return, the pebble bed has a restriction with regards to the coolant/fuel ratio. The coolant volume fraction in a pebble bed is fixed and around 37% (AHTR coolant volume fraction is 6.56 %). This has consequences for the volumetric flow rate and for the thermodynamics of the reactor. The question is: is this a problem?

1.3 Objectives of the Thesis and Scope

In order to benefit from both the on-line refueling capabilities of a pebble bed and the excellent heat transfer capabilities of the liquid salt, a Liquid-Salt-cooled Pebble Bed Reactor (LSPBR) is proposed. The objective of this thesis is to make a preliminary design for a Liquid Salt cooled Pebble Bed Reactor and to investigate its design possibilities by analysis of core physics and thermal hydraulics of the reactor core. The investigation can be split in four parts, namely:

- To make an investigation of different liquid salt coolants in a pebble bed reactor and make a selection of the liquid salt coolant to be used in the LSPBR. To obtain a stable system the liquid salt may not introduce a positive temperature reactivity coefficient. Which salt is best fit for the LSPBR?
- To make an investigation of the dimensioning of the LSPBR design. The size of a pebble bed is restricted by its pressure drop; a large pressure drop would require a large pumping power, which would reduce efficiency. Is the pressure drop a restriction for the LSPBR?
- To make an investigation of the reactor physics and thermodynamics in steady state operation by performing steady state calculations on the LSPBR. From steady state calculations temperature and power profiles can be obtained. Hot spots during operation can be localized. Also the effect of two core shapes is studied. Which core shape would be preferred, an annular core or a cylindrical core?
- To make an investigation of the capability of the reactor core to remove the decay heat in a Loss of Forced Cooling Accident, by performing Passive Decay Heat Removal simulations. With this investigation an answer can be found to the question what the maximum power is that can be produced.

The structure of this thesis will be as follows. The selection of the coolant will be handled in chapter 2. In this chapter k-infinity calculations are performed with different liquid salt coolant candidates in an infinite array of pebbles, to investigate the effect of temperature and voiding on the reactivity effects. The most important design features will be handled in chapter 3. In chapter 4 steady state calculations will be performed with the aid of the neutronics code EVENT and the thermal hydraulics code THERMIX. In this chapter the steady state results are compared with results from calculations performed on the AHTR. Also differences in reactor core shapes will be discussed. In chapter 5 decay heat removal calculations will be performed. The results acquired from THERMIX decay heat calculations will be compared with results from calculations performed with the decay heat thermal hydraulics code HEAT and with results from the AHTR. The conclusions of the thesis are given in chapter 6, followed by recommendations and future research opportunities in chapter 7. In the appendices additional information can be found about the thermal hydraulics code THERMIX, the neutronics code EVENT and the thermal hydraulics code HEAT.

2 Selection of the Liquid Salt Coolant

The selection of a liquid salt coolant depends on several aspects. Apart from good heat transfer coefficients, coolants must be chemically inert, have low toxicity, reasonably low melting points and high boiling temperatures. For the stability of the neutronics in the core it is also required that the presence of the liquid salt coolant does not lead to positive voiding or temperature reactivity effects. In this chapter an investigation is made of the effects of the liquid salt coolants on the neutronics in an infinite array of pebbles to make a selection for the first candidate liquid salt coolant in the LSPBR. Several salts are candidate.

2.1 Liquid Salt Coolant Candidates

Liquid salts were originally developed in the 1950's and 1960's for the Aircraft Propulsion Program (ARE) and the Molten Salt Reactor Experiment (MSRE). Since then, many salts have been examined. Several mixes of fluoride salts were selected for the Advanced High Temperature Reactor (AHTR) project by the Oakridge National Laboratory. Table 1 lists the salt mixtures that were selected as candidates for the LSPBR (Forsberg, 2004).

Table 2. physical properties of selected liquid salts

Salt (mol %)	Form. wt. (g/mol)	Melt. pt. (°C)	Density (g/cc), T(°C)	700°C Heat capacity (cal/g-°C)	Viscosity (cP), T(K)	Thermal cond. (W/cm-°C)
LiF-BeF ₂ (66-34)	33.1	458	2.28-4.88e-4*T	0.57	0.116exp(3755/T)	0.011
NaF-BeF ₂ (57-43)	44.1	360	2.27-3.7e-4*T	0.52	0.034exp(5164/T)	~0.01
LiF-NaF-KF (46.5-11.5-42)	41.2	454	2.53-7.3e-4*T	0.45	0.04exp(4170/T)	0.006-0.01
NaF-ZrF ₂ (50-50)	104.6	510	3.79-9.3e-4*T	0.28	0.071exp(4168/T)	~0.01 (est.)
NaF-KF-ZrF ₄ (10-48-42)	102.3	385	3.45-8.9e-4*T (est.)	0.26 (est.)	0.0061exp(3171/T) (est.)	~0.01
LiF-NaF-ZrF ₄ (42-29-29)	71.56	460	3.37-8.3e-4*T	0.35	0.0585exp(4647/T)	~0.01
NaF-NaBF ₄ (8-92)	104.4	385	2.252-7.11e-4*T	0.36	0.0877exp(2240/T)	~0.005

All candidate salts are fluoride salts. No chloride salts are candidates because of corrosive characteristics, high thermal-neutron absorption cross section and generation of ³⁶Cl, a long-lived radionuclide.

2.1.1 The void coefficient

The reactor core physics of the LSPBR is similar to that of a thermal HTR, because it uses the same fuel and moderator. Differences are expected, due to differences in the neutron cross-sections of the salt compared to helium. An anticipated difference is the coolant void coefficient of reactivity, since relevant nuclear cross sections of the liquid salts are larger than those of helium. The void coefficient corresponds to the amount of reactivity that is added or subtracted by complete removal of the coolant. To obtain a stable system a negative voiding reactivity effect is desirable.

The coolant salt will moderate and absorb neutrons. The amount of moderation depends on the scattering cross-section of the liquid salt and has a reactivity improving effect. Neutronic absorption is dependent on the neutron absorption cross-section and has a reactivity decreasing effect. The void coefficient (i.e. reactivity effect due to complete voiding) is dependent on the cross-sections of the coolant salt. When voiding occurs the reactivity will increase due to the reduced absorption and reactivity will decrease due to the reduced moderation. To obtain a negative void coefficient, the coolant should have a low absorption cross-section and a high scattering cross-section.

The microscopic cross-sections of the chosen salts as well as the macroscopic cross-sections can be seen in appendix D. Of the liquid salt coolant candidates, FliBe has the lowest absorption macroscopic cross-section and a relatively high scattering cross-section and is therefore possibly the best option to use in a thermal nuclear reactor.

2.1.2 Moderating power of the selected salts

The moderating quality of the selected salts can be quantified. The average logarithmic energy loss of a neutron with a nucleus (lethargy gain ξ) is given by (Duderstadt and Hamilton, 1976):

$$\xi = 1 - \frac{(A-1)^2}{2A} \ln\left(\frac{A+1}{A-1}\right) \quad (2.1)$$

Here A is the atomic mass number of the scattering material. The average number of collisions on average for a neutron of energy $E_0 = 2$ MeV required to be moderated to thermal energies, say 1 eV, can be estimated from

$$\langle no.collisions \rangle \approx \frac{\ln(E_0/E)}{\xi} = \frac{\ln\left(\frac{2 \cdot 10^6}{1.0}\right)}{\xi} \approx \frac{14.5}{\xi} \quad (2.2)$$

The lethargy gain ξ , which is a measure of moderating ability, decreases with the nuclide mass. The effectiveness of a nuclide in moderating a neutron also depends on the relative probability that a collision will result in a scattering reaction and not absorption of the

neutron. Therefore the figure of merit for moderating quality is the moderating ratio, defined as:

$$\text{Moderating ratio} = \frac{\xi \Sigma_s}{\Sigma_a} \quad (2.3)$$

Table 3. Slowing down parameters of typical moderators and selected salts

moderator	ξ	Number of collisions from 2 MeV to 1 eV	$\xi \Sigma_s$	Σ_a	$\xi \Sigma_s / \Sigma_a$
H	1	14	-	-	-
H ₂ O	.920	16	1.35	.019	71
C	.158	91	0.059	$4.1 \cdot 10^{-5}$	1437
He	.425	43	$1.6 \cdot 10^{-5}$	$1.9 \cdot 10^{-7}$	83
⁷ LiF-BeF ₂	.1046	139	0.026	$3.1 \cdot 10^{-4}$	83
NaF-BeF ₂	.0858	169	0.025	$1.2 \cdot 10^{-3}$	20
LiF-NaF-KF	.1057	137	0.016	$2.4 \cdot 10^{-3}$	6.8
NaF-ZrF ₄	.0809	179	0.021	$1.2 \cdot 10^{-3}$	18
NaF-KF-ZrF ₄	.0784	185	0.017	$2.0 \cdot 10^{-3}$	8.3
LiF-NaF-ZrF ₄	.0910	159	0.026	$1.2 \cdot 10^{-3}$	22
NaF-NaBF ₄	.1154	125	0.024	$1.0 \cdot 10^{-3}$	23

In Table 3 the mean lethargy gain ξ , the number of collisions to slow down a neutron from 2 MeV to 1 eV and the moderating ratio of the selected salts are tabulated together with other well known moderators. The average macroscopic cross-sections were calculated by averaging over the whole neutron energy spectrum (20 MeV-0.05 meV, 172 groups) of a thermal HTR (Duderstadt and Hamilton, 1976). LiF-BeF₂ has the highest moderating ratio of the selected salts.

2.1.3 Natural ⁶Li and Transmutation of Beryllium to ⁶Lithium during operation

Natural Lithium consists of 7.5 % ⁶Li and 92.5 % ⁷Li. ⁶Li has a large thermal neutron absorption cross-section ($\sigma_a = 940$ barn) (Pfennig, 1998). When Lithium is used in a coolant salt it is highly desirable to use ⁷Li only. It is difficult however to produce lithium with a ⁷Li content higher than 99.99%. Reducing the amount of ⁶Li would be highly desirable, but further reduction would not be helpful because of transmutation effects in the reactor, that produce ⁶Li during normal operation. During operation ⁶Li is formed by the ⁹Be(n, α)⁶He reaction with subsequent beta decay (in 806.7 ms) and ⁶Li is consumed by the ⁶Li(n, α)³H reaction. The ⁶Li concentration can therefore approximately be described with the following differential equation:

$$\frac{dN_{Li6}}{dt} = -\sigma_{a,Li6} \phi N_{Li6} + \sigma_{(n,\alpha)} \phi N_{Be9} \quad (2.4)$$

in this equation N_{Li6} is the ${}^6\text{Li}$ concentration, $\sigma_{a,Li6}$ the total absorption cross section of ${}^6\text{Li}$, $\sigma_{(n,\alpha)}$ the cross-section of ${}^9\text{Be}$ for a (n, α) reaction, N_{Be9} the ${}^9\text{Be}$ concentration (assumed constant) and ϕ is the neutron flux. The solution of this differential equation is

$$N_{Li6}(t) = \frac{\sigma_{(n,\alpha),Be9} \phi N_{Be9}}{\sigma_{a,Li6} \phi} \left(1 - e^{-\sigma_{a,Li6} \phi t}\right) + N_{Li6}(0) e^{-\sigma_{a,Li6} \phi t} \quad (2.5)$$

The equilibrium ${}^6\text{Li}$ concentration

$$N_{Li6}(eq.) = \frac{\sigma_{(n,\alpha),Be9} \phi N_{Be9}}{\sigma_{a,Li6} \phi} \quad (2.6)$$

was calculated to be 0.00073 % of the total Lithium concentration with a starting wt% of 0.01%. This agrees with calculations performed for the Reference AHTR at Oakridge National Laboratory. At 2400 MW(t), the equilibrium ${}^6\text{Li}$ concentration in the coolant was 0.001 wt% or about 10% of its initial concentration (Forsberg et. al. 2004). The time after the first startup until the equilibrium is reached depends on the power density and the amount of salt in the reactor system compared to the amount of salt in the core. It is estimated that, with a power density of 8.3 MW/m³ and a total amount of salt in the primary loop which is about twice the amount of salt in the core, the equilibrium can be reached in 200 days of production after the first startup of the reactor. During this period until equilibrium the ${}^6\text{Li}$ concentration (above equilibrium) has a negative effect on the reactivity. This could be compensated with a higher enrichment of the fuel. In further calculations the ${}^6\text{Li}$ concentration will be kept at equilibrium level.

2.2 Calculations of Liquid Salt Effects on Reactivity

2.2.1 k_{∞} as a function of the moderator-fuel ratio and voiding of liquid salt coolant.

The k_{∞} in a thermal nuclear reactor depends on the moderator fuel ratio (N_{mod}/N_{fuel}). When this ratio is small (left from the moderating optimum), the decrease in the moderator fuel ratio leads to a decrease in k_{∞} due to neutron resonance capture (the core is undermoderated). When N_{mod}/N_{fuel} is large (right from the moderating optimum), the increase in moderator fuel ratio leads to a decrease in k_{∞} due to parasitic absorption of neutrons by the moderator (the core is overmoderated).

In some thermal nuclear reactor types the coolant (for example water in a pressurized water reactor (PWR)) also acts as the moderator. When voiding occurs (due to temperature rise or accident) the moderator-fuel ratio will decrease. When a negative voiding factor is desired, a thermal reactor must be designed to operate in the undermoderated area.

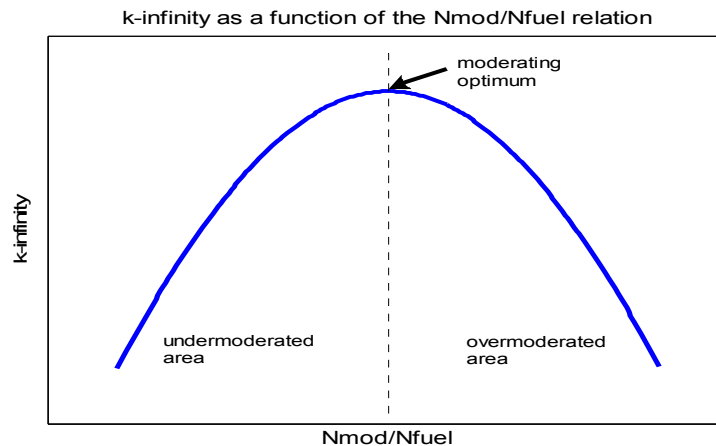


Figure 7. K_{∞} as a function of the moderator-fuel ratio. A small ratio ($N_{\text{mod}}/N_{\text{fuel}}$) will lead to a decrease in k_{∞} due to neutron resonance capture (undermoderated area), while a large ratio ($N_{\text{mod}}/N_{\text{fuel}}$) will lead to a decrease in k_{∞} due to parasitic neutron absorption by the moderator (overmoderated area).

When liquid salts are used as a coolant, the liquid salt coolant and the graphite in the reactor will both act as moderator. This introduces a difficulty in showing $N_{\text{mod}}/N_{\text{fuel}} - k_{\infty}$ relations. When voiding occurs, the composition of the moderator changes for liquid salt cooled reactors. The ratio of the coolant and carbon in the moderator will change, because the density of the coolant decreases while the carbon density remains constant. To make a clear visualization of the voiding effects, it was chosen to leave the liquid salt out of the $N_{\text{mod}}/N_{\text{fuel}}$ ratio. The $N_{\text{mod}}/N_{\text{fuel}}$ ratio in the following analyses is replaced by the $N_{\text{carbon}}/N_{\text{fuel}}$ ratio. This is proportional to the reciprocal amount of fuel per pebble (1/g fuel per pebble). Voiding of the coolant will then not change the $N_{\text{carbon}}/N_{\text{fuel}}$ ratio, but will show a different $N_{\text{carbon}}/N_{\text{fuel}} - k_{\infty}$ relation, from which the voiding coefficient can be determined.

For the selection of the preferred coolant, k_{∞} calculations were performed on a single pebble in an infinite array with the seven liquid coolant candidates and helium, as a reference. The k_{∞} calculations were performed with different fuel loadings of the pebble, in order to find the k_{∞} relations to the moderator-fuel ratio.

2.2.2 K_{∞} as a function of fuel and coolant temperature

An increase in fuel temperature will lead to Doppler broadening of resonances at an increase in resonance absorption and a decrease in reactivity. The amount of reactivity decrease due to Doppler broadening is approximately -7 pcm/K in a high temperature, gas cooled reactor (Duderstadt and Hamilton 1975).

This Doppler broadening is dependent on the neutron flux spectrum and this spectrum will be influenced by the liquid salt coolant. K_{∞} calculations were performed with different fuel temperatures (and a constant coolant density) to investigate the reactivity effect due to Doppler broadening with different salts. In reality, the density of the salt

changes with temperature with relations shown in Table 2, therefore k_{∞} calculations were also performed with changing fuel and coolant temperature.

2.2.3 K_{∞} as a function of the packing fraction

In a pebble bed HTR the porosity of the randomly closed packed bed ε is given by (Kugeler and Schulten, 1989):

$$\varepsilon = 0.375 + 0.34 \cdot \frac{d_p}{D} \quad (2.7)$$

in this relation d_p is the diameter of a single pebble and D is the diameter of the core. The packing fraction is then given by

$$packing_fraction = 1 - \varepsilon \quad (2.8)$$

In a randomly packed pebble bed the packing fraction will be around 61 %. However a different relation for the porosity of the bed can be found due to the density of the salt for two reasons:

1. For some salts the density of the salt will be higher than those of the fuel pebbles and therefore pebbles might float in these salts. This can result in a lower packing fraction (higher porosity).
2. In the liquid salt pebble bed reactor the coolant flow is planned to flow downwards through the pebble bed. This will possibly result in an increased packing fraction. A loss of forced cooling accident will then result in a lower packing fraction.

Different from a prismatic design reactor as the AHTR, which allows a great design freedom in coolant volume fractions, the packing fraction in a pebble bed reactor is fixed at around 61%-63%. An increase in the packing fraction can lower the absorbing effect of the liquid salt on the neutronics. This is interesting for salts with a positive voiding coefficient. In the current AHTR design only 6% of the core volume will be liquid salt coolant.

Possibly, the packing fraction could be increased by adding pebbles of different sizes to the pebble bed. To make an estimate of a possible increase of the packing fraction, the theoretical highest possible packing was studied. The highest packing possible with identical spheres is called cubic closed packing (ccp) or hexagonal closed packing (hcp). The packing fraction is then 74.05%. Within the interstitial sites of such a closed packed lattice smaller pebbles could be placed to achieve a higher packing fraction. Smaller pebbles could be placed in the octahedral or tetrahedral interstitial sites.

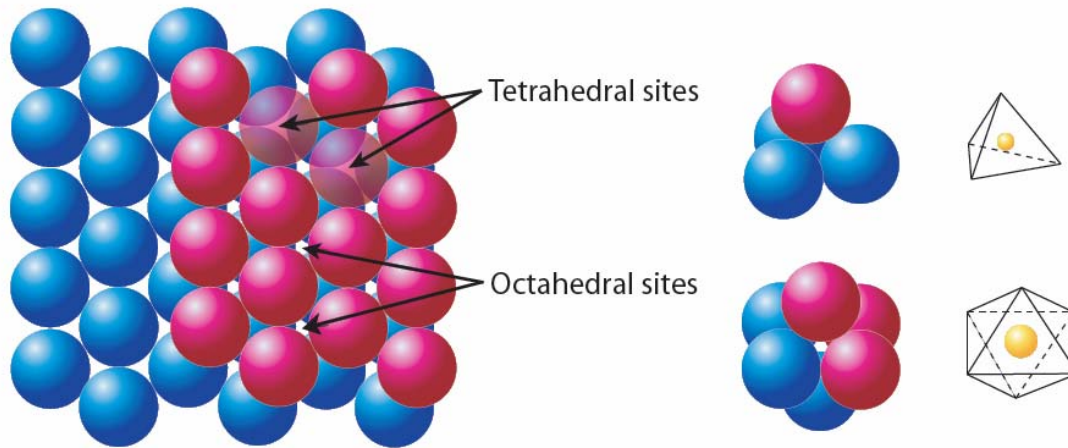


Figure 8. Examples of tetrahedral and octahedral interstitial sites; if R is the radius of the pebbles in a ccp lattice, the maximum radii of pebbles in tetrahedral and octahedral interstitial sites are $0.215 R$ and $0.414 R$ respectively.

All pebbles in a closed packing have one tetrahedral and two octahedral sites. It can be shown that if R is the radius of the pebble in the ccp lattice, the largest possible radius of the smaller pebbles in the tetrahedral and octahedral sites are $0.215R$ and $0.414R$ respectively. The increase of the packing fraction in a cubic closed packed configuration when the interstitial sites are filled is tabulated below:

Table 4 Possible increase of the packing fraction in a cubic closed packed configuration by filling interstitial sites, R_p is the pebble radius.

Sites used	Radii site spheres	Number of sites per pebble	Filled Volume per unit cell	Total Volume per unit cell	Max. Packing fraction (%)	Max. packing increase (%)
None	—	—	$16.76 R^3$	$22.63 R^3$	74.05 %	—
Tetrahedral	$0.215 R_p$	1	$16.92 R^3$	$22.63 R^3$	74.77 %	1%
Octahedral	$0.414R_p$	2	$19.13 R^3$	$22.63 R^3$	84.53 %	14%
Both	—	1 + 2	$19.30 R^3$	$22.63 R^3$	85.29 %	15%

It can be seen that adding smaller pebbles to the tetrahedral interstitial sites has a minor effect. The addition of smaller pebbles to the octahedral sites will increase the maximum packing fraction with 14 %. The addition of smaller pebbles to a randomly closed packed configuration (with a packing fraction of $\sim 61\%$), as in a pebble bed reactor, can be estimated to increase the packing fraction with 9 % (14 % of 61 %). The packing fraction can then be estimated to be around 70 %.

The increase in packing fractions calculated above is an estimate. To get an idea of the effect of the packing fraction on the k_{∞} , calculations were performed with different packing fractions.

2.2.4 Calculation scheme

From the SCALE code system (SCALE-4.4a, 2000), the BONAMI code was used for the resonance treatment in the unresolved energy region, the NITAWL-II code for the resonance treatment in the resolved energy region and the XSDRPM code for the cell weighing calculations (homogenization). The codes were run by using the CSAS driver code, which prepares the input files for the selected codes to run, and coupled by an own made PERL script.

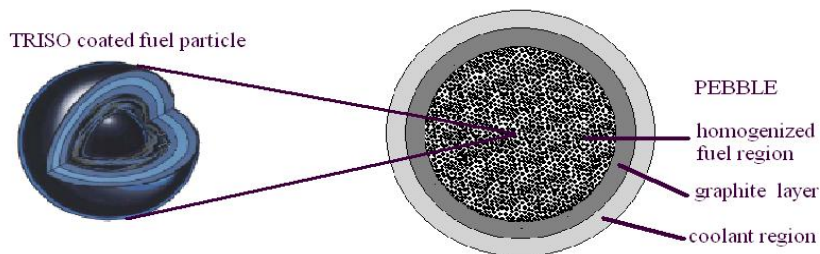


Figure 9. Build up of homogenized fuel, graphite and coolant region

In all calculations a macro cell was modeled containing a smeared fuel region, a graphite layer and a coolant region. Because the SCALE code system cannot handle explicitly the heterogeneity of the fuel, the cell-weighting procedure was split up in three parts. In the first part the TRISO coated particles were homogenized using BONAMI, NITAWL-II and XSDRNPM to generate a cross-section library of homogenized fuel zone of the pebble. The Dancoff factor used in the resonance shielding was calculated by an analytical procedure (Bende et. al. 1999) and takes into account the double heterogeneity of the fuel and the salt between the pebbles. In the second part, both the graphite fuel layer as the (liquid salt) coolant region were homogenized using BONAMI and NITAWL-II to generate two cross-section libraries of the regions. In the third part all three libraries were merged and linked to XSDRNPM to perform the cell weighing of the pebble and to calculate the k_{∞} . The parameters, used to describe the pebble and the fuel, are tabulated below.

Table 5. Parameters used to model the pebble and the fuel

Fuel enrichment (%) (UO_2)	10,15,20
Pebble packing fraction (%)	61
Triso radii(kernel, buffer, IPyC, SiC, OPyC areas) (cm)	0.025; 0.034; 0.038; 0.042; 0.045
Pebble radii (fuel zone, graphite layer) (cm)	2.5 ; 3

2.3 Results of Liquid Salt Reactivity Calculations

2.3.1 K_{∞} as a function of 1/HM per pebble

This section presents the results of the k_{∞} calculations performed. Figure 10 shows the k_{∞} as a function the inverse the fuel load (1/g heavy metal) per pebble. The (1/g heavy metal) per pebble relation is equivalent to the relation $N_{\text{mod}}/N_{\text{fuel}}$ (When the amount of fuel in a pebble is increased the value for $N_{\text{mod}}/N_{\text{fuel}}$ will become proportionally smaller). The liquid salt coolant is not accounted as a moderator because of reasons explained in §2.2.1. Three different fuel enrichments are simulated, 10,15 and 20 %. For all salts a moderating optimum can be identified. The undermoderated area is small for most salts. When looking at the 10 % enrichment results one can observe that for LiF-NaF-KF, NaF-ZrF₄-KF and NaF-NaBF₄ very high fuel loadings per pebble are necessary to be situated in the undermoderated area. The moderating optimum lays for these salts around 30-50 grams (0.02 - 0.03 g⁻¹) fuel per pebble. For NaF-BeF₂, NaF-ZrF₄ and LiF-NaF-ZrF₄ the moderating optimum lays around 11-15 grams (0.07 - 0.09 g⁻¹) fuel per pebble and for LiF-BeF₂ around 6 grams (0.17 g⁻¹).

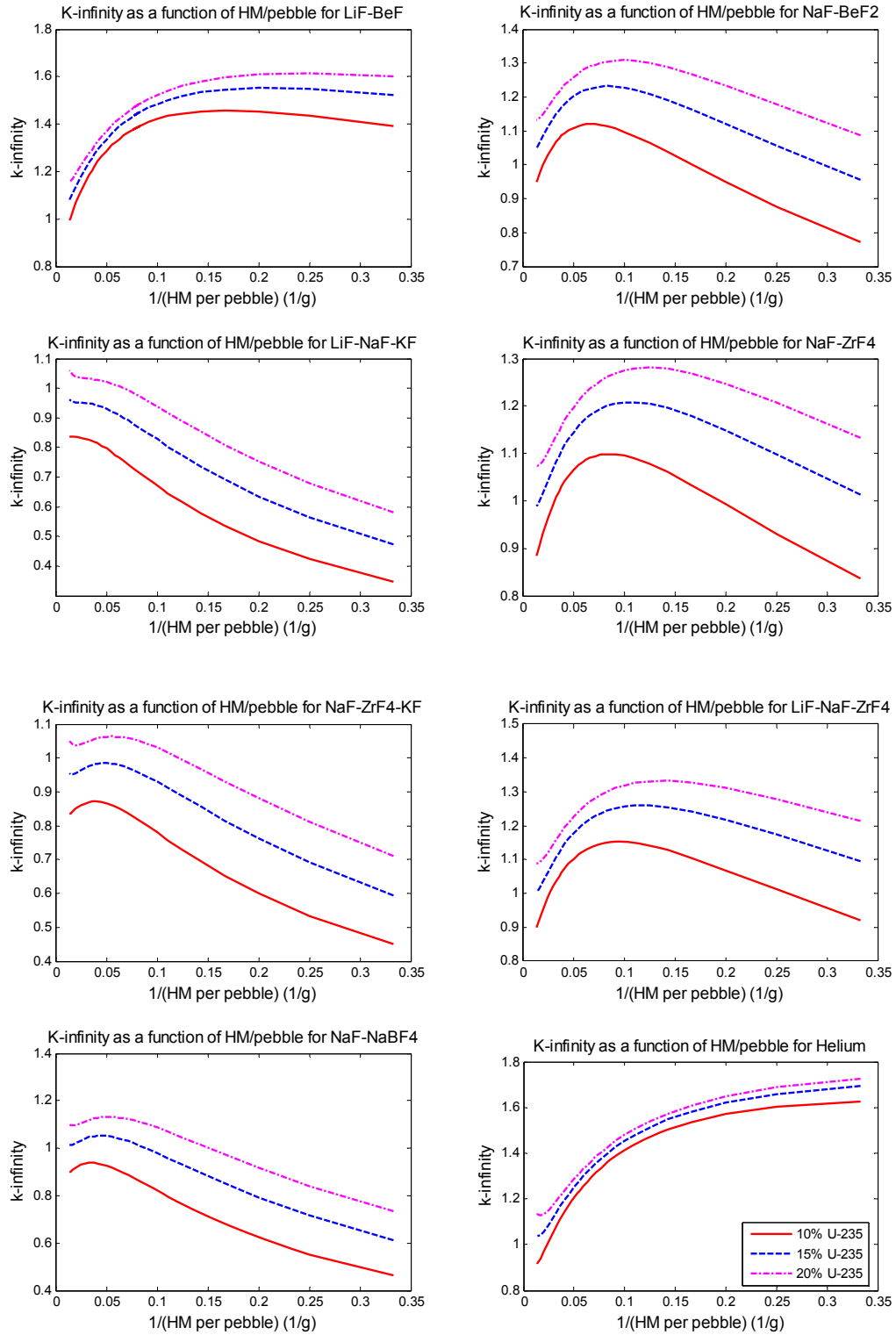


Figure 10. K-infinity as a function of 1/HM per pebble for all liquid salt candidates and Helium

2.3.2 Effect of liquid salt voiding on K_{∞}

Calculations were performed with decreasing density of the salt at fixed temperatures to examine the dependency of the k_{∞} on voiding of the different salts.

Most salts are not very good moderators. The absorbing effect of most liquid salts appears to be stronger than the moderating effect. Voiding will then lead to more thermal neutrons in the macro cell and thus a higher reactivity. Liquid salt coolant voiding can therefore lead to a positive void coefficient in the undermoderated area. This can be concluded when comparing the k_{∞} values of the different salts with the k_{∞} values calculated for the helium coolant. Helium has no effect on the neutronics because of its low atomic density and very low neutron absorption and scattering cross-sections. Except for LiF-BeF₂ all salts have lower k_{∞} values than Helium at any fuel load. Voiding of the candidate salts when situated in the undermoderated area can therefore lead to a positive reactivity coefficient.

If voiding occurs the k_{∞} will move in the direction of the helium k_{∞} -curve, as depicted in Figure 11. This can lead to a negative voiding reactivity effect (for LiF-BeF₂ with fuel loading higher than ~8-9 grams (~0.11-0.13 g⁻¹) per pebble negative voiding will occur. Figure 11- left) but in most cases voiding will lead to a positive reactivity effect, Figure 11- right).

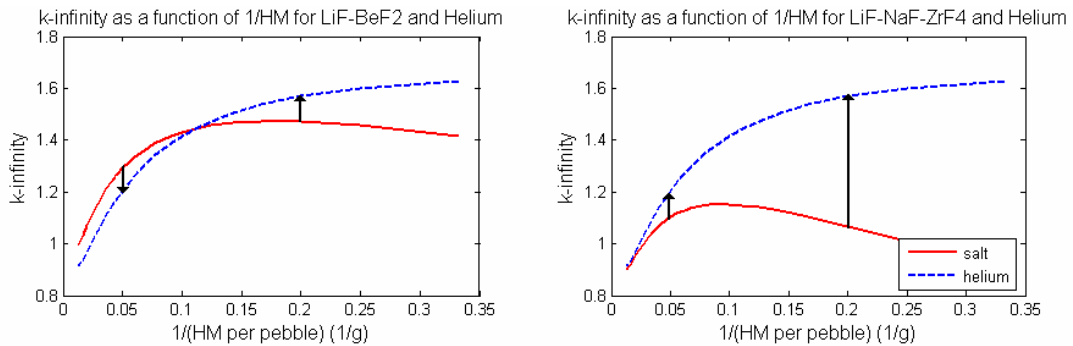


Figure 11. Voiding of liquid salt coolant: the k_{∞} -curve will move in the direction of the k_{∞} -curve of Helium. For ⁷LiF-BeF₂ a negative voiding effect will occur with fuel loadings of over 9 gram HM per pebble. For LiF-NaF-ZrF₄ voiding will always result in a positive reactivity coefficient.

When the k_{∞} results of the liquid salts are compared with the k_{∞} results of helium, the complete voiding coefficients for different fuel loadings can be found. The total voiding reactivity coefficients are depicted in Figure 12 and Figure 13 for three different fuel enrichments (10%, 15% and 20%).

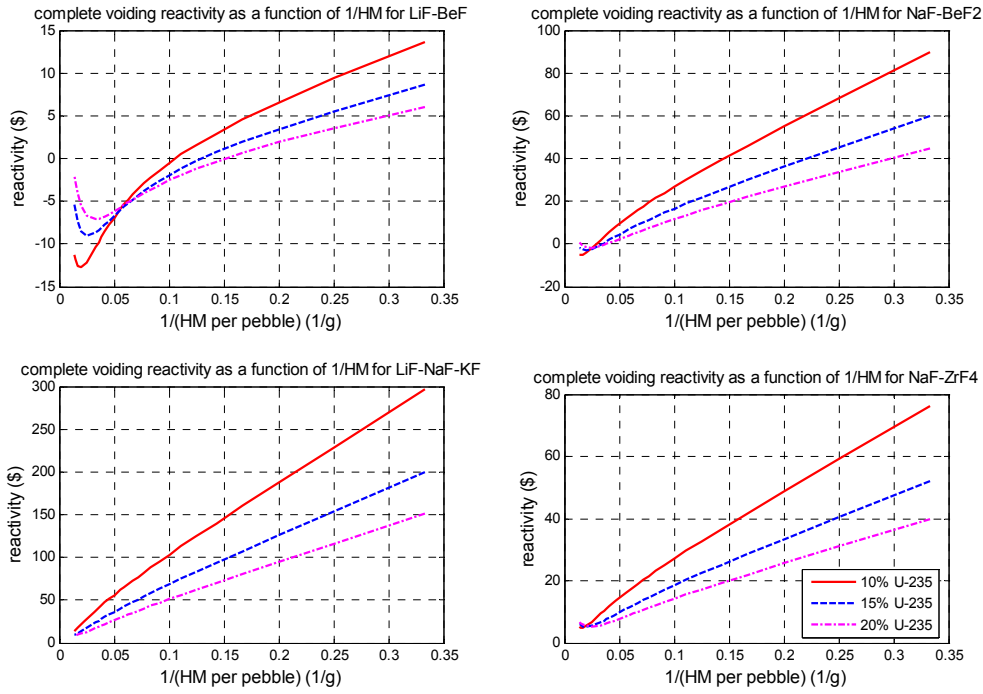


Figure 12. Complete voiding reactivity for LiF-BeF₂, NaF-BeF₂, LiF-NaF-KF and NaF-ZrF₄. Voiding will lead to a negative reactivity coefficient only with LiF-BeF₂.

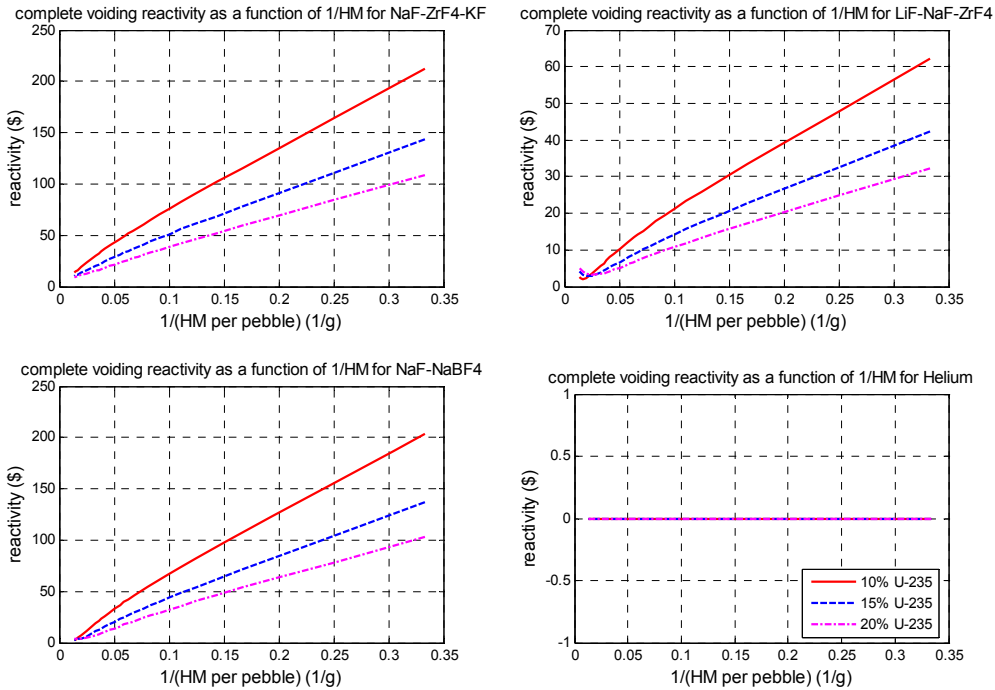


Figure 13. Complete voiding reactivity for NaF-ZrF₄-KF, LiF-NaF-ZrF₄, NaF-NaBF₄ and Helium. Voiding of Helium doesn't add or subtract reactivity due to the small density of Helium.

2.3.3 k_{∞} as a function of fuel temperature

In the previous results it was shown that complete voiding can lead to a positive reactivity coefficient. In Figure 14 the results for the dependency of the k_{∞} on fuel and coolant temperature are shown. The effect of the Doppler broadening was simulated by increasing the fuel temperature while keeping the liquid salt coolants at a constant density (density salts at 1173 K) and a fuel loading of 12 g HM per pebble.

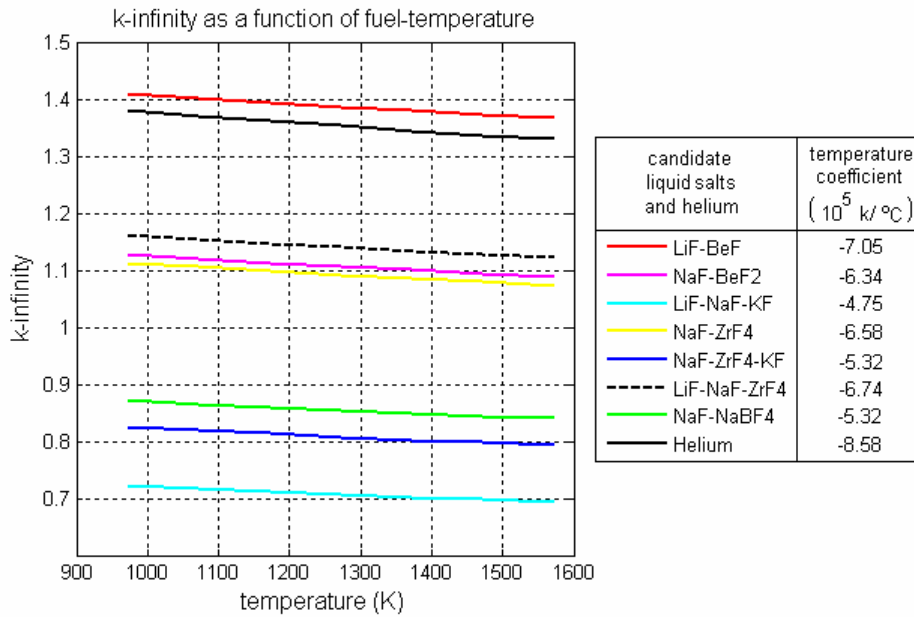


Figure 14. The k_{∞} as a function of fuel temperature, while keeping the coolant at a constant density (density at 1173 K) and a fuel loading of 12 g HM per pebble. The Table (Legend) shows the numeric values of the fuel temperature coefficient for different salts and Helium.

For all salts the fuel temperature coefficient is negative and in the order of $-6 \text{ pcm}/^{\circ}\text{C}$. The fuel temperature coefficient salts are stronger negative when the k_{∞} -values of the macro-cell are higher (compare the temperature coefficients of LiF-BeF₂, NaF-BeF₂ and LiF-NaF-KF).

2.3.4 k_{∞} as a function of fuel and coolant temperature (Doppler and voiding combined)

When complete removal of the coolant from the primary system can be prevented, complete voiding will not occur in the LSBPR. If the liquid salt coolants are kept below their boiling temperatures, the densities of the coolants will decrease (with relations shown in Table 2, on page 10) with increasing temperatures. The “real” temperature dependence of the k_{∞} with the different salts was simulated. The results for a fuel loading of 12 g HM per pebble are depicted in Figure 15.

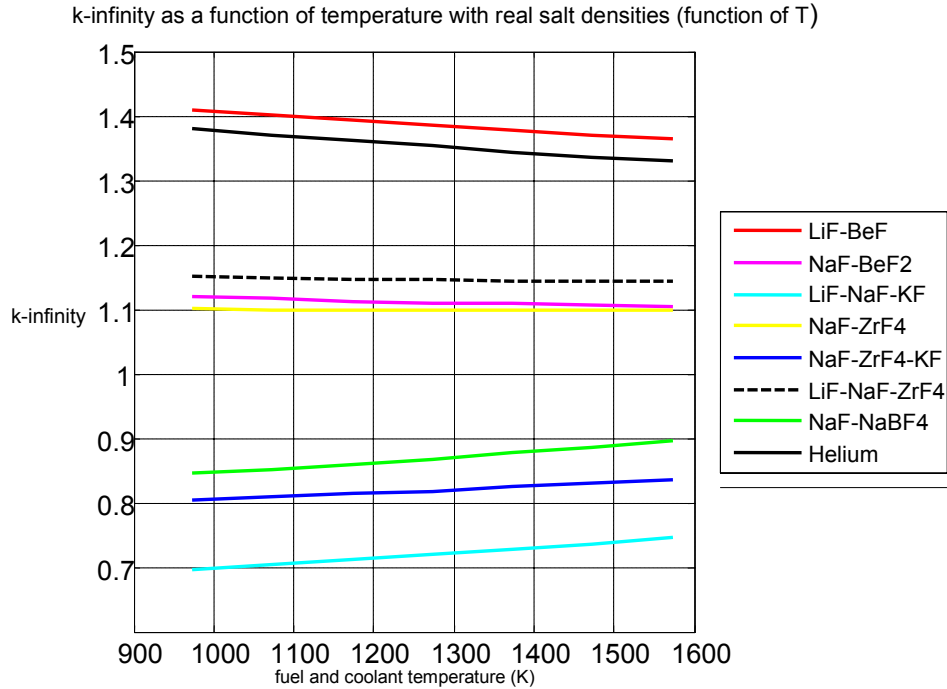


Figure 15. Temperature dependency of k_{∞} with temperature dependent liquid salt densities, with 12 g HM per pebble.

The salts with high voiding coefficients at this fuel load (NaF-NaBF₄, NaF-ZrF₄-KF and LiF-NaF-KF) show positive temperature coefficients. For the liquid salts NaF-BeF₂, NaF-ZrF₄, LiF-NaF-ZrF₄ the resulting temperature coefficient is almost zero.

The resulting temperature coefficient of LiF-BeF₂ is -7.7 pcm/°C, which is stronger negative than without voiding. So in this case (12 g HM, and 10% enrichment) the negative fuel temperature coefficient and the negative voiding effect reinforce each other.

The consequence of the combined effect of voiding and the Doppler Effect can be shown when the k_{∞} is plotted as a function of the inverse amount of fuel per pebble (1/HM per pebble [1/g]) at different temperatures with real densities of the salt, see Figure 16. In this figure it is shown that, when the temperature of the macro cell rises, the effect of voiding of LiF-BeF₂ is compensated by the strong negative Doppler effect. In the figure three separate zones can be identified: In zone I the Doppler effect and the voiding effect reinforce each other, in zone II the voiding coefficient is positive but the Doppler effect is negative and dominant and in zone III the voiding effect has become dominant. With fuel loadings lower than ~3.9 (= 0.255 1/g) g per pebble, the macro cell has a positive temperature coefficient.

In a reactor core, pebbles with fuel loadings lower than 3.9 g per pebble will not contribute much to the reactivity of the core. Compared to other pebbles they have low fuel loadings and will therefore not contribute much to the total power. A limited amount of pebbles with fuel loadings lower than 3.9 g per pebble can therefore be tolerated inside the core. This introduces more designing freedom for the LSPBR.

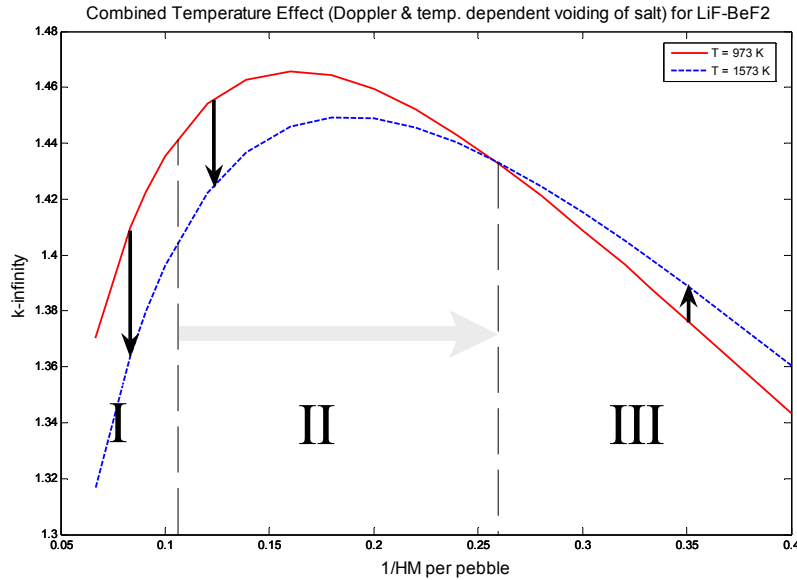


Figure 16 the combined temperature effect (Doppler and temperature dependent voiding of the salt) for LiF-BeF₂. There are three separate zones: In zone I the Doppler effect and the voiding effect reinforce each other, in zone II the voiding coefficient is positive but the Doppler effect is negative and dominant and in zone 3 the voiding effect has become dominant. With fuel loadings lower than ~3.9 g (=0.255 g⁻¹) per pebble, the macro cell has a positive temperature coefficient.

2.3.5 K_{∞} as a function of the packing fraction.

The results for the k_{∞} calculations as a function of the packing fraction are shown in Figure 17. For the 5 g HM/pebble case (Figure 17, right) the k_{∞} will increase with higher packing fractions for all liquid salts. In the 20 g HM/pebble case (Figure 17, left) the k_{∞} increases for all salts except LiF-BeF₂. This is because for 20 g HM per pebble the option with LiF-BeF₂ is in the undermoderated area. A higher packing fraction will lead to less moderation and thus to a lower k_{∞} . The turning point, where higher or lower packing fraction has no influence on the k_{∞} for the LiF-BeF₂ lies around 9 g HM per pebble. This is at the same value where the void coefficient of LiF-BeF₂ is zero (see figure 7).

If a loss of forced cooling accident would result in a lower packing fraction, this might be a problem with LiF-BeF₂. Floating of the pebbles by loss of forced cooling will then introduce a positive reactivity effect. If LiF-BeF₂ would be chosen as the coolant for the LSPBR, this effect should be compensated for.

From these results it can be seen that a higher packing fraction can introduce a higher reactivity for most salts, however the k_{∞} must become higher than the k_{∞} of helium to introduce a negative voiding effect (see Figure 11 on page 20). The estimated increase of packing fraction of 14% will therefore not be enough to introduce such a negative voiding effect. Higher packing fractions will be difficult to accomplish and it should be

investigated what the effect of such high packing fractions will be on the thermodynamics, such as the effect on pressure drop.

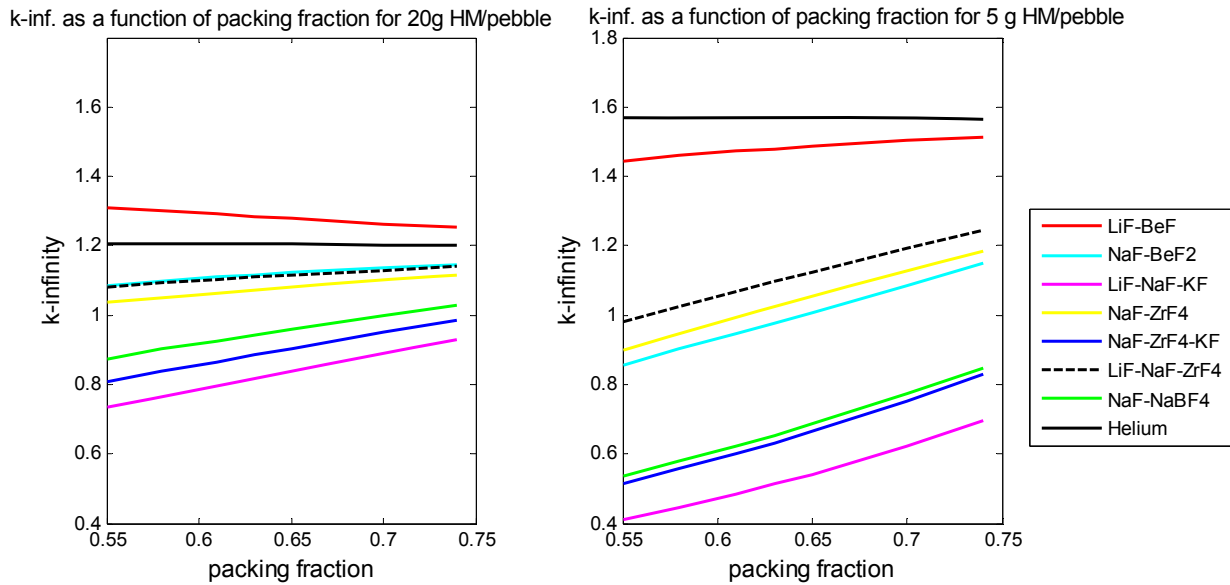


Figure 17. K_{∞} as a function of the packing fraction for two sample cases, 20 g HM/pebble (left picture) and 5 g HM/pebble (right picture), both with 10% enrichment.

2.4 Conclusions on Selection of the Liquid Salt Coolant

It can be concluded that LiF-BeF₂ has the best neutronics properties of all candidates and will therefore be selected as the leading primary coolant for the LSPBR. The choice is made in favor of LiF-BeF₂, because of the following reasons:

- LiF-BeF₂ has the highest moderation ratio (lowest absorption cross-section), and therefore the best moderating quality;
- LiF-BeF₂ has the highest k_{∞} -values for different fuel loadings of the pebble, this increases the freedom of geometry designs;
- LiF-BeF₂ is the only salt with a negative voiding reactivity constant. The voiding coefficient is negative for fuel loadings of ~ 9 g (0.11 g⁻¹) HM/pebble and higher.
- LiF-BeF₂ has the strongest negative total temperature coefficients of all liquid salt candidates. The negative voiding effect and the Doppler effect endorse each other, up to a fuel loading in the pebble of ~ 9 HM per pebble.
- If prevention of the complete removal of the coolant can be guaranteed, a fuel loading less than 9 g HM per pebble is possible with LiF-BeF₂ as the primary coolant. The benefit of this is that pebbles can be kept in the reactor longer and a

higher burnup is possible. This introduces more design freedom for the LSPBR. With lower fuel loadings the result of voiding coefficient of the coolant by temperature increase and the temperature coefficient by the Doppler effect remains negative until a fuel loading of $\sim 3.9 \text{ g}$ ($= 0.255 \text{ g}^{-1}$) HM/pebble.

Points of attention for LiF-BeF₂ coolant:

- The Lithium used for fresh LiF-BeF₂ salt will consist of 0.01 % ⁶Li. This ⁶Li concentration will decrease with operation time to an equilibrium concentration of $\sim 0.001 \text{ wt}\%$. During the period from first startup until equilibrium the ⁶Li concentration (above equilibrium) has a negative effect on the reactivity.
- The density of LiF-BeF₂ at operation temperature, 1173 K to 1273 K varies from 1.84 g/cm^3 to 1.79 g/cm^3 . This is slightly more than the density of the carbon used ($\sim 1.7 \text{ g/cm}^3$). Therefore the possibility exists that pebble will float, especially during a loss of forced cooling accident. For fuel loading of 9 g HM per pebble and more, a decrease of the packing fraction, by possible floating of the fuel, will lead to an increase of reactivity.

3 The Liquid Salt Pebble Bed Reactor (LSPBR)

With FLiBe selected as the primary liquid salt coolant, the goal is now to design a reactor, which has: a pebble bed core geometry, a large power output, low difference between maximum fuel and coolant temperatures, high coolant exit temperatures and small differences in temperature between coolant inlet and outlet. When the LSPBR dimensions were set much was learned from the AHTR design. Therefore, the dimensioning of the LSPBR will except for its fuel geometry not differ much from the AHTR. In this chapter the main design of the LSPBR will be formed.

3.1 Fuel

The fuel for the pebble bed reactor is similar to that of other (gas-cooled) high temperature pebble bed reactors. uranium dioxide (10% ^{235}U) fuel kernels with a diameter of approximately 0.5 mm are coated with multiple layers of pyrolytic carbon and silicon carbide to form a 0.9-mm-diameter microsphere (see Figure 18). These microspheres practically completely retain the fission products up to a fuel temperature of 1600 °C. In fact, fuel temperatures of 1600° C can be tolerated for limited periods of time (~100 of hours). When the fuel kernels are coated with ZrC, it may be possible to increase the fuel failure temperature to 2000 °C (Williams, 2004), it is not sure that this will be necessary for liquid salt cooled nuclear reactors, since the boiling point of most salts is also a limiting factor.

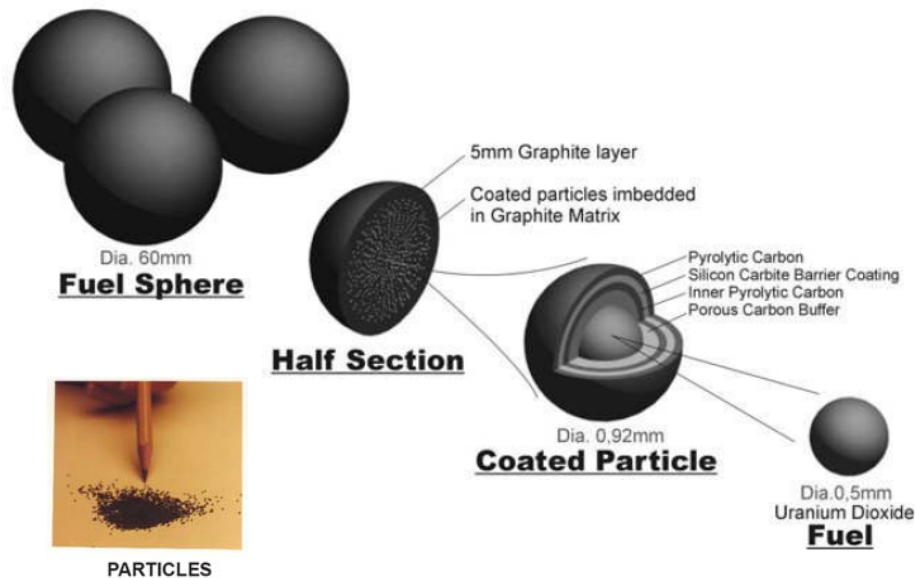


Figure 18. Diagram of the high temperature pebble fuel structure, on the left a picture is shown to indicate the size of the TRISO coated particles.

The coated particles are incorporated into a graphite pebble coated with a 5 mm graphite layer. The diameter of the fuel pebbles is 60 mm.

3.2 Dimensioning the LSPBR

The pressure drop over the reactor core is a restricting factor on the size of the LSPBR. If the work needed to overcome the pressure drop in the packed bed, is several percentages of the total power generated, the system will lose efficiency and economical benefits.

3.2.1 Pressure drop

To estimate the pumping power in the LSPBR the pressure drop over the core can be calculated. The pressure drop over a packed bed can be calculated with the Ergun-relation, which is valid over the whole Re-number range (Van den Akker and Mudde, 1996):

$$\Delta p = \frac{1-\varepsilon}{\varepsilon^3} \left(170 \frac{\mu}{\rho v_0 d_p} (1-\varepsilon) + 1.75 \right) \frac{H}{d_p} \rho v_0^2 \quad (3.1)$$

here ε is the porosity of the pebble bed (or the coolant volume fraction), μ the dynamic viscosity, ρ the density of the coolant, v_0 the coolant velocity through the core, d_p the pebble diameter and H the height of the reactor core. With

$$v_0 = \frac{\dot{m}}{\rho A} \quad (3.2)$$

(where m is the coolant mass flow and A is the axial surface of the reactor) this equation can be written as:

$$\Delta p = \frac{1-\varepsilon}{\varepsilon^3} \left(170 \frac{\mu A}{\dot{m} d_p} (1-\varepsilon) + 1.75 \right) \frac{H}{d_p} \left(\frac{\dot{m}}{A} \right)^2 \quad (3.3)$$

The mass flow of the coolant inside the reactor core can be calculated with the relation

$$\dot{m} = \frac{P}{c_p \Delta T} \quad (3.4)$$

here c_p is the heat capacity of the coolant, P the total thermal power produced in the reactor and ΔT the temperature difference of the coolant between the in- and outlet of the core. To make an estimation of the pressure drop that can be expected with different core shapes, for the liquid salt coolant FLiBe pressure drops were calculated for cylindrical core with a 300 m³ core volume. The pressure drop can also be calculated with another relation. It is used in the computer code THERMIX to calculate pressure drops and given by (Kugeler and Schulten, 1989):

$$\Delta p = \Psi \frac{1-\varepsilon}{\varepsilon^3} \frac{H}{d_p} \frac{1}{2\rho} \left(\frac{\dot{m}}{A} \right)^2 \quad (3.5)$$

with

$$\Psi = \frac{320}{\frac{\text{Re}}{1-\varepsilon}} + \frac{6}{\left(\frac{\text{Re}}{1-\varepsilon}\right)^{0.1}} \quad (3.6)$$

$$\text{Re} = \frac{\dot{m}d_p}{A\mu} \quad (3.7)$$

This relation is valid for the Reynolds numbers which satisfy the following relation:

$$1 \leq \frac{\text{Re}}{1-\varepsilon} \leq 10^5 \quad (3.8)$$

$$0.36 \leq \varepsilon \leq 0.42 \quad (3.9)$$

With the pressure drop, the pumping power can be calculated, necessary to overcome this pressure difference by (Moran and Shapiro, 1998):

$$W_{pump} = \frac{\dot{m} \Delta p}{\rho} \quad (3.10)$$

here, W_{pump} is the pumping power. In Figure 19 the pressure drop over the pebble bed is shown as a function of the core height with a volume of 300 m^3 . It can be seen that both relations give results that differ significantly. However, the pressure drop is still under 1 bar for both relations if the height of the core is below 8 m.

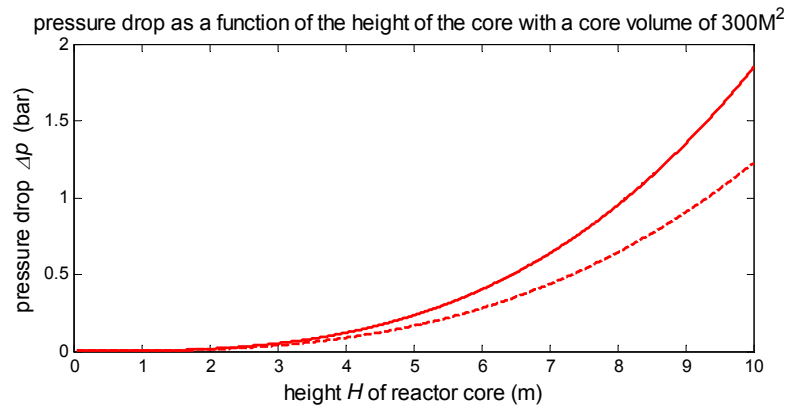


Figure 19. The pressure drop over the pebble bed reactor core as a function of the height of the pebble bed with a core volume of 300 m^3 , a total power P of 2500 MW and a temperature difference of 100°C . The liquid salt coolant is FLiBe . The solid line is the result from the Ergun relation and the dashed line is the result from the relation presented by Kugeler and Schulten.

In Table 6 the results for the pressure drop calculations are summarized. In these calculations the following factors were assumed: The pebble bed volume of 300 m^3 , the reactor core height of 7.5 m , a temperature difference between in- and outlet of 100°C , a total Power of 2500 MW(t) and an electrical power of 1300 MW(e) .

Table 6. Summary of pressure drop calculations for FLiBe and NaF-ZrF₄.

Liquid salt properties in pressure drop calculation for FLiBe	Results
density ρ at 950 °C (kg/m ³)	1815.7
dynamic viscosity at 950 °C (Ns/m ²)	2.498E-3
heat capacity c_p (J/kgK)	2386
Results with H = 7,5 m; core Volume 300 m³; $\Delta T = 100$ °C; total Power = 2500 MW	
Mass flow m (kg/s)	10478
Coolant velocity (m/s)	0.144
Reynolds number Re	6291.7
Ergun: Pressure drop (bar)	0.782
Ergun: Pumping power (kW)	451.4
Ergun: Fraction of total electrical Power of 1300MW (%)	0.032
K&S : Pressure drop (bar)	0.533
K&S : Pumping power (kW)	307.7
K&S : Fraction of total electrical Power of 1300 MW (%)	0.024

It can be concluded that there is a significant difference in results between both calculation methods. The power necessary to pump the salt through the reactor core is not a restriction for this core shape, the necessary pumping power is less than 0.1 % of the total electrical power produced. It is therefore not a restriction in the preliminary design of the LSPBR.

3.2.2 Maximum power

The maximum power that can be generated with a nuclear reactor is limited by the capacity of the system to transfer the heat away from the core while not exceeding temperatures at which fuel failure occur. This should be the case for normal operation conditions as for decay heat removal at accident situations, such as loss of forced cooling. Simulations will be performed to evaluate the capacity of the reactor system to transfer decay heat from the system.

The coated particle graphite fuel used in this design practically completely retains the fission products up to a fuel temperature of 1600 °C. The AHTR design has a large power output of 2400 MW(t). In this first study a power output of 2500 MW(t) is chosen for a pebble bed design. The ultimate power will be chosen when it is shown that the decay heat can be removed effectively from the reactor core. The average core power density is set to be 7,5-10 MW(t)/m³. To achieve such a power density, a reactor core volume of ~300 m³ is needed.

3.2.3 Core shape

There are two core shapes considered, a cylindrical shape or an annular shape can be chosen. Possible differences between the cylindrical and the annular core shape will be:

- the pressure drop
- the flow velocity of the coolant
- the neutron flux shape
- power profile
- maximum fuel temperatures
- heat transfer properties.

To investigate these differences for this preliminary design of the LSPBR, both a cylindrical and an annular core shape will be investigated. From the investigation results one preferred shape will be selected.

3.3 LSPBR preconceptual design parameters

Based on the dimensioning in the previous paragraphs and information from the AHTR project, the design parameters were set for the LSPBR. The parameters shown here will be used for the steady state calculations and production of the cross-section libraries used. In Table 7 the fuel parameters are shown. The same fuel was used for the both the annular and the cylindrical core calculations. The core will be refueled on line. For the steady state calculations a homogenous fuel loading of 8 g per pebble is assumed to simulate an equilibrium fuel loading in the core. To compensate for the overreactivity, boron is added to the moderating graphite. In reality, reactivity could also be compensated by control rods and pebble loading.

Table 7. Fuel pebble and coated particle specifications.

Fuel Pebble	
Pebble outer radius (cm)	3.0
Thickness of fuel free zone (m)	0.5
Density of graphite fuel free zone ($\text{g}\cdot\text{cm}^{-3}$)	1.7
Total heavy metal loading per fuel pebble	8 g
Enrichment for equilibrium fuel (%)	10
Impurity of natural boron in moderating graphite (ppm)	0.75
Coated particle	
Fuel kernel diameter (mm)	0.25
Particle material type	UO ₂
UO ₂ density ($\text{g}\cdot\text{cm}^{-3}$)	10.5
Coating material	C / C / SiC / C
Layer thickness: Buffer/PyC/SiC/Outer PyC (μm)	90 / 40 / 35 / 35
Buffer layer densities ($\text{g}\cdot\text{cm}^{-3}$)	1.00 / 1.85 / 3.16 / 1.85

In Table 8 the liquid salt parameters are shown. The salt will enter the core at 900°C and will be heated to 1000°C. To achieve this with a power of 2500 MW(t) a mass flow rate of 10478 kg/s will be set.

Table 8. Liquid salt coolant information

Description	Cylindrical core	Annular Core
Coolant salt	FliBe	FliBe
Coolant inlet temperature (°C)	900	900
Coolant outlet temperature (°C)	1000	1000
Coolant mass flow rate (kg/s)	10478	10478
Coolant fraction (core) (%)	40	40
Estimated velocity inside the pebble bed (m/s)	0.36	0.37

In Table 9 the dimension of both core geometries are listed. The dimensions of the core are chosen to achieve a core volume of approximately 300 m³. The annulus of the annular core is 2 m in diameter. To achieve a volume for the annular core that is close to the volume of the cylindrical core the annular core outer radius was set at 370 cm, 10 cm larger than the cylindrical core radius. In both designs the top and bottom reflector accommodate coolant channels and have a porosity of 50 %. Both designs have an additional top and bottom salt plenum of 2 m high to provide additional thermal inertia to remove decay heat.

Table 9. Dimensions of 2 different core shapes

Description	Cylindrical Core	Annular Core
Core height (m)	7.5	7.5
Core outer diameter (m)	3.60	3.70
Core annulus (m)	n. a.	1.0
Total Core Volume (m ³)	305.36	299.0
Volume fraction fuelzone (TRISO, and inner graphite)	0.35	0.35
Average estimated power density (MW/m ³)	8.19	8.36
Core axial/radial mesh size (m)	0.50/0.30	0.50/0.30
Number of axial/radial meshes	15 / 12	15 / 9
Vessel diameter (m)	9.00	9.20
Vessel height (m)	16.60	16.60
Vessel thickness (m)	0.10	0.10
Argon gap (m)	0.10	0.10
Guard Vessel thickness (m)	0.02	0.02
Outside reflector thickness (m)	0.80	0.80
Top reflector thickness (m)	2.00	2.00
Top reflector thickness (m)	1.50	1.50
Porosity top and bottom reflector (fraction of solid material)	0.50	0.50
Porosity top and bottom plenum (fraction of solid material)	0.1	0.1
Top plenum inner/outer diameter / height (m)	0.0/3.6/2.0	1.0/3.7/2.0
Bottom plenum inner/outer diameter / height (m)	0.0/3.6/2.0	0.0/3.7/2.0

4 Steady State Calculations, the LSPBR during Normal Operation

To examine the behaviour of the LSPBR during normal operation, steady state calculations were performed. To perform these calculations the neutronics code EVENT was coupled to the thermal hydraulics code THERMIX (Boer, 2005). With THERMIX, temperature profiles in the fuel and the coolant, the velocity field of the coolant and the pressure field are calculated. The pressure drop over the reactor and heat fluxes can also be calculated. The neutronics code EVENT is able to calculate the neutron flux density in the LSPBR core by solving an eigenvalue problem for the particular reactor shape. Steady state calculations were performed for both the annular and the cylindrical core shapes.

THERMIX was originally written for HTR-simulations with gas-cooling. THERMIX has been modified for the thermal hydraulic simulations of the Liquid Salt Pebble Bed Reactor (LSPBR). To implement an extra coolant option, several subroutines had to be modified. The modifications of Thermix for the use of FLiBe can be found in appendix A.3.

In this chapter, first the coupling between THERMIX and EVENT is discussed, then the THERMIX and EVENT input is presented and then the results of the steady state calculations are investigated

4.1 THERMIX EVENT coupling

When EVENT and THERMIX are coupled a detailed description can be made of the reactor core physics (Boer, 2005). In Figure 20 the calculations scheme for coupled steady state calculations is shown. In this coupling, the steady state operation is found for the LSPBR. The cross-section library is poisoned with boron to achieve $k_{\text{effective}} = 1$ at reasonable temperatures close to an operational power of 2500 MW. The coupled calculation consists of several components which are discussed below.

XS library

When a steady state calculation is performed, first a temperature dependent cross-section library is generated for the core and the reflector regions. The 2 group cross-section library of ANISN format contains homogenized cross-sections for the core and the reflectors for two different temperatures. The temperature dependent cross-sections can then be obtained by interpolation. The cross-section working library is created from the XMAS 172 energy group cross-section master library.

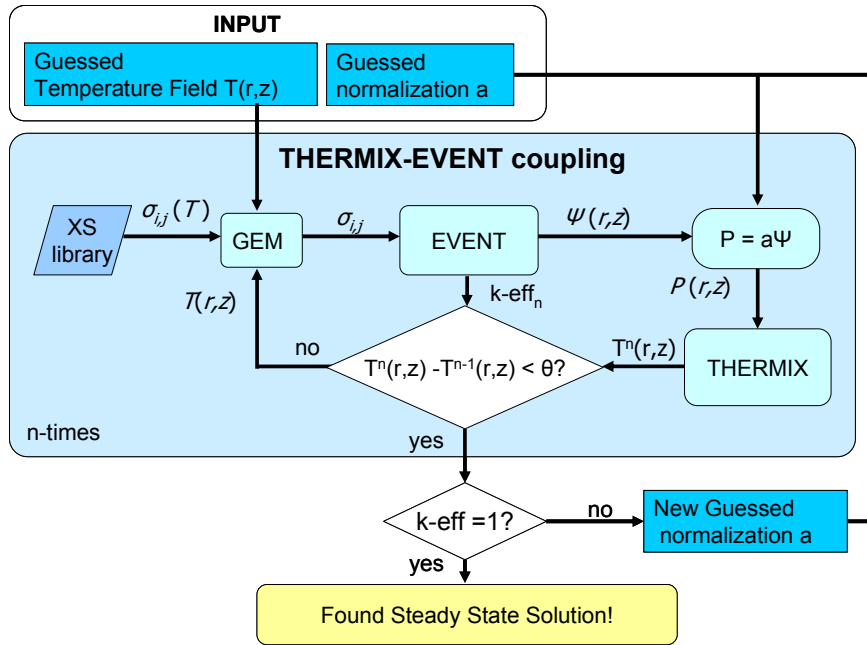


Figure 20. Scheme of coupled THERMIX and EVENT calculation to find Steady State Solution.

At two different temperatures the TRISO coated particles, the graphite layer and the coolant are homogenized using BONAMI, NITAWL-II and XSDRNPM. The Dancoff factor used in the resonance shielding was calculated by an analytical procedure (Bende et. al. 1999). The reflector zones are homogenized using BONAMI and NITAWL-II. Here, also libraries are produced at two different temperatures. The libraries produced are then collapsed to two groups and merged in to one working library by WAX. ALPO then transforms the library into the library in ANISN-format.

GEM

GEM is the input generator of EVENT. With GEM the event input, with information about the temperature dependent cross-sections, geometry and reactor dimensions, the number of energy groups etc. is transformed into input that is readable by EVENT.

EVENT

The even-parity neutronics code EVENT calculates the k-effective and the neutron flux profile inside the reactor. A power profile is then calculated by averaging the normalized (with normalization factor a) scalar flux for several regions and weighing this flux with the fission cross-sections and the energy released per fission (Boer, 2005). A detailed description of the even parity neutronics code EVENT can be found in appendix B.

THERMIX

This power profile is written in the THERMIX input. A temperature profile of the fuel (and other solid material) and coolant is calculated as well as a mass flow and a pressure

profile. The solid output temperatures are used to create new temperature dependent cross-sections for the neutronics calculation.

The program THERMIX is divided in three parts. The first part (the main program) calculates the temperatures of the solid state material in the model. The second and third parts (incorporated in the convection part of the program) calculate the fluid flow field of the coolant and the coolant temperatures. In Figure 21 a simplified flow diagram of THERMIX is shown. A detailed description of the THERMIX theory and the discretizations used is given in appendix A.

THERMIX – DIREKT flow chart

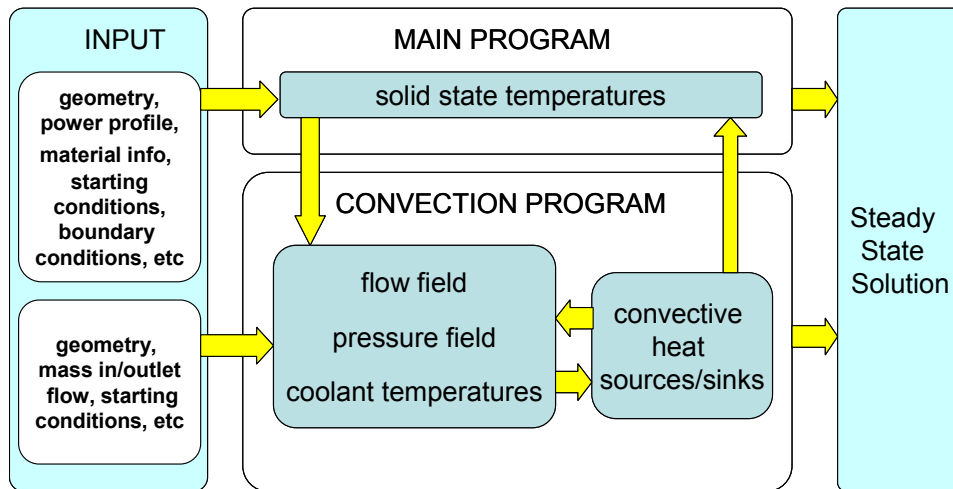


Figure 21. Simplified data flow diagram of THERMIX

The coupled calculation is performed n -times until convergence is reached. If the difference in the temperature profile of the n^{th} calculation with the $(n-1)^{\text{th}}$ calculation is less than a certain value θ , the coupling is stopped and it is verified whether an equilibrium is already reached ($k\text{-eff} = 1$?). If not, a new guess of the normalization factor of the flux (new nominal power) is made using the regula falsi method and the coupling is started again. Because the system has a negative temperature coefficient, the normalization factor of the flux is increased when $k\text{-eff} > 1$ and decreased when $k\text{-eff} < 1$. This iteration process is performed until equilibrium (steady state) is reached.

4.2 Steady state input Annular & Cylindrical Core

In this paragraph the input used for the steady state calculations is discussed. In short all input parameters have been given in paragraph 3.3. Here the specific input for THERMIX, EVENT and the cross-section library is discussed.

THERMIX & EVENT input

The input for THERMIX and EVENT is depicted in the appendix E. The materials used are:

1. The pebble bed core (pebble bed, porosity of 60 %).
2. The top and bottom reflector (graphite, porosity of 50%, described as pipes. In the annular core the coolant riser consists also of this material).
3. The top and bottom salt plenum (graphite, porosity of 99%).
4. the (inner and) outside reflector, (graphite no porosity and also graphite liner).
5. Reactor vessel (steel)
6. Argon gap, (and radiation gap with emissivity ε of 0.8).
7. Guard vessel (steel)
8. Air layer, (and radiation gap with emissivity ε of 0.4).
9. Boundary layer (fluid zone, the heat transfer coefficient is set to be 12 W/m²K).
10. Coolant inlet plenum.
11. Coolant outlet plenum.

The THERMIX input consists of two parts, a solid material part and a convection part. The solid material input consists of the materials 1 to 9. It describes the solid material from the reactor core until the boundary layer. The convection part input consists of material 1 to 3, 10 and 11. It describes the area of the core where the coolant is present. The materials 10 and 11 are the coolant inlet and the coolant outlet respectively. In the annular core the coolant will exit via coolant risers in the center inner reflector.

In both the cylindrical and the annular core the input for EVENT is given by the material inside the reactor vessel (material 1 to 4). It is expected that only this material will influence the neutronics.

Cross-section library

The cross-section library was produced using the homogenous fuel specifications listed in Table 7 (page 31) and the properties of the liquid salt coolant FliBe listed in Table 2 (page 10). The neutron energy boundaries of the fast flux and thermal flux are respectively $1.964 \cdot 10^7$ -3.3 MeV and $3.3 - 1.0 \cdot 10^{-5}$ MeV. The maximum temperature of the cross-section library is chosen around the boiling temperature of the liquid salt coolant (1430°C). It is assumed that cross-sections for higher temperatures are not physically correct. The temperature for the minimum cross-section temperature is 100°C. This can be a problem since the melting point of FliBe is 459 °C. Lower temperatures will not be physically correct. However, for the graphite reflectors, temperatures lower than 400 °C can be expected since there will be a strong temperature gradient over the reflector and the reactor vessel. The boundary of 100°C will be correct if either the effect of cross-sections made for temperatures below the melting point of FliBe can be neglected (when for example these materials are 2 meters away from the core) or when

the temperatures of salt containing regions in the reactor will not below 459 °C. For the cross-sections produced the following points must be considered:

- No fission products (as Xenon-poison) are taken into account in this steady state calculation.
- No burnup is taken into account, thus no different burnup regions through the reactor are simulated.
- No geometrical dependency of the cross-sections is taken into account.
- In the calculation of the temperature dependent cross-sections, the fuel temperature is assumed equal to the coolant temperature. The temperature used to calculate the cross-sections is the surface temperatures of the fuel (calculated by THERMIX). This means that the fuel temperature is underestimated and that the coolant temperature is overestimated.
- To compensate over reactivity (when k-eff would be larger than 1 at 2500 MW) the core was poisoned with additional Boron-10.

4.3 Steady State Results for the cylindrical core shape

In this paragraph the results of the steady state calculations for the Liquid Salt Pebble Bed Reactor are given. Two designs were investigated, the LSPBR with a cylindrical core and the LSPBR with an annular core. For both designs, steady state calculations were performed with the XS-library minimum temperature 100°C (and T_{bc} at 100°C).

The power level inside the reactor core was iterated to reach ~2500 MW. This has resulted in average power levels of ~8.2 MW/m³ in the cylindrical core and 8.4 MW/m³ in the annular core (the annular core volume is 6.36 m³ smaller than the cylindrical core). The maximum power level however is largest in the cylindrical core.

The coolant inlet temperatures were set at 900°C. The outlet temperatures are as expected around 1000 °C. The small differences in outlet temperatures are caused by the small differences in total power and the heat flux to the boundary cells. The maximum coolant and fuel temperatures are higher for the cylindrical core, which is related to the higher power density that is achieved in this core shape. The average coolant and fuel temperatures are approximately the same for both core shapes.

The pressure drops in the core are ~0.94 bar and ~1.1 bar for the cylindrical and the annular core respectively. This difference can be explained by realizing that the flow channel of the annular core is longer. The pressure drop over the pebble bed is approximately the same for both core shapes.

Table 10. Results of steady state calculation for the annular and cylindrical core with different boundary conditions and XS-lib minimum temperatures

Description	Annular core	Cylindrical core
Boundary temperature (°C)	100.0	100.0
XS-library minimum temperature (°C)	100.0	100.0
Additional B-10 in moderating graphite (ppm)	17.300	17.599
Power level (MW(t))	2500.3	2500.2
Average power density \bar{P} (MW(t)/m ³)	8.36	8.19
Maximum power density P_{max} (MW(t)/m ³)	14.67	16.82
Peak factor (P_{max}/\bar{P})	1.75	2.05
Total heat flux to boundary cells (MW(t))	3.86	3.72
Average velocity of salt in the pebble bed (m/s)	0.372	0.364
Coolant inlet temperature (°C)	900.0	900
Coolant outlet temperature (°C)	999.8	999.9
Maximum coolant temperature(°C)	1027.78	1051.46
Maximum fuel (surface) temperature (°C)	1034.73	1059.54
Maximum fuel (pebble centre) temperature (°C)	1151.9	1190.0
Average fuel (surface) temperature (°C)	970.25	970.67
Maximum reflector temperature (°C)	1026.97	1051.47
Maximum vessel temperature (°C)	617.15	614.4
Average vessel temperature (°C)	370.74	365.26
Pressure drop between inlet/outlet (bar)	1.028	0.921
Pressure drop over the pebble bed(bar)	0.6	0.6

4.3.1 Flux profiles

The calculations were performed with a two group neutron library. Therefore a fast neutron flux ($1.96 \cdot 10^7$ MeV-3.3 MeV) and a thermal neutron flux (3.3 MeV- $1.0 \cdot 10^{-5}$ MeV) is obtained. The radial projections of the thermal flux profiles are depicted in Figure 22. The cylindrical core flux is shown on the left and from the picture it can be seen that the thermal neutron flux is largest in the center of the core. In (and close to) the side reflector an increase in the flux is observed. This increase is caused by moderating of fast neutrons in the reflector zone. The radial projection of the annular thermal flux is shown on the right. The inner reflector can be identified by the large peak in the thermal neutron flux close to the inner reflector boundary at $r = 100$ cm. In the outer reflector also an increase in thermal flux can be seen.

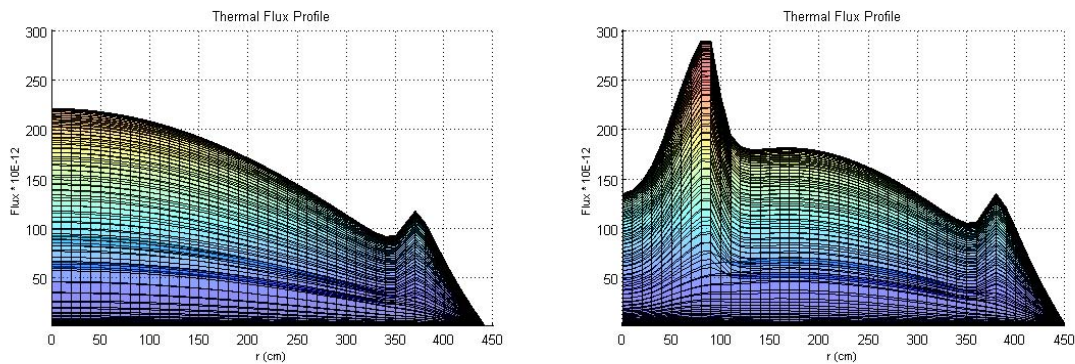


Figure 22. Radial projections of the thermal flux profiles in the cylindrical (left) and annular (right) reactor core shape. The view direction is from top to bottom.

When the cylindrical and the annular core thermal fluxes are compared it can be seen that,

- the difference between maximum and minimum flux inside the pebble bed (not reflectors) is largest in the cylindrical core;
- the flux in the annular core is more flat, from $r = 125$ cm to $r = 200$ cm the flux is almost constant, while in the same range in the cylindrical core the flux has decreased with $1/5$;
- the flux at the outer reflector boundary ($r = 360$ cm in the cylindrical core, and $r = 370$ cm in the annular core) is larger for the annular core;
- the dip in the inner reflector in the annular core is caused by absorption of neutrons by the inner reflector graphite, the diffusion length of neutrons in graphite is 59 cm.

These observations indicate that there is a more flat radial power profile in the annular core compared to the power profile in the cylindrical core. This is confirmed by the maximum power density shown in Table 10. The axial projections of the thermal fluxes are shown in Figure 23.

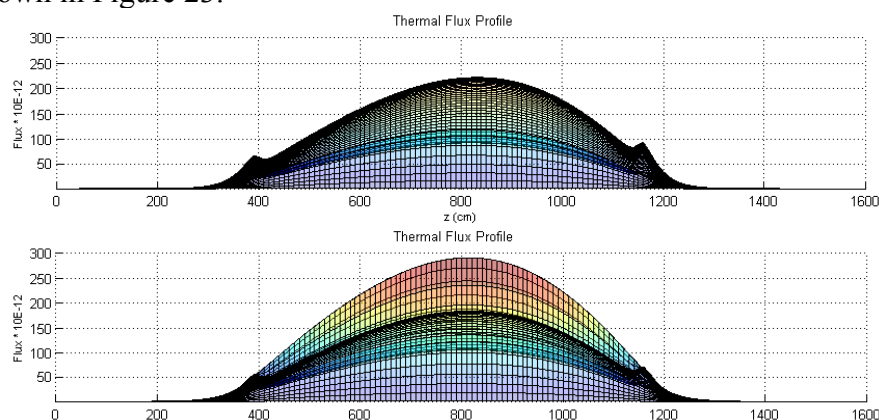


Figure 23. Axial projections of the thermal flux profiles in the cylindrical (above) and the annular (below) core shapes. In the annular axial projection, the maximum in the inner reflector somewhat disguises the maximum in the core (see also Figure 22).

The core is situated from $z = 400$ cm (bottom) to $x = 1150$ cm (top). The axial projection of the thermal neutron flux is similar for both designs (apart from the inner reflector maximum in the annular core). Local thermal flux maxima can be seen at the top and bottom reflectors. For the cylindrical core this is very clear, for the annular core the small maxima in the reflectors is somewhat disguised by the inner reflector flux maximum.

The maximum flux is not situated in the center of the core height (which is at $z = 775$ cm), but slightly more to the cooler part of the reactor. This is the effect of the negative temperature reactivity coefficient. This effect is also visible in the reflector maxima of the fluxes. The reflector maximum is significantly larger at the top reflector than at the bottom reflector. The reflector maxima are lower for the annular core shape. This can be related to a lower maximum power density or amplitude in the axial flux profile.

The fast neutron fluxes of both reactor core shapes are shown in Figure 24. The fast flux quickly disappears in the reflector zones due to moderation.

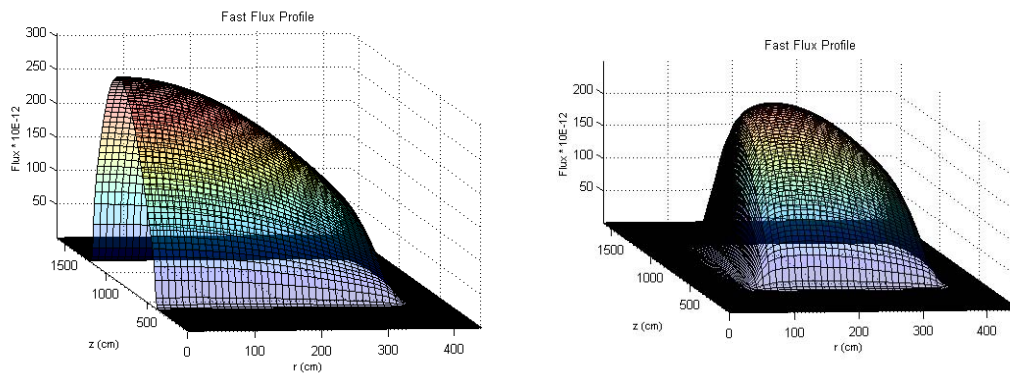


Figure 24. The fast neutron fluxes of the cylindrical core shape (left) and the annular core shape (right)

4.3.2 Power density profiles

The power density profiles of both reactor core shapes are shown in Figure 25. As expected when analyzing the thermal fluxes, the power profile of the annular core is much more flat. When analyzing the figures, it seems that the cylindrical core produces more energy because the maximum power density is much higher and because its volume seems larger. This is not the case since the power density in each ring must be multiplied with its volume to achieve the total volume per ring. From approximately $r = 1.75$ m to the side reflector the power density is larger in the annular core. Since the volume of the disks in the r - z geometry is much larger at the outside the total power will be approximately the same.

The shape of the axial profile is approximately the same for both the cylinder and the annular core. The amplitude is different. The cylindrical core has a larger maximum power density and therefore larger power densities at the top and bottom reflector. The

power density at the side reflector however is larger, because of the flatter radial flux profile.

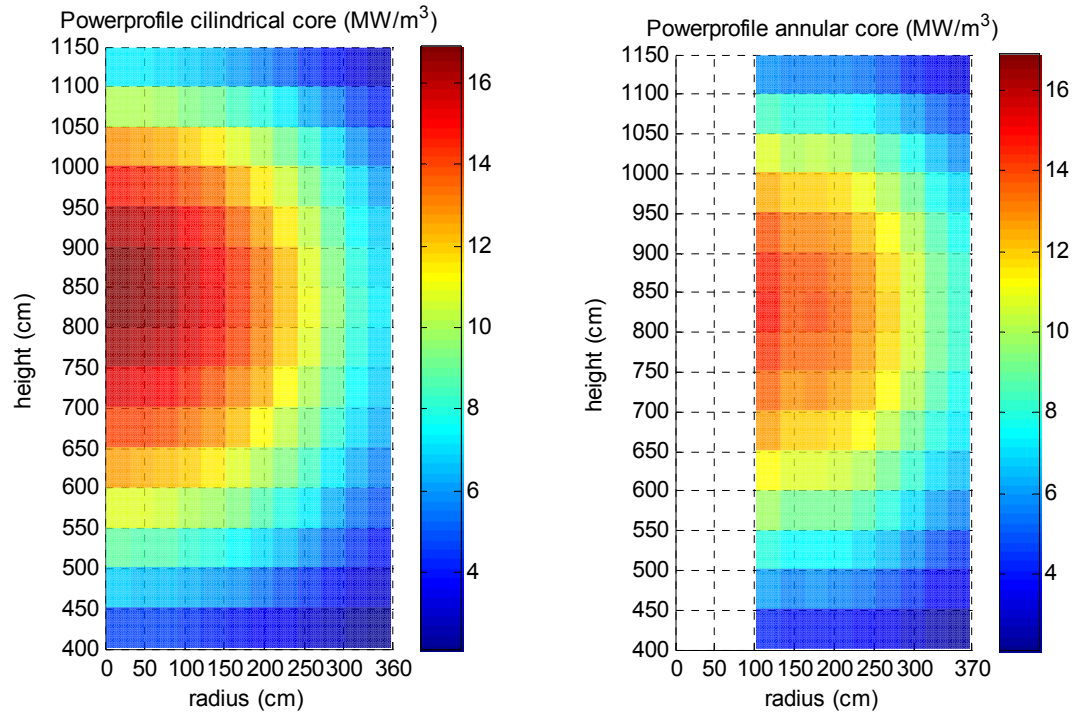


Figure 25. Power density profiles of the cylindrical core (left) and the annular core (right).

4.3.3 Temperature profiles

Temperature profiles of the solids and the salt of both reactor core shapes are shown in Figure 26. Here the top of the reactor is at $z = 0$ (THERMIX z -definition). The liquid salt is clearly visible in the solid temperature graphs and is situated between z -coordinates 330 cm and 1830 cm. It can be seen that the center of the cylindrical core reaches higher temperatures.

Due to the presence of convection heat sources (in the convection part of THERMIX) in the areas where the liquid salt is present there is a strong connection between the solid material and the liquid salt temperatures in these regions. The solid temperatures outside the core have values close to the salt temperatures where the salt is present, but decrease very fast outside the coolant filled regions. Large temperature differences can exist if the conduction in the solid material is very low. In the pebble bed, the conduction is calculated with the Zehner Schlunder method (see equation (A.14)) where the conduction of a coolant in rest is also taken into account. In the other solid region where flow occurs, the conductivity is just the conductivity of the solid material present multiplied by its volume fraction, these volume fractions are 0.5 and 0.1 for the top/bottom reflector and the salt plenums respectively (see Table 9). No convective heat transfer is modeled between the coolant and the outside reflector, in chapter 5 this will be investigated. Therefore, large differences can be seen in the temperatures of the side reflector that connect to different core parts. The approximate maximum temperature differences are

200°C for the side reflector next to the core, 600 °C next to the top/bottom reflector and 750 °C next to the liquid salt top and bottom plenum.

The liquid salt temperature increases through the core from 900 °C to 1000°C. In the lower part of the core the temperatures of the salt in the center (small in volume) are much higher than the temperatures at the outside of the core (large in volume). In the bottom salt plenum, the salt is mixed and the outlet temperature is the result of the volume weighed average.

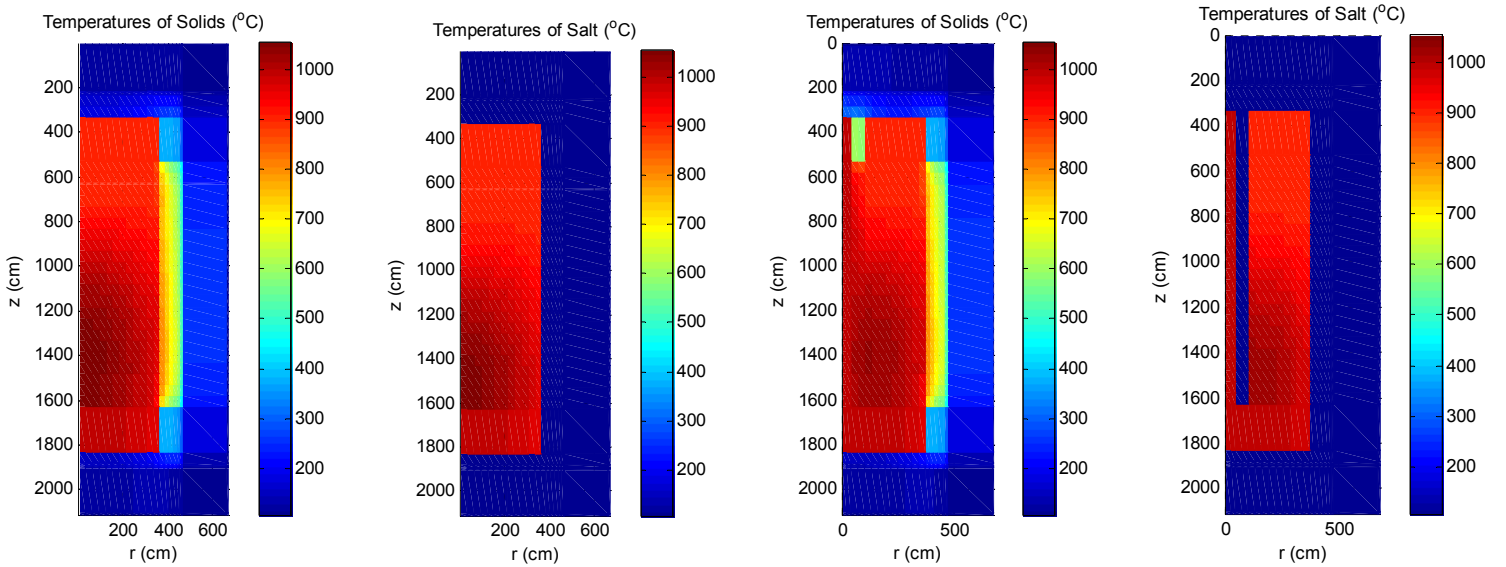


Figure 26. Temperature profiles of (from left to right): the solid material in the cylindrical core; the liquid salt in the cylindrical core; the solid material in the annular core; the liquid salt in the annular core

4.3.4 Comparison of steady state results with the AHTR

To get an idea of the performance of the LSPBR designs, they are compared with the AHTR. The fuel centerline temperature and the coolant temperature of the hot channel (coolant channel with the hot spot) in the prismatic AHTR design (Forsberg et. al. 2004) is compared with the maximum fuel temperature (at center of the pebbles) and the maximum coolant temperature in the LSPBR. The maximum fuel temperature (in the centre of the pebble) was calculated from the pebble surface temperatures (THERMIX output) by (Boer, 2004):

$$T_{F,\max} = \frac{\dot{q}_{fis} R_F}{6\lambda_F} + \frac{\dot{q}_{fis} R_F^2}{3\lambda_G} \left(1 - \frac{R_F}{R_G}\right) + T_S \quad (4.1)$$

Here q_{fis} is the average power density in the fuel region of the pebble (this is the power density of the region divided by the volume fraction of the fuel zone, see Table 9), R_F is

the radius of the fuel region of the pebble, λ_F is the conductivity in the fuel region, R_G is the radius of the outer graphite region of the pebble, λ_G is the conductivity in the outer graphite region and T_s is the surface temperature of the pebble.

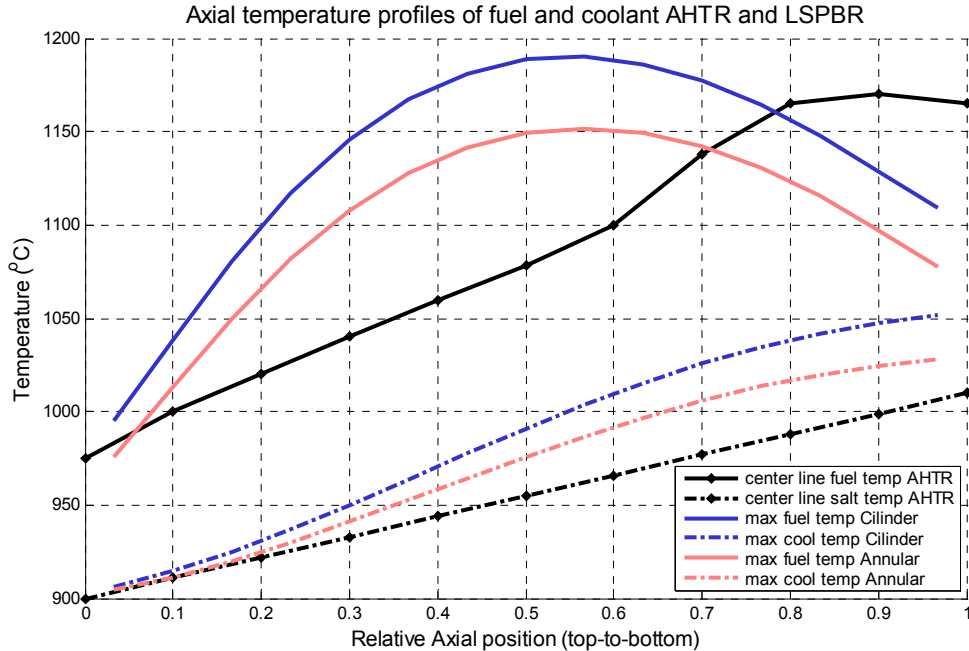


Figure 27. A comparison between the axial profiles of the maximum fuel temperatures and the average coolant temperature of the LSPBR and the LSPBR (annular & cylindrical).

The maximum coolant temperatures of the LSPBR are 25 to 50 °C hotter than the coolant temperature inside the AHTR, but increase similar through the reactor core. The fuel temperatures are different. The maximum fuel temperatures inside the LSPBR are reached at approximately 65 % of the core's height. In the AHTR the maximum temperature line increases more gradually. The difference in maximum temperatures can be explained by a different axial power profile. It appears that the AHTR has a flatter axial flux profile.

The maximum fuel temperature in the AHTR is ~1180 °C, the maximum temperature in the cylindrical LSPBR will be ~ 1190°C and the maximum temperature in the annular LSPBR will be ~1151°C. From these results it can be concluded that the annular core has the best max fuel - coolant outlet temperature ratio.

The steady state calculations on the LSPBR were performed with a homogenous core with additional poison to acquire a k-effective of 1 at 2500 MW. In reality the k-effective will be controlled using control rods or pebble flow. This can lead locally to higher power densities and a larger maximum fuel temperature. On the other hand a homogenous core will at most occur one time, at first startup. During operation the core will constantly be refueled. Fresh fuel is added at the top of the reactor core while fuel with reasonable burn up is taken out from below. This will move the power profile maximum closer to the top

(the cooler region of the core) and therefore also the maximum temperature difference between the coolant and the maximum fuel temperature.

There are several options to modify power profiles, for example, during startup dummy pebbles (graphite only) can be used to flatten the power profile

4.4 Conclusions on the steady state calculations

The following can be concluded from the steady state calculations:

- The use of the cross-section library boundary of 100°C is justified, because the salt containing regions in the reactor are not below 459 °C. Therefore no physically incorrect cross-sections were used.
- The flux profiles have their maximum in the center of the core (especially in the cylindrical core), which means that the power density is largest in the center. However, the volume of salt heated is smallest in the center, thus the high power density does not contribute much to the total heat production. A movement of the flux maximum towards the outside of the core would be desirable;
- The annular core has a more flat radial flux profile than the cylindrical core, which leads to a more flat power profile inside the core. The axial flux profiles have the same shape for both the cylindrical and the annular core;
- Because of the more flat power profile the annular core has lower maximum fuel temperatures than the cylindrical core shape;
- Vessel maximum temperatures are high, close to 620 °C. A more flat power profile will lead to an increase of the vessel temperature of a few degrees (see Table 10);
- Considering the conclusions above, the annular core is the preferred core shape for the Liquid Salt Pebble Bed Reactor.

Considering the following:

- The cross-section library was produced by interpolating the solid state temperatures (in the pebble bed, the pebble surface temperatures). This means that inside the core:
 - the liquid salt temperatures are overestimated (negative effect on k-eff);
 - the fuel temperatures are underestimated (positive effect on k-eff),and that outside the core inside the top and bottom reflector:
 - the liquid salt temperatures are under estimated (positive effect on reflector capabilities).

- The fuel used for the steady state calculations is homogenous fuel with poison to adjust the over reactivity in the core at 2500 MW(t) core power. In reality this over reactivity will be adjusted by control rods. This will influence the flux profile which can lead to higher local maximum fuel temperatures. Also, fresh fuel will be added from the top of the reactor, which will move the flux profile maximum to the top. The consequences should be investigated.
- The vessel maximum and average temperatures could possibly be lowered by additional cooling systems inside the side reflector
- The boundary temperature is not known. It is not sure if 100°C is a right temperature, therefore vessel and reflector temperatures which depend on this boundary temperature can be different from reality
- It is not sure whether the materials used in these calculations (graphite, steel) can resist the temperatures found in the calculations. The capabilities of these materials should be studied
- The input model is highly simplified, a more detailed description would render more accurate results

5 Decay Heat Removal

During operation of a nuclear power plant fission products are produced and will accumulate inside the reactor core. Some of these fission products are radioactive. Decay of these fission products, actinides and activation products contributes to the thermal energy produced in the reactor. When reactor operation is stopped no fissions will take place anymore. However, the radioactive fission products, actinides and the activation products will continue to decay and they will produce a reasonable amount of decay heat. Directly after shut down the decay heat will be around 7 % of the nominal power (~175 MW with a nominal power of 2500 MW). The decay heat decreases quickly and after a few hours it will be around 1.5 %. This decay heat must be removed out of the reactor core to prevent fuel failure or a core meltdown.

In a Loss of Forced Cooling (LOFC) accident with scram, the decay heat cannot be removed from the core by the coolant and the secondary cooling system. The decay heat must then be removed from the reactor by natural convection of the coolant inside the reactor, convective heat transfer to the reflector, conduction and thermal radiation. The maximum power that can be produced in the LSPBR is limited by the temperatures that are reached during a LOFC accident. Limits for the temperature during such a temperature transient are the boiling point of FLiBe (1430 °C) and the fuel failure temperature (1600°C). In this chapter decay heat removal simulations are described and results are discussed.

5.1 Decay Heat Calculation Methods

While radioactive fission products, actinides and the activation products will all contribute to the total decay heat, the fission products' contribution dominates the decay heat source while that of the actinides usually does not exceed 25 %. The activation products become important only for long cooling times (Kloosterman, 2000). The half lives of fission products range from a small fraction of a second to millions of years. Calculations of decay heat can be done by means of summation calculations, which take into account the build up and decay of as many nuclides as possible. However, for a limited range of the cooling time, some fission products dominate the decay heat produced, which means that simpler formulae can be used to describe the decay heat. A well known method to calculate the decay heat is the Way -Wigner decay heat calculation method. This method is used in THERMIX to calculate the decay heat. In appendix A.4 this calculation method is described.

5.1.1 Calculation of decay heat with decay heat groups (used in HEAT)

Another method to describe the decay heat is to divide the contribution of the decay heat to the total power in different decay heat groups, each with a decay constant λ_n (Agung, 2005):

$$\frac{dP_{d,n}(t)}{dt} = \frac{\gamma_n}{Q_f} P_p - \lambda_n P_{d,n} \quad (5.1)$$

Here $P_{d,n}$ is the decay heat power of group n , Q_{fis} is the prompt energy per fission and γ is the decay heat yield. When operated for a long time at a constant power, the decay power will have reached a steady state and the decay power from each group can be expressed as a fraction of the prompt power:

$$P_{d,n} = \frac{\gamma_n}{Q_f \lambda_n} P_p \quad (5.2)$$

The total power in the core can be described as the sum of the prompt power and the decay power from each group:

$$P_{tot} = P_p + \sum_{n=1}^{N_d} P_{d,n} \quad (5.3)$$

When the reactor is shutdown, the prompt fission power will be zero. The total decay power can then be found by solving equation (5.1) for each group with $P_p = 0$ and with the boundary condition given in equation (5.2) which will result in:

$$P_{d,n} = \sum_{n=1}^{N_d} \frac{\gamma_n P_p}{Q_f \lambda_n} e^{-\lambda_n t} \quad (5.4)$$

The total decay power can also be expressed in terms of the total power P_{tot} . Then equation (5.3) must be inserted in equation (5.4) to find

$$P_{d,n} = \frac{P_{tot}}{Q_f + \sum_{n=1}^{N_d} \frac{\gamma_n}{\lambda_n}} \sum_{n=1}^{N_d} \frac{\gamma_n}{\lambda_n} e^{-\lambda_n t} \quad (5.5)$$

This relation is used in the code HEAT to calculate the decay power. HEAT uses the original decay heat data of $N_d = 23$ groups from DIN (1990).

5.1.2 Analytical calculation of power profile in HEAT

The power profile from the steady state calculations is not used in the code HEAT. While the total decay power (or average power density inside the core) is calculated with the method explained above, the power *profile* was calculated analytically using the analytical equation for the flux $\phi(r,z)$ (Duderstadt and Hamilton, 1976):

$$\phi(r, z) = AJ_0\left(\frac{v_0 r}{R}\right) \sin\left(\frac{\pi z}{H}\right) \quad , \text{with} \quad \begin{array}{l} 0 \leq r \leq R \\ 0 \leq z \leq H \end{array} \quad (5.6)$$

The flux in the r-direction is a zeroth order Bessel function and in the z-direction it is a sine function. In this equation, A is a normalization factor, v_0 is the first zero of J_0 , R is the radius of the core (it is in fact the extrapolated radius, but that was not taken into account in this calculation) and H is the height of the reactor core. The normalization factor A in terms of the total core power level P can be calculated when the integral is taken over the core:

$$P = \int_V d^3r w_f \Sigma_f \phi(\mathbf{r}) = \frac{w_f \Sigma_f A 4\pi R^2 H J_1(v_0)}{\pi v_0} \quad (5.7)$$

The normalization factor is found to be

$$A = \frac{3.63P}{w_f \Sigma_f \pi R^2 H} \quad (5.8)$$

The power profile can then be described as

$$P(r, z) = w_f \Sigma_f (r, z) = w_f \Sigma_f \frac{3.63P}{w_f \Sigma_f \pi R^2 H} J_0\left(\frac{v_0 r}{R}\right) \sin\left(\frac{\pi z}{H}\right) \quad (5.9)$$

or simplified

$$P(r, z) = 3.63 \bar{P} J_0\left(\frac{v_0 r}{R}\right) \sin\left(\frac{\pi z}{H}\right)$$

here \bar{P} is the average power density in the core.

5.2 Thermal hydraulics code HEAT

It was planned to use the thermal hydraulic code THERMIX for the decay heat removal calculations. However, THERMIX was originally written to calculate the thermal hydraulics in gas-cooled reactors. Although changes were made to implement the liquid salt cooling it is not sure that the use of THERMIX is justified for decay heat calculations with a liquid coolant. Since the LSPBR is a new concept, there is no possibility to benchmark the results obtained with THERMIX. It was chosen to perform additional decay heat removal calculations with the thermal hydraulics code HEAT. Especially one simplification made in THERMIX is expected to be incorrect for liquid coolants. It will be discussed in the next paragraph.

The code HEAT was originally written for fluidized beds in chemical applications (Lathouwers and Bellan, 2001). Later, it has been used for several applications as thermodynamic calculations for passive decay heat removal in the Fluidized Bed Nuclear

Reactor (FLUBER). In this research, HEAT was used to perform decay heat removal calculations in the Liquid Salt Pebble Bed Reactor. In a 2D r-z geometry, an axisymmetric cylindrical reactor core is modeled (no annular core has been modeled, until now). Around the reactor core, graphite reflectors are modeled. A set of balance equations for momentum and energy is discretized and solved using the finite volume method with a staggered grid. Scalar variables are defined at the center of the grid cells. Time discretization is based on backward Euler scheme in combination with a pressure correction technique. The theory used in HEAT (momentum equation, energy equations and boundary conditions) is described in appendix C.

5.2.1 (Lack of) heat transport between coolant and reflector in THERMIX

The temperature profile of the solid material is calculated in the main program of THERMIX by solving the energy (conduction) equation (A.1). The solid material temperature profile is then used in the convection program of THERMIX to calculate the temperature profile of the coolant with equation (A.32). Based on the temperature difference, the contact surface within the mesh and the flow velocity, heat transfer coefficients are calculated. From these heat transfer coefficients, convective heat sources (when the coolant is hotter than the solid) or heat sinks (when the coolant is colder than the solid material) are calculated. These convective heat sources/sinks are then communicated back to the main program for a new calculation of the solid material. The convective heat sources/sinks are inserted in the heat conduction equation as a convective heat source. In the pebble bed, the heat sources are added to the nuclear heat produced (see equation (A.2)). Thus, the coolant can transport heat into/out of the system in the coolant in/outlet and the coolant can transport heat inside the convection grid (the area of the solid state grid, in which flow occurs) by virtual heat sources or sinks.

The coolant is not able to transport heat to solid material that connects to the convection grid by convective heat transfer. This is where the problem occurs. Heat can be transferred from the center mesh of the core to the outside mesh of the core by (natural) convection but from there it must be transferred out of the core by conduction (in the solid material calculation) It is expected however, that the convective heat transfer from the coolant to the reflector is the main heat transport mechanism in decay heat removal problems. Apparently, this form of heat transport can be neglected in gas-cooled reactors. This is not the case in a liquid coolant cooled nuclear reactor.

5.3 Decay heat removal calculation input

The model for the decay heat calculations was originally planned to be same as used in the steady state calculations. It was planned to perform a restart from a steady state calculation with a power profile given by the steady state calculations result. However, the first results found were not satisfying, because the heat is not removed at a rate that

was expected and THERMIX eventually terminated because maximum temperatures were exceeded.

It was planned to make a benchmark of THERMIX with the code HEAT. Unfortunately the code HEAT isn't able to simulate an annular core or multiple materials as the reactor vessel or an argon gap. In the code HEAT only a cylindrical core, a coolant plenum and the graphite reflector are simulated. The core and plenum volume is closed, which means that no coolant can flow in or out. To make a good comparison with this code, the THERMIX model was modified to be similar to the HEAT model. This means that only a cylindrical core was simulated. The model used for the THERMIX decay heat removal calculations is summarized in Table 11.

Table 11. Summation of the THERMIX and HEAT input data used for the decay heat calculations

Description	THERMIX input	HEAT input
Core shape	Cylindrical	Cylindrical
Materials used	4: pebble bed, graphite reflector, air layer, temperature boundary layer	3: pebble bed, graphite reflector, natural convection and radiation boundary
Core size radius/height (m)	3.60 / 7.50	3.60 / 7.50
Height bottom reflector (m)	1	1
Height top reflector (m)	1	1
Thickness outside reflector (m)	1	1
Mesh form	uniform	uniform
nr of meshes in z-direction of the core (cm)	75	120
Mesh height in core and reflector (dz) (cm)	10	6.25
nr of meshes in z-direction of the core (cm)	18	30
Mesh size in r direction (dr) (cm)	20	12
Starting temperature core (°C)	950	950
Starting temperature reflector (°C)	950	950
Starting temperature air layer (°C)	500	n.a.
Boundary temperature (T at infinity) (°C)	25	25
Power profile	Result from st.st. THERMIX calculation	Analytical calculation
Decay heat calculation	Way-Wigner (radiation time 1.5 hours)	DIN (1990)
Pebble packing fraction in the core	0.6	0.6
heat transfer value in boundary layer.	1000	Calculated (natural convection, radiation)
Emissivity (in boundary layer HEAT, in air layer THERMIX)	0.8	0.8
Time step size (s)	1 (t < 5 h), 5 (t > 5 h)	0.25 s / 0.5 s (additional salt plenum)
Restart (nr. of time steps)	n.a.	7200
Number of time steps per output result	10	10
Height of additional salt plenum above the core (second case)	n.a.	7.5 m

To investigate the effect of an additional salt plenum on the decay heat removal capacity calculations were not only performed on a pebble bed with salt coolant but also on a pebble bed with an additional salt plenum. It is expected that the additional salt adds

thermal inertia which will enable the pebble bed to remove more heat. Therefore two cases are modeled in HEAT. One without, and one with a 7,5 meter high salt plenum.

Time step size

The time step size was chosen to be sufficiently small to get accurate results, and large enough to prevent very expensive computation times. It was decided that the 0.25 time step size is accurately enough for the decay heat calculation for the pebble bed without additional salt plenum and a time step of 0.5 seconds is decided to be accurately enough for the calculations with additional salt plenum in heat. In THERMIX a time step of 1 sec was decided to be accurately enough.

Outside temperature boundary conditions

In THERMIX a constant boundary temperature was chosen. The heat transfer from the graphite to the air layer is then given by heat conduction and thermal radiation. Thus, no natural convection is simulated. This was not possible, because in THERMIX only a constant value for the heat transfer coefficient can be defined (see equation (A.19)), the heat transfer coefficient from natural convection (or radiation) is not constant. Neglecting the natural convection therefore only leads to small errors because thermal radiation is the dominant heat transfer mechanism. In HEAT, the temperature boundary condition is given by thermal radiation and natural convection.

Fuel temperature

In THERMIX the fuel temperature is the surface temperature, actual fuel temperatures will be higher. The fuel temperature in HEAT is assumed to be uniform. There is no thermal transient between the surface and the center of the pebbles. This means that pebble surface temperatures are overestimated and the maximum fuel temperature (at the center of the pebbles) is underestimated. Heat transfer from the pebbles to the salt is dependent on the temperature difference between the surface of the pebble and the liquid salt coolant local temperature. The heat transfer can therefore be overestimated. This must be taken into account, while analyzing the results.

Salt plenum

The original THERMIX input has a reasonable amount of additional salt to add thermal inertia to the core. In fact it can be compared with a pool type reactor. In HEAT a salt plenum can be simulated. The top reflector must then be removed. In THERMIX large salt plenums are not so easily defined, since they are only allowed to be one mesh high. Thus, THERMIX calculations were performed for the original (chap 4) input and the pebble bed without additional plenum only. With HEAT calculations were performed for the pebble bed core with and without additional salt plenum.

5.4 Results of Decay Heat Calculations

The results of the decay heat removal calculations are presented in this paragraph. First the results obtained with the thermal hydraulics code THERMIX and the original input are discussed, then the results obtained from a comparison between THERMIX and HEAT are discussed, then the HEAT results will be discussed and a comparison is made with the decay heat calculation performed on the AHTR.

5.4.1 Results from decay heat calculations with original THERMIX input

In Figure 28 the results of the THERMIX decay heat calculations are shown. Both the annular and the cylindrical core are shown. The starting conditions were the steady state results acquired in paragraph 4.3. It can be seen that for both the cylindrical and the annular core the maximum permissible fuel temperature is reached within 15 hours. To be able to verify the results obtained, calculations are performed in HEAT and THERMIX in a comparable geometry. These comparison results are shown in the next paragraph.

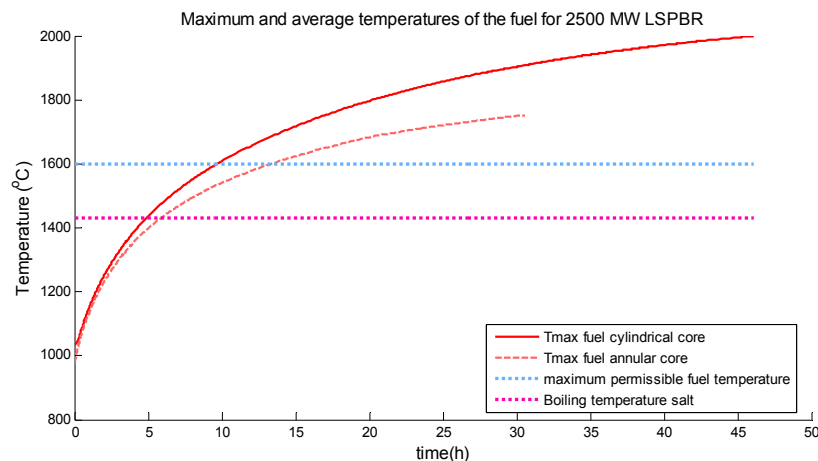


Figure 28. Results from THERMIX decay heat removal calculations with the original steady state input.

5.4.2 Results of THERMIX and HEAT comparison calculations

Here the results are shown of the comparison calculations between THERMIX and HEAT. The operational power was set to be 1000 MW. In Figure 29 the maximum fuel temperature transients are shown for both calculations. The calculations were started from a uniform reactor core and reflector temperature in both cases of 950 °C. The maximum temperature reached in the THERMIX calculation is 1215.5 °C, in HEAT the maximum temperature is 1116.1 °C. The total temperature difference between maximum

and initial temperature in THERMIX is 1.6 times the total temperature different in HEAT.

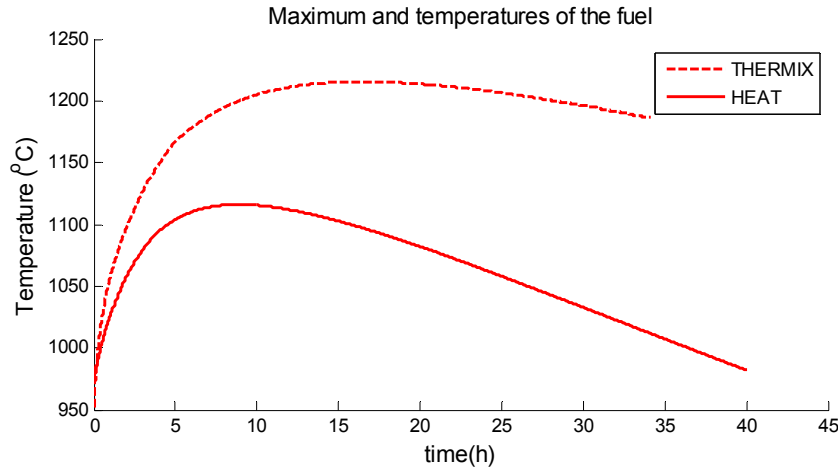


Figure 29. Comparison of THERMIX and HEAT maximum fuel temperature results for a cylindrical core (without additional salt plenum) for 1000 MW.

In Figure 30 the total decay power and the heat flux are compared for both calculations. A difference can be seen in the decay power, which is larger for the code HEAT. This can be explained by the differences in calculation method. While the calculation method of HEAT is based on an long irradiation period (or constant operating period), the Way-Wigner method used in THERMIX is set to calculate the decay heat after an irradiation time of 1.5 years.

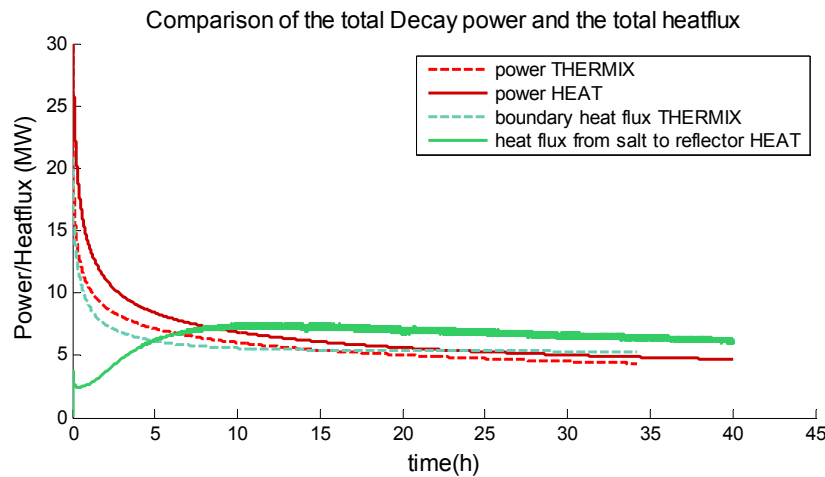


Figure 30. Comparison of the decay power and heat fluxes in THERMIX and HEAT

The heat fluxes shown in this figure cannot easily be compared. The heat flux of THERMIX is the total boundary heat flux. It starts of at a large value because the reflector is very hot compared to its surroundings starts to cool (uniform starting temperature of 950 °C), but remains below the decay power line up to approximately 15 hours. The heat flux from HEAT is the total heat flux from the salt to the reflector. All

heat from the graphite pebbles inside the core is removed by convective heat transfer by the salt. There is no heat conduction between the pebbles separately between the pebbles and the reflector. It starts at zero (since at $t = 0$ the temperature in both regions is equal ($950\text{ }^{\circ}\text{C}$)), increases fast as the liquid salt is heated by the decay heat and starts to flow. The heat flux increases further with temperature of the fuel and salt. A decrease in heat flux is seen when the fuel temperature decreases.

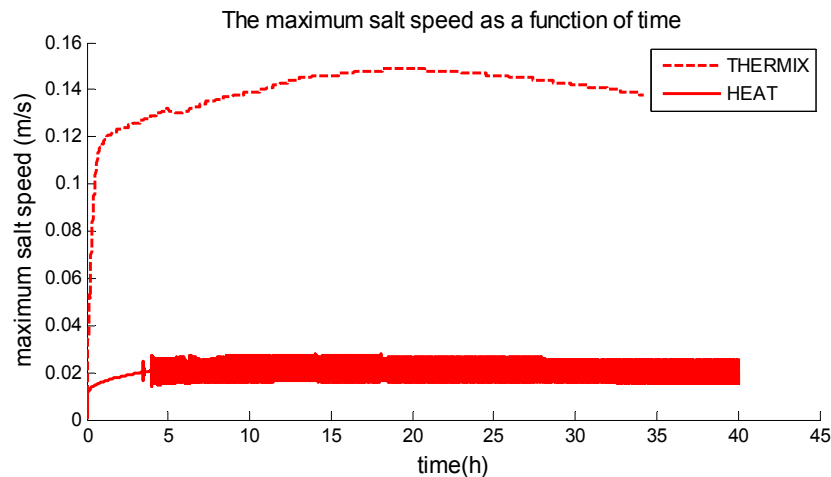


Figure 31. Comparison of maximum speed during decay heat calculations in THERMIX and HEAT.

In Figure 31 a comparison is shown between the maximum speed inside the pebble bed as calculated by THERMIX and HEAT. The maximum speed calculated by THERMIX is much larger than calculated by HEAT. This difference can be explained by the fact that the friction factor in THERMIX is based on the pressure drop during a steady state calculation. In HEAT this relation was implemented, but besides that also additional terms in the momentum equation are the viscous stress and molecular diffusion. These values could be unnecessary when these are accurately enough represented by the friction term in THERMIX. Since that is not sure, the terms for viscous stress and molecular diffusion were kept in the equation. It is possible that the velocity calculated in HEAT is underestimated. The heat transfer from the liquid salt will then be overestimated.

In THERMIX heat must be transported out of the pebble bed to the reflector via conduction in the solid material. In HEAT the heat produced must be transported from the pebble via (convective heat transfer with) the liquid salt. From the comparison between HEAT and THERMIX and the concerns about THERMIX mentioned in paragraph 5.4.1 it was concluded that convective heat transfer is the main heat transfer mechanism from the pebble bed to the reflector. It is therefore more likely that the results of HEAT are more accurate. It was decided to perform the decay heat removal calculations with HEAT with increased reactor power.

5.4.3 HEAT results decay heat calculation pebble bed

Two cases are investigated. The first case considered is a decay heat calculation on a pebble bed with the enclosed coolant with a surrounding graphite reflector. The second case considered is a decay heat calculation on the pebble bed with an additional 7,5 m high salt plenum on top of the pebble bed. Various initial power levels are simulated for each case, to investigate the thermal transients resulting from these power levels. All simulations were run for 40 hours of real time.

The decay heat removal calculation was performed for the pebble bed without extra salt plenum for initial powers from 500 MW until 2500MW. In Figure 32 the maximum fuel temperatures as a function of time for different initial powers are shown. The coolant temperatures do not differ much from the fuel temperatures. After a few hours, the differences in maximum temperature between the coolant and the fuel will be less than 2°C for most cases.

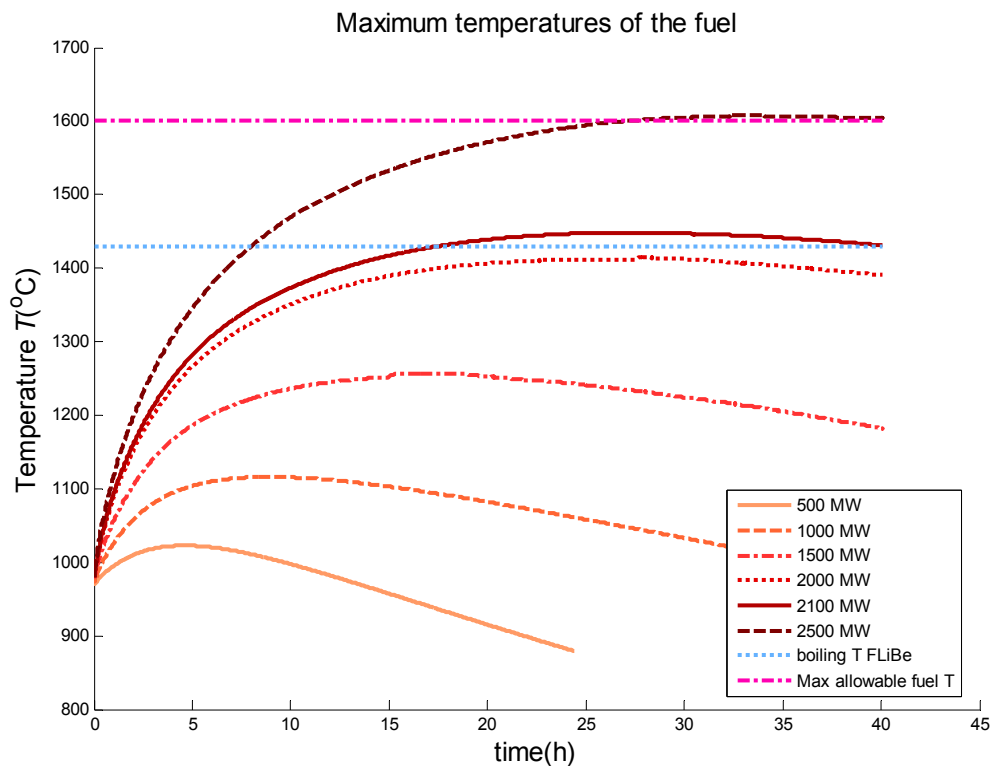


Figure 32. Transients of the maximum fuel temperature for different initial operating powers (500 – 2500 MW) for the Decay Heat Removal simulation of case A.

The thermal transients show an increase in core temperature over the first few hours to reach a peak temperature followed by a gradual cool down. At first the heat transfer from the coolant to the reflector is insufficient to compensate for the decay power produced inside the core. The salt and core are heated and a natural convection flow is induced

inside the core. Because of the thermal inertia of the salt the heating of the core will not be a quick process but will take several hours. The maximum is given in Table 12.

Table 12. Maximum fuel and coolant temperatures reached and time at which these temperatures are reached for different initial powers in case A.

Initial Power (MW)	Max fuel temperature (°C)	Time at max temperature (h)	Max coolant temperature (°C)	Time at max. coolant temperature (h)
500	1023	4.5	1023	4.5
1000	1116	8.6	1116	8.6
1500	1257	16.1	1253	17.3
2000	1415	27.8	1412	24.8
2100	1448	26.0	1447	26.0
2500	1607	33.3	1606	33.1

When the flow speed induced by natural convection increases, the convective heat transfer at the reflector wall will increase and eventually the heat transfer to the wall will exceed the decay heat power produced in the fuel. Then, the coolant and the fuel will gradually cool. It can be seen that only in the 2500 MW case the maximum permissible fuel temperature (1600 °C) is reached. However, another limiting temperature in the LSPBR is the boiling temperature of the liquid salt coolant, FLiBe (1430 °C). This effect was not simulated in the code HEAT. Thus, since the coolant temperatures may not exceed the boiling temperature of the Liquid salt FLiBe, the highest permissible initial power to be produced in the LSPBR without extra salt plenum is 2000 MW.

5.4.4 Detailed results for 2000 MW initial power

When in Figure 32 the maximum fuel temperature transient of the 2000MW case is investigated, a small hop can be identified after 27.5 hours. This temperature hop will be clarified below. The core heats up after shutdown and soon a very strong temperature gradient is visible in the reflector. The salt temperature remains fairly uniform during the simulations. At the bottom of the reactor core however the coolant has a temperature gradient which is the result of the bottom boundary condition ($T_{bc} = 500$ K). When the salt is cooled from below, natural convection is not induced. The salt directly at the bottom will therefore not start to flow.

The maximum speed of the liquid salt coolant is depicted in Figure 33. Initially the flow speed is zero. By natural convection, the maximum speed slowly increases up to 2.5cm/s. In the above subfigure, the maximum speed is shown for the whole time range. The slowly increasing natural convection circulation is depicted in Figure 34. When the time precedes the lower part of the reactor is cooled efficiently (influenced by low local power and cold low boundary of 500 K). In Figure 35 can be seen that the coolant at the bottom (which is cooled from below doesn't participate in the natural circulation and almost

doesn't move. It can also be seen that the center of the natural circulation has moved to the outside of the reactor core. This implicates an increasing maximum speed at the reactor core wall.

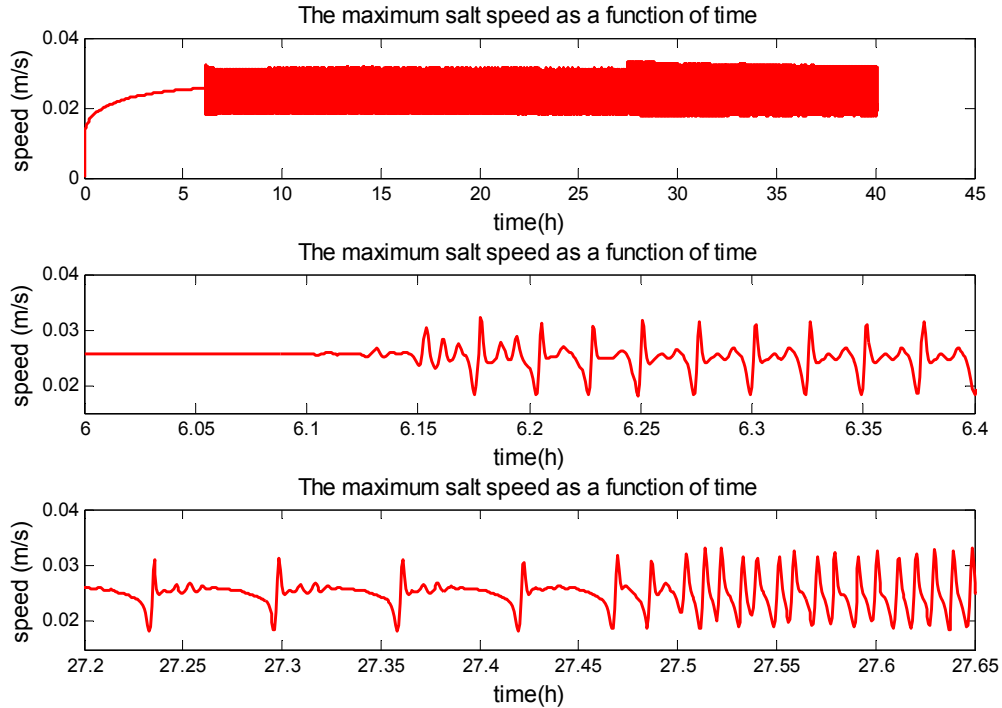


Figure 33. The maximum speed of the liquid salt as a function of temperature as a function of time for an initial power of 2500 MW. Above, the maximum speed is shown for the whole time range, a close up around 6 hours (center picture) and a close up of the period around 27,5 hours.

The speed appears to be randomly distributed after 6.2 hours. However, if a close up is made of the maximum speed around 6 hours (center picture of Figure 33) it can be seen that there is a returning pattern in the maximum speed. This returning pattern is caused by Rayleigh-Bernard convection plumes that drop from the top of the reactor core and are pushed to the outside of the reactor core by the dominating circulation. After several hours the top reflector is considerably cooler than the liquid salt coolant. Cooling a liquid from above will eventually induce Rayleigh Bernard convection. This effect is also shown in the flow field depicted in Figure 36.

The lowest subfigure of Figure 33 shows a close up of the time period around 27.5 hours. This is the moment that a hop can be recognized in the fuel temperature. A change in maximum speed pattern is observed. Before the change small plumes of cooler liquid salt coolant are pushed to the outside wall by the dominating natural convection flow (as shown in Figure 36). At ~27.5 hours a steady plume in the center top of reactor core starts to develop, which obstructs the dominant natural convection flow. The steady state

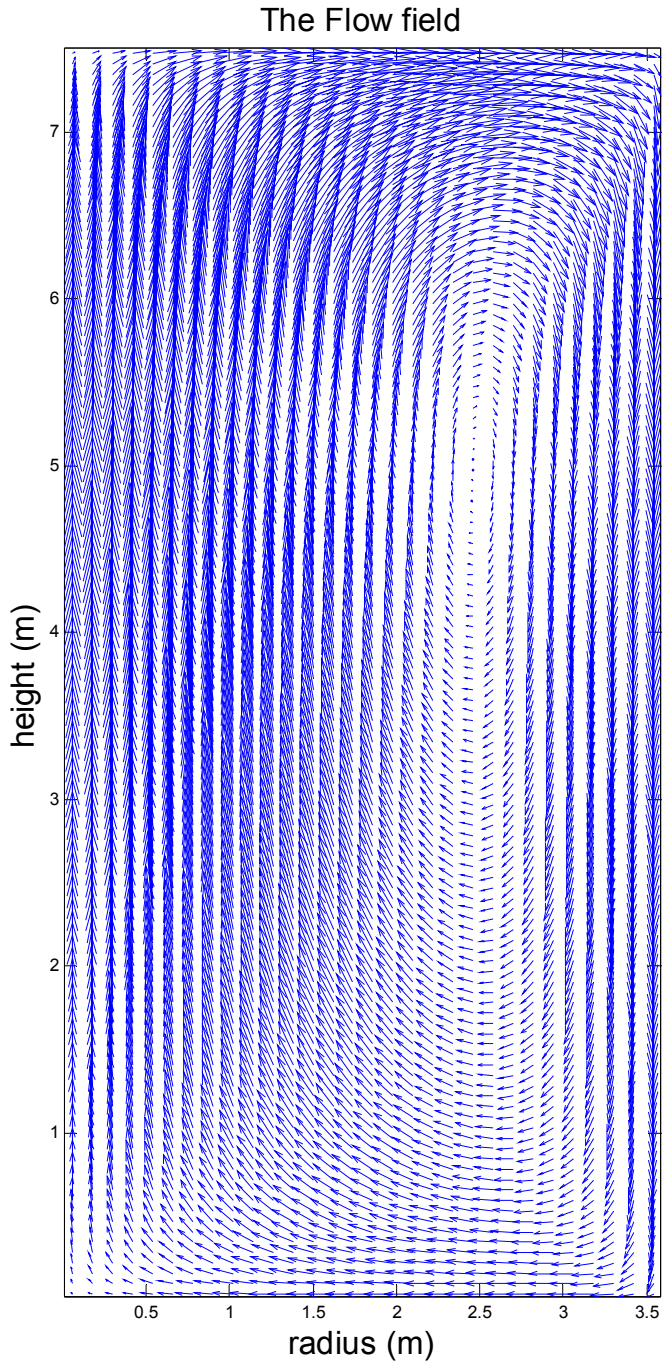


Figure 34. The flow field of the liquid salt coolant after ~ 140 seconds after shutdown at an initial operating power of 2000 MW, a steady natural convection circulation can be seen.

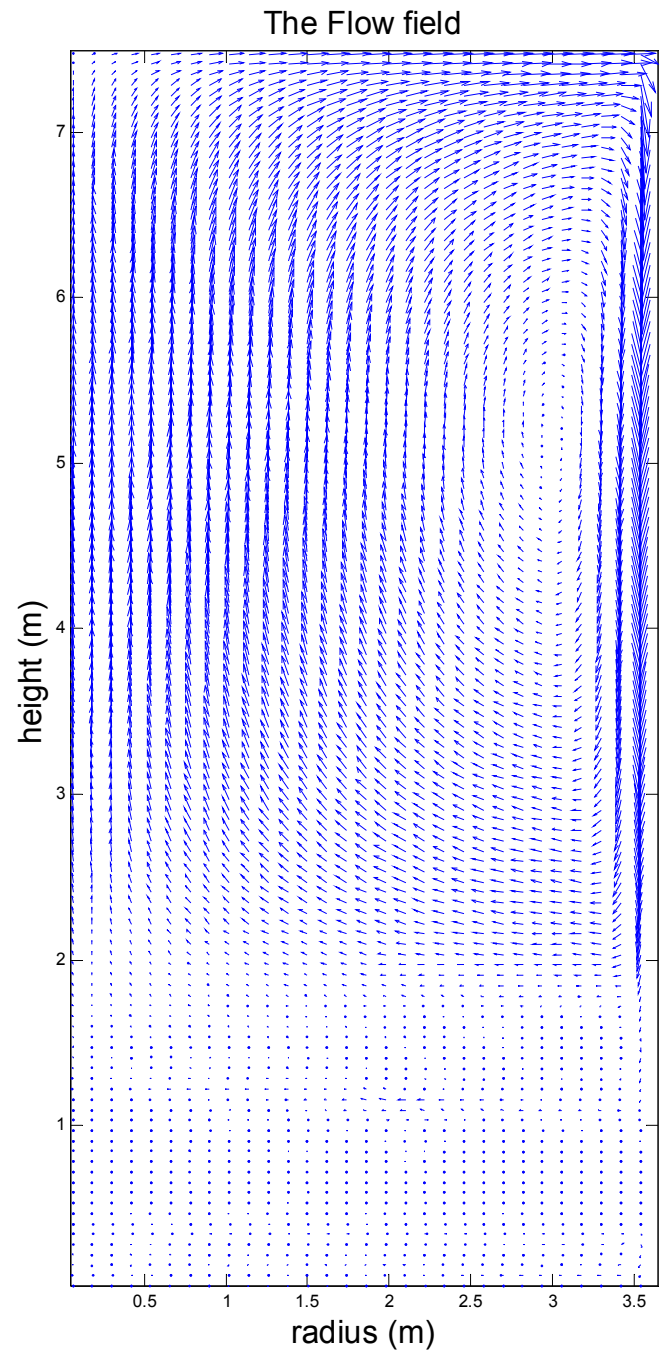


Figure 35. The flow field of the liquid salt coolant at 5 hours after shutdown, the centre of the convection circulation has moved to the outside. The salt at the bottom is cooler than the salt above and almost stopped flowing.

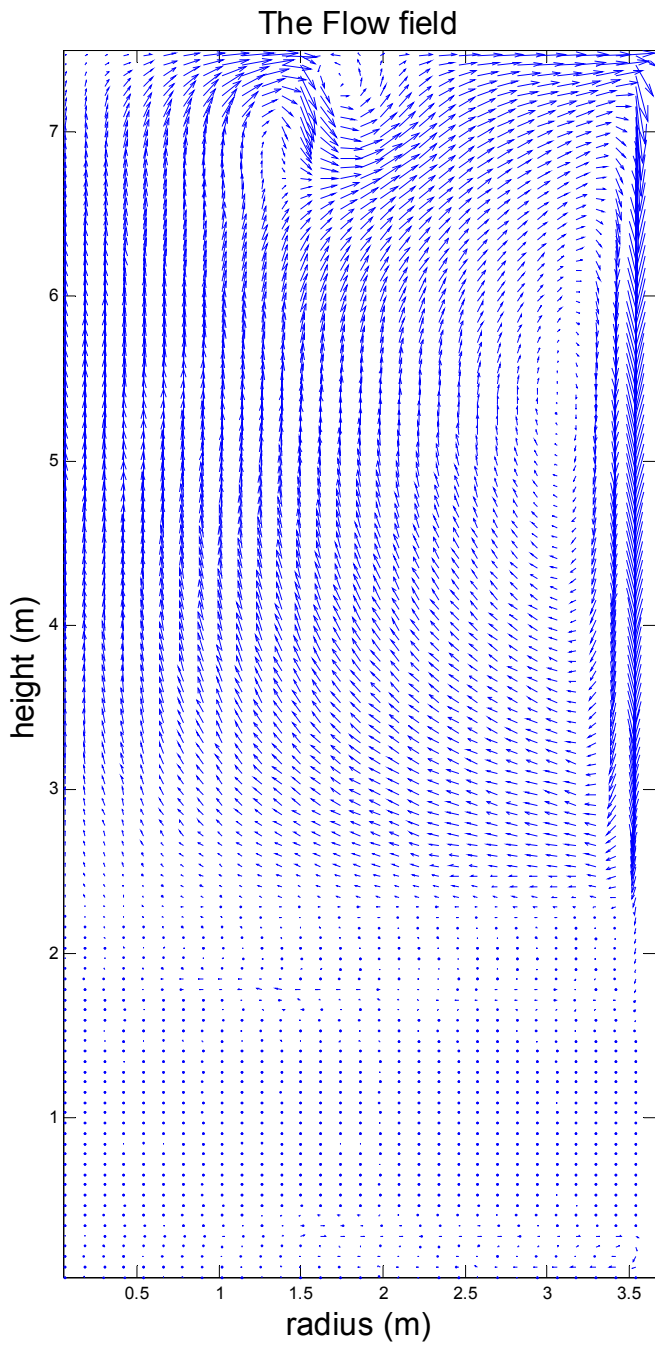


Figure 36. The flow field of the liquid salt coolant at 25 hours after shutdown at an initial operating power of 2000 MW, cold plume dropping from the reactor core top can be identified.

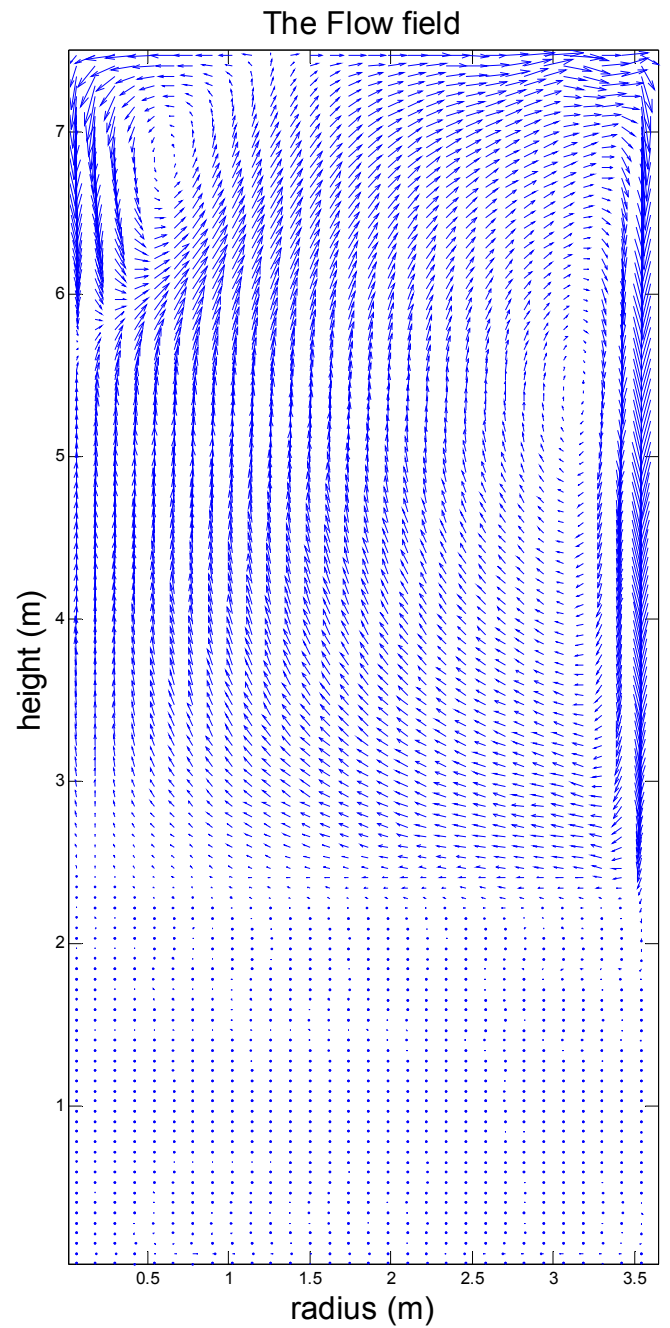


Figure 37. The flow field of the liquid salt coolant at 28 hours after shutdown at an initial operating power of 2000 MW, a steady cold plume dropping from the reactor core top centre has been developed.

plume is shown in Figure 37. This plume is probably the cause of the increasing difference between the maximum fuel temperature and the coolant maximum temperature. The center of the core is cooled less efficiently with this obstructing plume in the way.

The geometry of the core in this simulation is highly simplified. Therefore no conclusions should be made about the precise moment at which a certain flow patterns will develop. In reality this process will be much more chaotic, but the effects described above will most probably take place.

Figure 38 compares the heat removal from the core with the heat load produced by the decay power. The heat removal from the core is represented by the total heat flux from the salt coolant to the graphite reflector. It can be seen that the heat flux increases as the maximum speed of the liquid salt increases. The quick jump in heat flux at the beginning of the simulation is also found at the beginning of the maximum speed graph. The heat flux becomes unstable after ~ 4 hours. These fluctuations are a result of the irregularities in the flow pattern inside the reactor core, thus Rayleigh Bernard convection has a large effect on the heat flux.

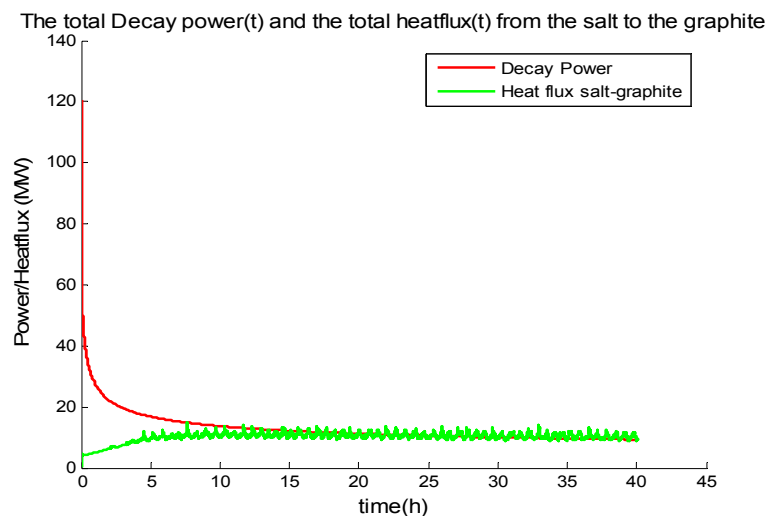


Figure 38. Comparison of the heat flux from the salt to the graphite reflector and the heat load generated by the decay heat after shutdown in a loss of forced cooling accident for 2000 MW initial operating power.

5.4.5 HEAT results for the pebble bed reactor core with additional salt plenum

It is expected that more decay heat energy can be stored inside the reactor core with a smaller increase of the coolant and fuel temperatures. If an extra salt plenum (or salt pool) of 7.5 m is added on top of the 7.5 m high reactor core. Without additional salt plenum 40 % of the pebble bed volume is the salt volume, with salt plenum the liquid salt volume is 140 % of the pebble bed volume). This means that the total volume of salt

present is multiplied by 3.5. The outer surface of the reactor core is also enlarged (1.68 the size of a reactor core without salt plenum), thus the heat transport from the salt to the graphite reflector is expected to increase considerably. The Decay Heat Removal calculation was performed for initial powers from 2000 MW until 5000MW. In Figure 39 the maximum fuel temperatures as a function of time for different initial powers are shown for a reactor core with additional salt plenum.

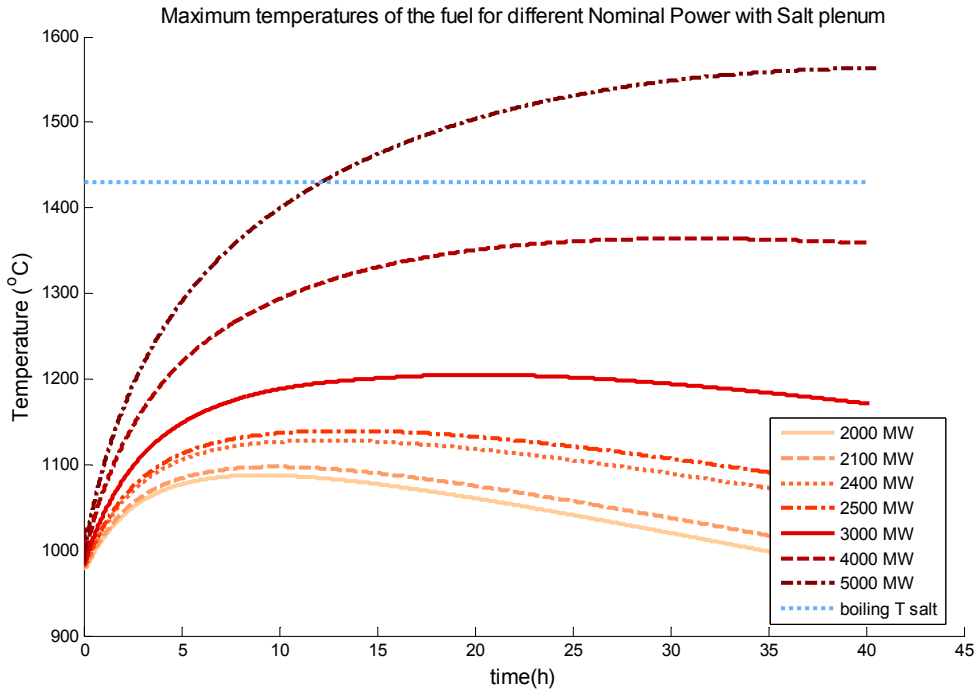


Figure 39. Transients of the maximum fuel temperature for different initial operating powers (2000 – 5000 MW) for the Decay Heat Removal simulation of case B.

The salt plenum introduces (as expected) extra thermal inertia. The maximum temperatures of the fuel reach much lower maximum values during the transients compared to case A where there is no extra salt plenum. In

Table 13 the maximum temperatures that were reached are summarized.

Table 13. Maximum fuel and coolant temperatures reached and time at which these temperatures are reached for different initial powers in case B.

Initial Power (MW)	Max fuel temperature (°C)	Time at max temperature (h)	Max coolant temperature (°C)	Time at max. coolant temperature (h)
2000	1087.7	9.1	1086.4	8.9
2100	1097.5	9.6	1096.2	9.6
2500	1193.3	13.4	1137.9	13.5
3000	1205.0	19.4	1203.6	20.0
4000	1364.2	30.0	1362.5	30.4
5000	Not reached		not reached	

Again, the maximum surface fuel temperature will be close to the maximum coolant temperature during operation. After a few hours, the differences in maximum temperature between the coolant and the fuel will be less than 3 °C for all cases.

Only in the 5000 MW case the boiling temperature of FliBe (1430 °C) is reached. To prevent boiling of the liquid salt coolant temperatures may not exceed the boiling temperature of the liquid salt FliBe. The highest permissible initial power to be produced in the LSPBR with an extra 7.5 m high salt plenum is then 4000 MW. The maximum coolant temperature reached in the transient is well below the boiling point of FliBe. This result is comparable to the result that was acquired by the calculation performed by University of California at Berkeley for a 4000 MW(t) core. It yielded a peak core temperature of 1325 °C (Forsberg et. al. 2004).

Detailed results for 4000 MW initial power

As in the case without salt plenum, the fuel temperature and the coolant temperature will not differ much from each other. The maximum speed and heat transfer do not fluctuate in the cases with additional salt plenum. Also, no Rayleigh Bernard plumes are identified. Apparently, the salt has a strong natural convection circulation which doesn't allow these plumes to develop. This also confirms a steady natural convection flow inside the pebble bed and the salt plenum. The velocity field for two different times is shown below.

Both flow fields are strikingly similar. The only difference is the absolute value of the speed at both times. The maximum speed has increased from 1.05 cm/s at 8 hours to 1.12 cm/sec at 40 hours. Some point of attention could be made about the simulations with additional salt plenum:

- The absence of irregularities in the flow in these graphs doesn't imply that in reality flow irregularities as Rayleigh Bernard convection do not occur. It must be kept in mind that the grid size in the z-direction in this case is twice the size of the z-direction grid size in the case without additional salt plenum.
- Here, the salt plenum is situated directly above the pebble bed core. In reality this would not be preferable because a top reflector should be placed on top of the core. The results will certainly be influenced when this will be taken into account.
- The 7.5 m high salt plenum should not necessarily be placed on top of the pebble bed. A salt plenum on both sides of the pebble bed can be considered. This would of course lead to different results.

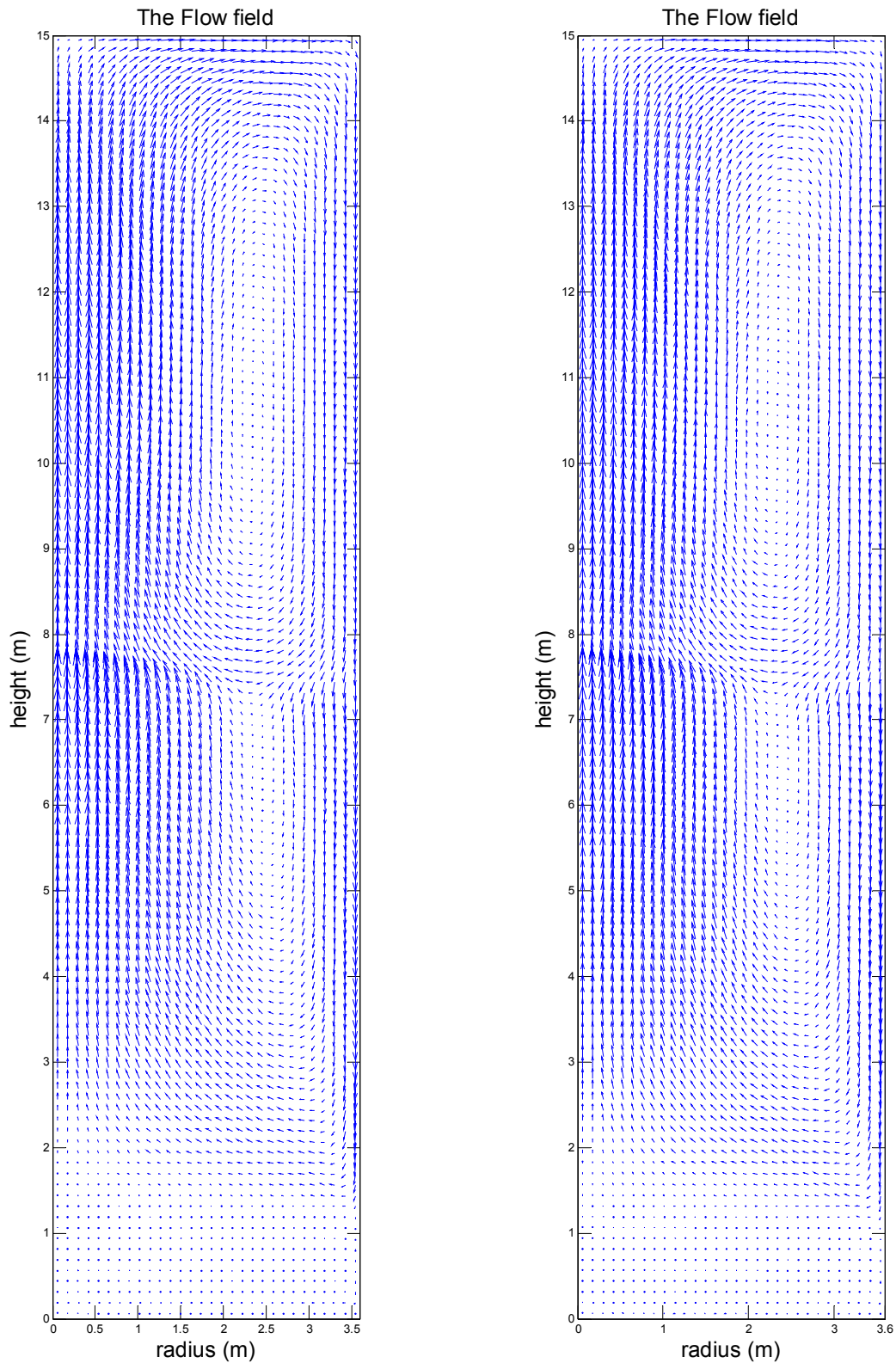


Figure 40. The flow field of the liquid salt coolant at 8 hours (left) and 40 hours (right) after shutdown, the flow field is steady, only the flow speed has increased a bit. The pebble bed boundary can be identified at 7.5 m height.

5.4.6 Comparison of the results for 2000 MW of both cases (with & without salt plenum)

The fuel reaches a temperature of 1415 °C without salt plenum for 2000 MW. When a 7.5 m high salt plenum is present, the maximum temperature of the fuel remains below 1090 °C with an initial power of 2000 MW. The transients of both cases are shown in Figure 41. The effect of the introduced additional thermal inertia is clearly visible. In fact the total temperature difference without plenum is ~ 3.4 times the temperature difference when a salt plenum is present.

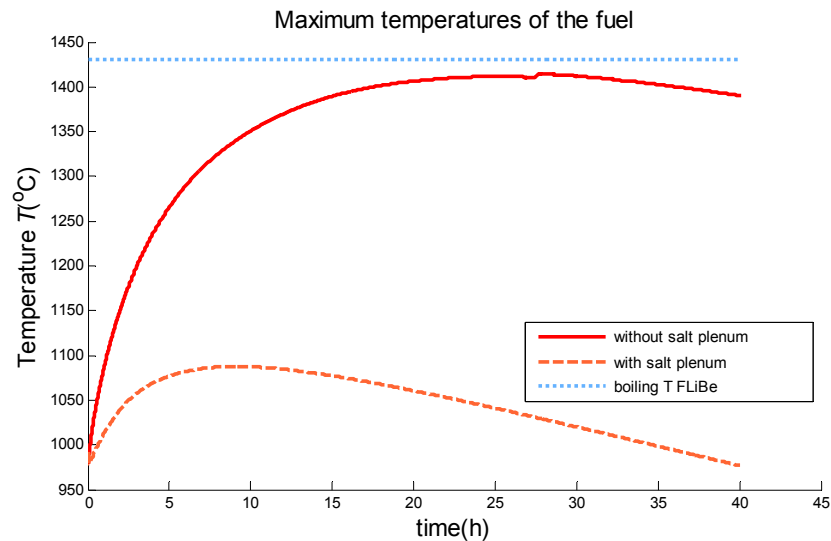


Figure 41. Comparison of the maximum fuel temperature transients for 2000 MW initial power of both cases.

The times at which the maximum temperatures occur are also different. Without plenum the maximum temperature is reached after 27.8 hours while with plenum the maximum fuel temperature is already reached at 9.1 hours. This means that not only the capability to absorb energy while remaining at low temperatures is increased, also is the capability increased to transfer the heat from the core to the graphite reflector. A comparison of the heat transfers in case A and B is shown in Figure 42. For clarity an extra line was added to the graph that presents an average of the heat flux in case A. This average was obtained by averaging the results of 10000 time steps (1000 output results).

It can be seen that the heat flux from the salt to the graphite increases when an extra salt plenum is added. The total surface over which heat can be transferred is much larger with additional salt plenum and there is more salt to remove the heat from the pebble bed. An increase in the heat flux of approximately 3.2 MW shortens the time when the heat removal line crosses the decay heat power line with approximately 18 hours.

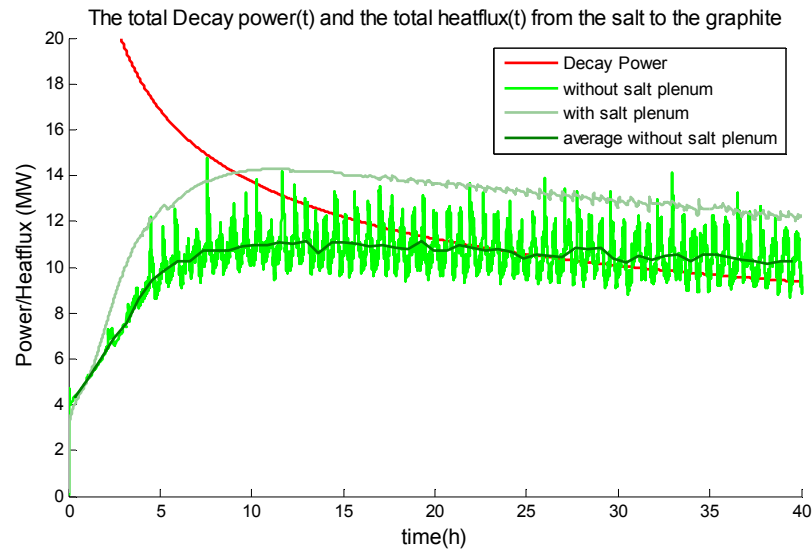


Figure 42. Comparison of the decay heat load and the heat transfer from the salt to the graphite for both cases with 2000 MW initial power.

The average heat flux is correlated with the speed of the liquid coolant at the surface of the reflector. In equation (C.14) can be found that the heat transfer coefficient is linearly dependent on the Nusselt number. The Nusselt number (which has a minimum value of two, see equation (C.10)) is dependent on $Re^{1/2}$, which is linearly dependent on the flow speed. Doubling the speed could therefore result in an increase in heat transfer of 1.4. It was found that without salt plenum the maximum speed fluctuates around 2.6 cm/s, while with salt plenum this maximum speed has decreased to approximately 1 cm/s. The average heat flux also decreased (~ 0.71 time the value without salt plenum), but because of the large increase in contact surface the total heat transfer has increased.

5.4.7 Comparison of the HEAT results for 2400 MW with salt plenum with results from AHTR

The results acquired with the thermal hydraulics can be compared with the results presented the status report on the AHTR (Forsberg et. al. 2004). Therefore the results of the decay heat removal simulation with an initial power of 2400 MW are plotted together with the decay heat removal simulation results of Oak Ridge. The maximum fuel temperatures are depicted in Figure 43. The results obtained are very different.

Differences that can be identified are:

- the starting maximum fuel temperature
- the maximum fuel temperature reached during the transient
- the time at which the maximum temperatures during the transient are reached

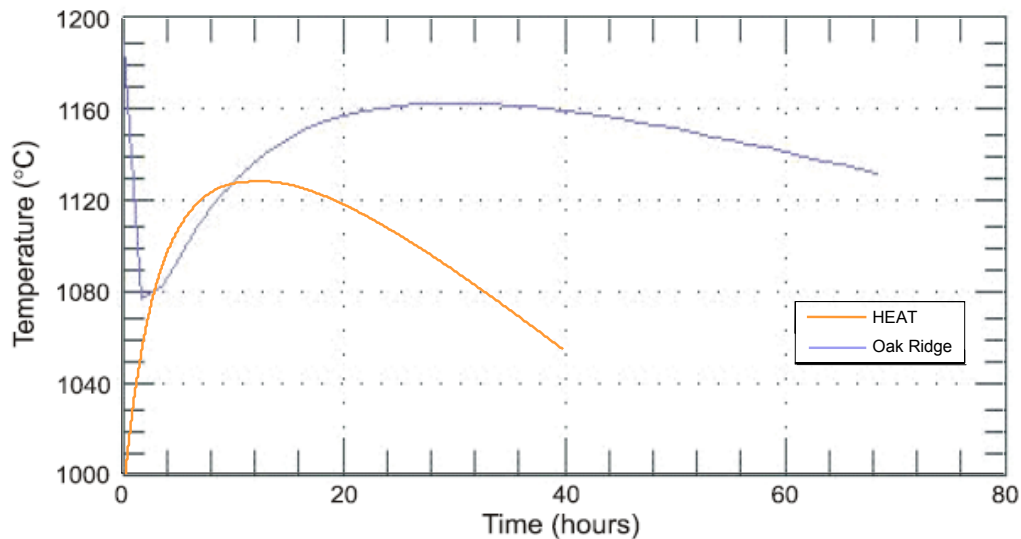


Figure 43. Comparison of the maximum fuel temperature transients of the Oak Ridge AHTR and the 2400 MW LSPBR simulation with salt plenum.

How are these differences clarified? The AHTR and the LSPBR are different designs with different geometry, model and calculation method. The main differences are:

- The liquid salt volume fraction in the AHTR is 6.56 % while (in HEAT) for the LSPBR this is 40%.
- The AHTR has prismatic fuel with coolant pipes, the LSPBR has fuel pebbles. Differences in flow resistance lead to differences in results.
- The AHTR has an annular core, the LSPBR model in the decay heat simulation has a cylindrical shape.
- No top reflector (above the pebble bed) was simulated in HEAT in the case with the additional salt plenum.
- The model in HEAT consist only of a pebble bed core, a salt plenum above the core, a graphite (1 m thick) reflector and a natural convection air boundary layer. The AHTR calculations were performed with much more detail: For example: the reactor vessel, the argon gap, the guard vessel and the reactor vessel auxiliary cooling system (RVACS) were modeled.
- Oak Ridge used the Graphite Reactor Severe Accidents Code (GRSAC), with a 3000 node 3D thermal hydraulics approximation to model the core and the RVACS
- Fuel temperatures in HEAT are uniform within the pebbles.

The difference in starting temperature can be explained by the fact that in HEAT a uniform core and reflector temperature was used as a starting condition. In reality this is a steady state temperature profile. The coolant temperature is then 900 °C at the top of the reactor and 1000°C at the bottom of the reactor, the fuel has a temperature profile which depends on the coolant temperature and the power profile while the reflector has a temperature dependent on the coolant, fuel temperature and outside boundary conditions.

The dip in the AHTR maximum fuel temperature transient is caused by the natural circulation in the core that will occur after the reactor shutdown. With a uniform starting temperature this dip will not appear.

The difference in maximum fuel temperature reached during the transient can be explained by noting that the code HEAT uses uniform fuel temperatures while in reality these temperatures are not uniformly distributed inside a pebble fuel element (cool pebble surface and hot center of a pebble). The difference in maximum achieved fuel temperature can also be explained when looking at the decay heat load and the heat removal from the core.

A comparison between the heat flux from the salt to the graphite reflector calculated in HEAT and the heat removal capacity calculated by Oak Ridge is shown in Figure 44. Again the heat removal is not easily compared, heat removal calculated by Oak Ridge is the RVACS heat removal capacity, which is the capacity of the auxiliary cooling system to remove heat from the core (this explains difference in heat removal at $t = 0$).

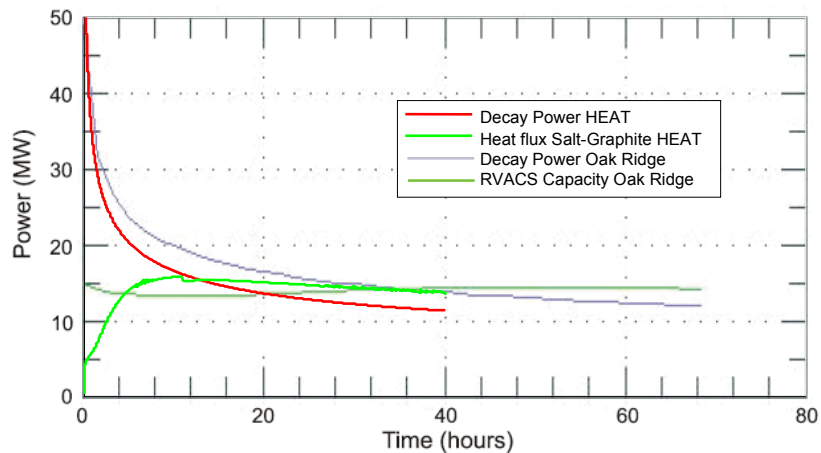


Figure 44. Comparison between the Decay heat load of the Oak Ridge calculation, the Decay heat load calculated with HEAT (2400 MW with additional salt plenum), the heat removal capacity of the Oak Ridge calculation and the heat flux from the salt to the reflector in the HEAT calculation.

Also the decay heat load of the HEAT and Oak Ridge calculations are shown. The decay load of Oak Ridge is larger than the decay load calculated with HEAT. The decay heat calculated for the AHTR decay heat removal calculations is approximately 20% larger than the decay heat calculated in HEAT. Apparently another calculation method was used by Oak Ridge to calculate the decay heat load. It is logical the maximum fuel temperatures will be higher when the decay heat load is larger, when compared with the 2400 MW case.

The heat flux from the salt calculated by HEAT is larger than the RVACS capacity of Oak Ridge, but not much larger. The heat flux calculated with HEAT exceeds the decay heat load from Oak Ridge after approximately 30 hours, which is the approximately at the same moment as when the RVACS line crosses the Decay heat removal line calculated by Oak Ridge.

Another difference is the time at which the maximum is reached of the fuel temperature transient. The transient calculated by Oak Ridge reaches its maximum at 30 hours, in the HEAT calculation the transient reaches its maximum after 15 hours. An explanation can be that there is more liquid salt present in the AHTR reactor vessel. The thermal inertia of the salt is able to absorb very large amounts of heat. An increase of the liquid salt volume slows down the heating of the core.

In return must the heat removal from the fuel be lower. The uniform fuel temperature in HEAT gives an over estimation of the fuel pebbles surfaces temperature. This leads to an over estimation of the heat flux between the liquid salt coolant and the pebble fuel. A lower heat flux between the fuel and the coolant could lead to a lower natural convection circulation. Lower coolant speeds close to the wall can lead to a lower heat transfer from the salt to the graphite reflector. The heat flux from the salt to the graphite can subsequently be reduced when extra heat barriers are included in the model, as a graphite liner, a reactor vessel, an argon gap, a guard vessel etc.

5.5 Conclusions on the decay heat removal calculations

The following can be concluded concerning the decay heat removal calculations:

- Convective heat transfer between the liquid salt and the graphite reflector is the main heat transfer mechanism from the pebble bed core. Neglecting this heat transfer is not justified for a liquid salt cooled nuclear reactor.
- THERMIX neglects convective heat transfer between the liquid salt and the reflector and is therefore not a justified tool for decay heat calculations on liquid salt pebble bed reactors.
- HEAT neglects conduction between the separate pebbles and between pebbles and the reflector. Since the contact surface between the pebbles is very small and since the convective heat transfer is the dominant heat transfer mechanism this is justified.
- Both HEAT and THERMIX use momentum equations that are not 100 % justified. In THERMIX the momentum equation is a steady state equation, where the friction in the flow is based on an empirical relation equal to the pressure drop at steady state. In HEAT the momentum equation is time and speed dependent and additional terms besides the friction term of THERMIX is used for the calculation of momentum transport. Compared to THERMIX the friction is overestimated, speeds in the flow are possibly underestimated.
- HEAT is the preferred code to perform decay heat calculations. Unfortunately, HEAT is only able to perform decay heat calculations on a cylindrical pebble bed and graphite reflector with (optionally) an additional salt plenum directly on top of the

pebble bed. A more accurate description of the core in decay heat calculations is desirable

- When a liquid salt cooled pebble bed without additional salt plenum is considered, a maximum nominal power of 2000 MW can be passively removed from the reactor core. Irregularities in the flow influence the heat transfer and can lead to higher maximum fuel temperatures.
- If an additional salt plenum is added directly on top of the pebble bed, the capacity to transfer decay heat away from the reactor core increases. A maximum nominal power of 4000 MW can now be passively removed from the reactor core. This increase in heat removal capacity is caused by the additional salt (added thermal inertia) and increased contact surface between the liquid salt and the reflector. The average heat transfer (per square meter) does not necessarily increase.
- Compared to the AHTR, maximum temperatures reached during a transient are lower and the maximum is reached faster. The decay heat calculated is different, but the heat transfer is fairly similar. HEAT is a simplification of a real pebble bed reactor, a more detailed description of the liquid salt pebble bed reactor core, reflectors, vessel and auxiliary cooling systems will give a more realistic view on its decay heat removal capacity.

6 Conclusions

The conclusions concerning this thesis can be split up in 4 parts:

- A selection for the first candidate liquid salt coolant in the LSPBR was made. The liquid salt best fit for the LSPBR is LiF-BeF_2 . Of the candidate salts it has the highest moderating ratio, the largest k-infinity values, a negative voiding reactivity coefficient and the strongest total temperature coefficient. If complete removal of the coolant can be prevented the result of voiding coefficient of the coolant by temperature increase and the temperature coefficient by the Doppler effect remains negative until a fuel loading of $\sim 3,9$ g HM/pebble.
- An investigation of the dimensioning of the LSPBR was made. The size of a pebble bed is not restricted by its pressure drop. If a pebble bed height of 7.5 m is chosen with a pebble bed volume of 300 m^3 the pressure drop will be less than 1 bar and a pumping power of less than 0.1 % of the total power of 2500 MW is needed to overcome this pressure drop.
- An investigation of the reactor physics and thermal dynamics in steady state operation was made by performing steady state calculations on the LSPBR. It was found that the flux profiles have their maximum in the center of the core and that the power density is largest in the center. However, the volume of salt is smallest in the center, thus the high power density does not contribute much to the total heat production. A movement of the flux maximum towards the outside of the core would be desirable. Because the radial flux profile is more flat for the annular core, a lower maximum power density and lower maximum fuel temperatures is found in the annular core. The axial flux profiles have the same shape for both the cylindrical and the annular core. Because of lower fuel temperatures the annular core is the preferred core shape for the Liquid Salt Pebble Bed Reactor. Compared to the AHTR the annular LSPBR has lower maximum fuel temperatures.
- An investigation was made of the capability of the reactor core to remove the decay heat by passive decay heat removal. It was found, from decay heat removal calculations performed with HEAT, that the maximum allowable nominal power is 2000 MW without salt plenum and 4000 MW with salt plenum. Irregularities in the flow influence the heat transfer and can lead to higher maximum fuel temperatures. Convective heat transfer between the liquid salt and the graphite reflector is the main heat transfer mechanism from the pebble bed core. Neglecting this heat transfer like is done in THERMIX is not justified for a liquid salt cooled nuclear reactor. Compared to the AHTR, maximum temperatures during a transient are lower and the maximum is reached faster.

7 Recommendations

During the investigations performed in this thesis new questions have raised which could be investigated in the future. They will be stated in this chapter:

- During the period from first startup until equilibrium the ${}^6\text{Li}$ concentration caused by the presence of this element in FLiBe has a negative effect on the reactivity. The impact on reactivity and stability can be further investigated.
- The possibility of floating pebbles should be investigated. It is possible that the pebbles will remain in a closed pack when forced cooling is applied, but they could start to float when forced cooling is lost. Floating of the fuel can lead to an increase of reactivity. A LSPBR could take advantage of this effect, for example pebbles could float into an absorber environment, which would stop the nuclear chain reaction.
- For this thesis, existing fuel pebbles from HTR programs are used inside the pebble bed core. Changing the pebbles size or composition influences the reactor physics and thermal hydraulics, possibly in a positive way. The effects of changing the fuel pebbles could be studied.
- If complete voiding can be prevented, other salts might be interesting for the cooling of a nuclear reactor. Three other salts showed negative total temperature coefficients. Before making the final selection of the liquid salt that will cool the LSPBR, a more detailed investigation of other, possibly less toxic and less expensive salts can be made. Especially three component salts can be promising.
- The cross-section library was produced by interpolating the solid state surface temperatures. It is recommended to replace this library by a library which is produced from different temperatures. Besides the surface temperature of the pebbles, also the local temperature of the liquid salt coolant, and the temperature profile inside the pebble should be taken into account. The library produced is a cell-weighted cross-section library. In new investigations the influences of energy spectra per zone inside the reactor core could be taken into account.
- In this thesis steady state calculations were performed with homogenous fuel and additional poison to adjust the over reactivity in the core and stabilize the reactor power at 2500 MW(t). In reality this over reactivity will be adjusted by control rods and pebble flow. This will influence the flux profile and can lead to higher local maximum fuel temperatures. Also, fresh fuel will be added from the top of the reactor, which will move the flux profile maximum to the top. The consequences should be investigated.
- In this thesis burnup of fuel in the reactor core was not taken into account. There are different fuel-cycles possible for the LSPBR. A once through then out principle can be used for the fuel pebbles, but pebbles could also be reshuffled during operation by

reusing pebbles which still contain enough fissile material. Different locations could be used when adding pebbles to the top of the reactor core. For example, used pebbles can be added in the center and fresh fuel pebble at the outside of the pebble bed to obtain a more flat power profile. The effects on the reactivity, temperature coefficients, burn up, flux and power profile of different fuel cycle options should be studied to obtain a preferred fuel management

- The vessel maximum and average temperatures could possibly be reduced by additional thermal blanket cooling systems inside the side reflector. A secondary closed loop of liquid salt could be added to the inside of the reflector or a thicker reflector could be used. The temperature dependent properties of the materials used in the LSPBR should be studied
- A thermal hydraulics code should be developed (or an existing code should be modified) which is capable of accurately describing the flow and heat transfer in a liquid coolant cooled pebble bed reactor. If achievable, it must be able to:
 - Perform temperature calculations that include all forms of heat transfer.
 - Perform momentum calculations with verified momentum equations.
 - Communicate with a neutronics code for coupled calculations.
 - Work with different reactor geometries. Besides a pebble bed and salt plenum also pipes, matrix fuel and porous reflectors can then be simulated, which also gives an opportunity to make benchmark calculations of the AHTR.
 - Simulate two phase flow. Boiling effects of the liquid salt can then be investigated. Now maximum temperatures are restricted by the boiling temperature of the liquid salt.
 - Simulate the whole primary coolant loop. During LOFC accidents, liquid salt will start to flow by natural convection, and will not remain in the reactor core. Passive cooling in the rest of the primary loop could increase the decay heat removal capacity.
 - Simulate additional passive auxiliary cooling systems. This will also have an effect on the decay heat removal capacity.
- Besides decay heat removal accidents, other accident scenarios should be investigated. Since there is a total negative temperature reactivity coefficient, how will the reactor react on reactivity insertion? How does the reactor during steady state operation react on increased coolant mass flow? Also beyond design basis accidents could be studied.
- Besides the LSPBR with forced cooling, the concept of a liquid salt cooled pebble bed reactor with natural convection flow could be studied. The absence of active pumps can be an advantage regarding passive safety and ease of operation. It should be examined what maximum powers can be generated in such a reactor. For this application it is also interesting to investigate the effects of possible boiling of the liquid salt.

Appendix A, The thermal hydraulics code THERMIX

The program THERMIX is divided in three parts. The first part (the main program) calculates the temperatures of the solid state material in the model. The second and third parts (incorporated in the convection part of the program) calculate the fluid flow field of the coolant and the coolant temperatures.

The temperatures, flow field and convective heat sinks/sources are calculated by solving energy equations, the momentum equation and the continuity equation. The spatial dependence is managed by discretizing into a number of meshes. Also, for time dependent calculations, time steps are discretized. The geometry of the (two dimensional) grid can be chosen to be orthogonal (x-y), or cylindrical (r- ϕ or r-z). In the convection part of the calculation however, only a r-z cylindrical geometry is allowed. In the following paragraph the theory used by THERMIX is described.

A.1 Heat transfer by conduction, the main program of THERMIX.

The solid state meshes in the calculation grid are divided in three different types of regions [1]:

1. Solid state zone
 - a. with flow
 - b. without flow
2. Hollow space
3. Boundary zones

The Solid state zones are homogenous material zones, where heat is transported by conduction, optionally with convective heat sources or drain. In the hollow spaces, heat transport is calculated similarly, except the heat is mostly transported by heat radiation (which is modeled as radiation conduction).

The Boundary zones are regions that are used as boundary conditions. The temperature is not calculated but constant and given. By defining a heat transport coefficient the boundary heat flux can be varied (Peterson, 1983).

A.1.1 Energy equations

The temperature profile of the solid state material is calculated by solving the energy balance equation for conduction. The energy balance equation which must be solved is (Verfondern, 1978; Peterson, 1983):

$$\rho c_p \frac{\partial T}{\partial t} = \nabla \lambda \nabla T + q \quad (\text{A.1})$$

here, ρ is the density, c_p is the heat capacity and λ the heat conductivity of the solid state material, T the temperature and q a heat source/sink. In equation (A.1), q is the combined heat source of nuclear heat production q_N and heat transfer by convection q_C . The total heat source/sink is the sum of both contributions:

$$q = q_C + q_N \quad (\text{A.2})$$

The nuclear heat source is given in the input by a power profile and the total power produced. In cylindrical coordinates (r - z geometry) the energy balance equation as used in THERMIX can be written as (Patankar, 1980):

$$\rho c_p \frac{\partial T}{\partial t} = \frac{1}{r} \frac{\partial}{\partial r} \left(\lambda r \frac{\partial T}{\partial r} \right) + \frac{\partial}{\partial z} \left(\lambda \frac{\partial T}{\partial z} \right) + q \quad (\text{A.3})$$

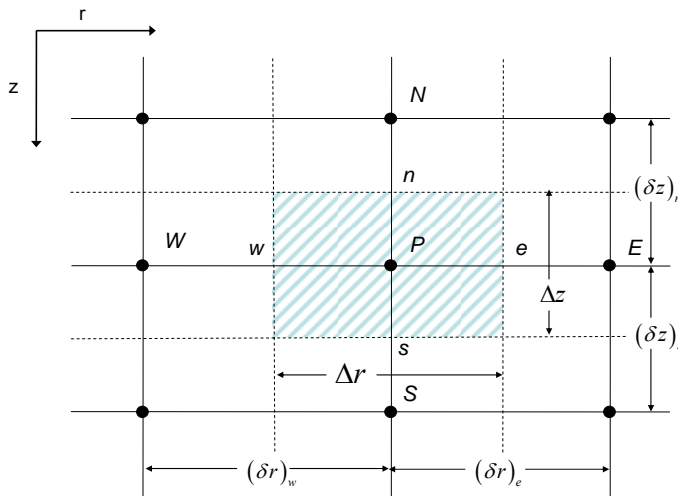


Figure 45. Discretization of the Solid state model in a cylindrical geometry, the location of the control volume and the control-volume faces are shown

When the problem has to be numerically solved the reactor is discretized for the cylindrical geometry as shown in Figure 45. For the unsteady case a time dependent relation must be found. Thus when given grid-point values of T at a certain time t are given, the values of T at time $t + \Delta t$ must be found. The “old” values of T at the grid points will be denoted with $T_W^0, T_P^0, T_E^0, T_N^0, T_S^0$, and the new (unknown) values at time $t + \Delta t$ with $T_W^1, T_P^1, T_E^1, T_N^1, T_S^1$. Because of cylindrical geometry the control volume over which is integrated is equal to $dV = 2\pi r dr dz$.

The discretization formula is derived by integrating equation (A.3) over the control volume shown in Figure 45 and over the time interval from t to $t + \Delta t$. Thus,

$$2\pi\rho c_p \int_w^e \int_n^s \int_t^{t+\Delta t} \frac{\partial T}{\partial t} r dt dz dr = 2\pi \int_w^e \int_n^s \int_t^{t+\Delta t} \left(\frac{1}{r} \frac{\partial}{\partial r} \left(\lambda r \frac{\partial T}{\partial r} \right) + \frac{\partial}{\partial z} \left(\lambda \frac{\partial T}{\partial z} \right) + q \right) r dt dz dr \quad (\text{A.4})$$

The left hand side of equation is

$$\rho c_p 2\pi \int_w^e \int_n^s \int_t^{t+\Delta t} \frac{\partial T}{\partial t} dt dz dr = \rho c_p (T_P^1 - T_P^0) \Delta V \quad (\text{A.5})$$

Here ΔV is the volume of the control volume; it is equal to $\frac{1}{2}(r_w + r_s) 2\pi \Delta r \Delta z$. Further integration of the right side of the equation leads to

$$\begin{aligned} \rho c_p (T_P^1 - T_P^0) \Delta V = & \\ \int_t^{t+\Delta t} \left[\left(\frac{\lambda_e (T_E - T_P)}{(\delta \ln r)_e} - \frac{\lambda_w (T_P - T_W)}{(\delta \ln r)_w} \right) 2\pi \Delta z \right] dt & \quad (\text{A.6}) \\ + \int_t^{t+\Delta t} \left[\left(\frac{\lambda_s (T_S - T_P)}{(\delta z)_s} - \frac{\lambda_n (T_P - T_N)}{(\delta z)_n} \right) (r_w + r_s) \pi \Delta r + q \Delta V \right] dt & \end{aligned}$$

In the above equation the equality $\partial(\ln r) = \frac{\partial r}{r}$ was used. It is assumed that the temperatures T_w, T_p, T_e, T_n and T_s vary with time from t to $t + \Delta t$ with:

$$\int_t^{t+\Delta t} T_p dt = [f T_P^1 - (1-f) T_P^0] \Delta t \quad (\text{A.7})$$

In the main program of Thermix instationary problems are solved with the Crank-Nicholson method. This means that f in the above equation is 0.5. Equation (A.7) then becomes:

$$\int_t^{t+\Delta t} T_p dt = \frac{T_P^1 - T_P^0}{2} \Delta t \quad (\text{A.8})$$

$$\begin{aligned} \rho c_p (T_P^1 - T_P^0) \frac{\Delta V}{\Delta t} = & \\ \frac{1}{2} \left[\left(\frac{\lambda_e (T_E^1 - T_P^1)}{(\delta \ln r)_e} - \frac{\lambda_w (T_P^1 - T_W^1)}{(\delta \ln r)_w} \right) 2\pi \Delta z + \left(\frac{\lambda_s (T_S^1 - T_P^1)}{(\delta z)_s} - \frac{\lambda_n (T_P^1 - T_N^1)}{(\delta z)_n} \right) \pi (r_w + r_e) \Delta r + q^1 \Delta V \right] & \quad (\text{A.9}) \\ + \frac{1}{2} \left[\left(\frac{\lambda_e (T_E^0 - T_P^0)}{(\delta \ln r)_e} - \frac{\lambda_w (T_P^0 - T_W^0)}{(\delta \ln r)_w} \right) 2\pi \Delta z + \left(\frac{\lambda_s (T_S^0 - T_P^0)}{(\delta z)_s} - \frac{\lambda_n (T_P^0 - T_N^0)}{(\delta z)_n} \right) \pi (r_w + r_e) \Delta r + q^0 \Delta V \right] & \end{aligned}$$

while rearranging this, the superscript 1 is dropped and T_P is the temperature at time $t + \Delta t$. The result is

$$a_P T_P = \left[a_E (T_E - T_E^0) + a_W (T_W - T_W^0) + a_N (T_N - T_N^0) + a_S (T_S - T_S^0) \right] + \left[a_P^0 - a_E + a_W + a_N + a_S \right] T_P^0 + q^0 \Delta V + q \Delta V \quad (\text{A.10})$$

where

$$\begin{aligned} a_E &= \frac{\lambda_e 2\pi\Delta z}{(\delta \ln r)_e}, \\ a_W &= \frac{\lambda_w 2\pi\Delta z}{(\delta \ln r)_w}, \\ a_N &= \frac{\lambda_n \pi (r_w + r_e) \Delta r}{(\delta z)_n}, \\ a_S &= \frac{\lambda_s \pi (r_w + r_e) \Delta r}{(\delta z)_s}, \\ a_P^0 &= \frac{2\rho c_p \Delta V}{\Delta t}, \\ a_P &= (a_E + a_W + a_N + a_S) + a_P^0 \end{aligned} \quad (\text{A.11})$$

In Thermix the numerical equations are formulated in terms of heat resistance elements W_{LT} [1]. The W_{LT} at every surface of the control-volume can be expressed in term of the coefficients a_E , a_W , a_N and a_S .

$$\begin{aligned} W_{LT,e} &= \frac{1}{a_E} = \frac{(\delta \ln r)_e}{\lambda_e 2\pi\Delta z} = \frac{\ln \frac{r_E}{r_P}}{\lambda_e 2\pi\Delta z}, \\ W_{LT,w} &= \frac{1}{a_W} = \frac{(\delta \ln r)_w}{\lambda_w 2\pi\Delta z} = \frac{\ln \frac{r_P}{r_W}}{\lambda_w 2\pi\Delta z}, \\ W_{LT,n} &= \frac{1}{a_N} = \frac{(\delta z)_n}{\lambda_n \pi (r_w + r_e) \Delta r} = \frac{(z_P - z_N)}{\lambda_n \pi (r_w + r_e) \Delta r}, \\ W_{LT,s} &= \frac{1}{a_S} = \frac{(\delta z)_s}{\lambda_s \pi (r_w + r_e) \Delta r} = \frac{(z_S - z_P)}{\lambda_s \pi (r_w + r_e) \Delta r} \end{aligned} \quad (\text{A.12})$$

A.1.2 The conductivity λ per region

The conductivity in the Solid state grid is calculated temperature dependently for every material. Since the grid knots are at junctions of materials the conductivity for each grid point in every direction is calculated as an averaged combination of the conductivity of the two meshes, where the control volume face through which the conduction must be calculated lies within, see also Figure 46. For example: the conduction through the n-face λ_n is calculated by averaging λ_1 and λ_2 , the heat conduction of material 1 and 2 [2]

$$\lambda_n = \frac{\lambda_1(r_P - r_W) + \lambda_2(r_E - r_P)}{(r_E - r_W)} \quad (\text{A.13})$$

here r_E, r_P, r_W are the r values of the points W, P and E.

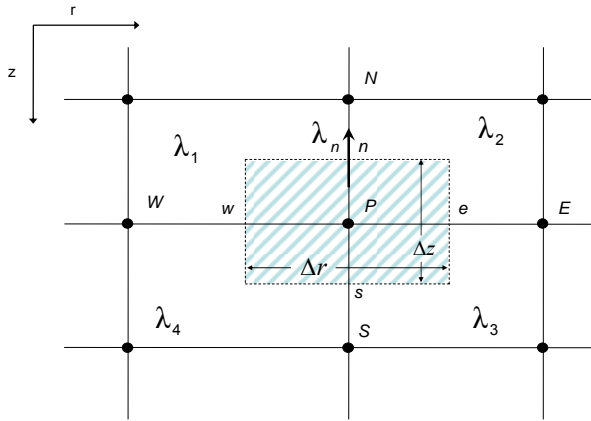


Figure 46. Discretization of the solid state model. The grid points lay at the junction of the material volumes, with different materials, temperatures, and material properties, as temperature dependent conductivity.

A.1.1.2 Solid state zone

In solid State zones the conductivity is calculated temperature and material dependently with a subroutine in the main program. For some solid state zones, as solid state zones with flow, the calculation of the conductivity is a bit more complicated. Here the calculation of the conductivity in the pebble bed is shown. In the pebble bed, the heat conduction when the reactor is in rest is λ_{ZS} (coolant flow is not taken in to account in this relation). λ_{ZS} is calculated with the Zehner/Schlünder relation (Verfondern, 1978; Struth 1998).

$$\lambda_{ZS} = (1 - \sqrt{1 - \varepsilon})(\lambda_C + \varepsilon\lambda_R) + \sqrt{1 - \varepsilon} [a_{bfl}\lambda_{fo} + (1 - a_{bfl})\lambda_P] \quad (\text{A.14})$$

here λ_C is the conductivity of the coolant, λ_{fo} is the conductivity of the solid material, λ_R is the conductivity by radiation (which is explained below) and λ_P the conductivity of the pebbles. ε is the coolant fraction and a_{bfl} is a value for the flattening of the pebbles at the contact points. The relation λ_P is given by:

$$\lambda_p = \frac{2.0\lambda_c}{N-M} \left[\frac{(BN-M)}{(N-M)^2} \ln \frac{N}{M} - \left(\frac{B-1}{N-M} \right) + \frac{B+1}{2M} (N-M-1) \right] \quad (\text{A.15})$$

with

$$M = B \frac{\lambda_c}{\lambda_{fo}}$$

$$N = 1 + \frac{\lambda_R}{\lambda_{fo}} \quad (\text{A.16})$$

$$B = 1.25 \left(\frac{1-\varepsilon}{\varepsilon} \right)^{\frac{10}{9}}$$

A.1.1.2 Hollow space

If the material consists of a hollow space, the conductivity of the material is not only defined by the material heat conduction but also by thermal radiation. The additional heat flux is defined by the relation for heat radiation between two parallel plates (Verfondern, 1978):

$$\lambda_R = \frac{c_s d}{\frac{2}{\varepsilon_s} - 1} \frac{\left(\frac{T_1}{100} \right)^4 - \left(\frac{T_2}{100} \right)^4}{T_1 - T_2}, \quad T_1 \neq T_2 \quad (\text{A.17})$$

$$\lambda_R = \frac{c_s d}{\frac{2}{\varepsilon_s} - 1} 0.04 \left(\frac{T_1}{100} \right)^3, \quad T_1 = T_2$$

here c_s is the constant of Stefan Boltzmann ($= 5.77\text{e-}4 \text{ W/cm}^2\text{-K}$ [4]), d is the distance between the walls over which radiation is applied, ε_s is the emission coefficient (must be entered manually) and T_1 and T_2 are the temperatures of both walls. The total conduction in a plenum is then

$$\lambda_{plenum} = \lambda_{fo} + \lambda_R \quad (\text{A.18})$$

The conductivity of the solid material λ_{fo} is very small in a hollow space, but it is still calculated because the volume fraction of solid material cannot be zero and the material is homogeneous.

A.1.3 Boundary Conditions Temperature Field Calculation

In boundary zones, wall boundary conditions are defined. The boundary zones are defined by a fluid zone. The heat flux q'' at a border of a fluid zone is defined by (Peterson, 1983):

$$q'' = \lambda_{bc} \left(\frac{\partial T}{\partial n} \right)_{bc} = h a_s (T_s - T_{bc}) \quad (\text{A.19})$$

Here T_s is the temperature of the solid state zone at a boundary, T_{bc} is the preset boundary zone, λ_{bc} is the heat condition in the boundary zone, a_s is the surface at the boundary and h is the given heat transport coefficient. With relation (A.19) two other boundary conditions can be simulated. When α is chosen close to zero ($1 \gg \alpha$), the fluid boundary zone simulates an adiabatic boundary, When α is chosen to be very large ($\alpha \gg 1$) a boundary with a constant temperature is simulated. It is also clarified with Figure 47. This is the boundary relation for convective heat transport to another medium.

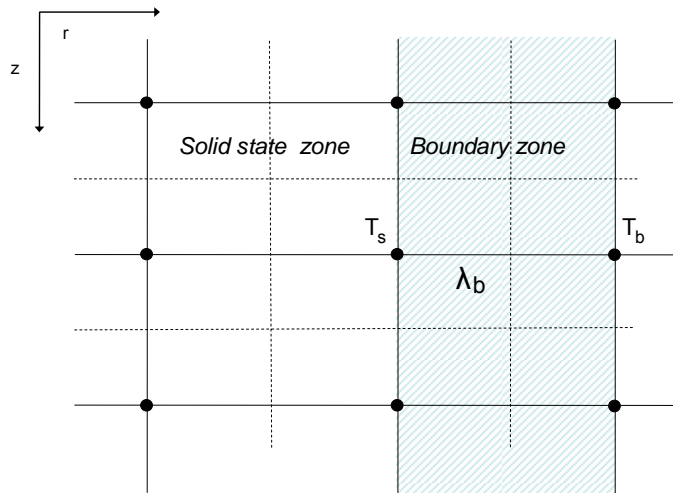


Figure 47. Boundary zone definition, T_b is a preset temperature and T_s the temperature at a boundary with the boundary zone. λ_b is calculated with equation (1.14).

With this relation two other boundary conditions can be simulated. When α is chosen close to zero ($1 \gg \alpha$), the boundary simulates an adiabatic boundary, When α is chosen to be very large ($\alpha \gg 1$) a boundary with a constant temperature is simulated.

A.2 Convection part of THERMIX, flow field and convective heat sources

When heat is transported not only by conduction but also convection, the convection program of THERMIX (DIREKTSR) is called. Starting with the solid state temperatures, calculated in the main program and convection boundary conditions, the (mass) flow field of the coolant and the coolant temperatures are calculated. From this information a convective heat source/sink distribution q_C is calculated, to simulate the convective heat transport of the coolant in the main program (see equation (A.1)).

The model used is a “geometric homogeneous two phase model” incorporated in a r-z cylindrical geometry. This means that in the model empirical relations are used to model the microscopic structure for flow resistance and heat transfer. The grid for convection

calculations is not necessarily the same size as the solid state grid. The size of the convection grid covers the area of the solid state grid, in which flow occurs. In the convection part four different regions can be defined (Verfondern, 1978):

1. the pebble bed (homogenized, isotropic and two dimensional flow)
2. perpendicular flow regions (homogenized, anisotropic, one dimensional flow)
3. fluid plenums (no pressure loss)
4. regions without flow

A.2.1 The (mass) flow field calculation

The structure of the subroutine DIREKTSR is shown in Figure 48. It was produced was after investigation of the source code of the program (Struth, 1998) and it shows an simple interpretation of the method used in THERMIX to calculate the coolant flow field and the convective heat sources/sinks field used in the solid state part of the program.

First the fluid properties of the coolant are calculated. Then the macroscopic mass flow and pressure fields are found by solving the continuity equation and the impulse balance equation. The flow is represented a macroscopic vector field of flow speed/mass flow and by a macroscopic pressure field within the pores of the homogenous solid material. These macroscopic fields are spatial averages of the quantities in the microscopic structure. The connection between both fields mutually takes place by empirical correlations.

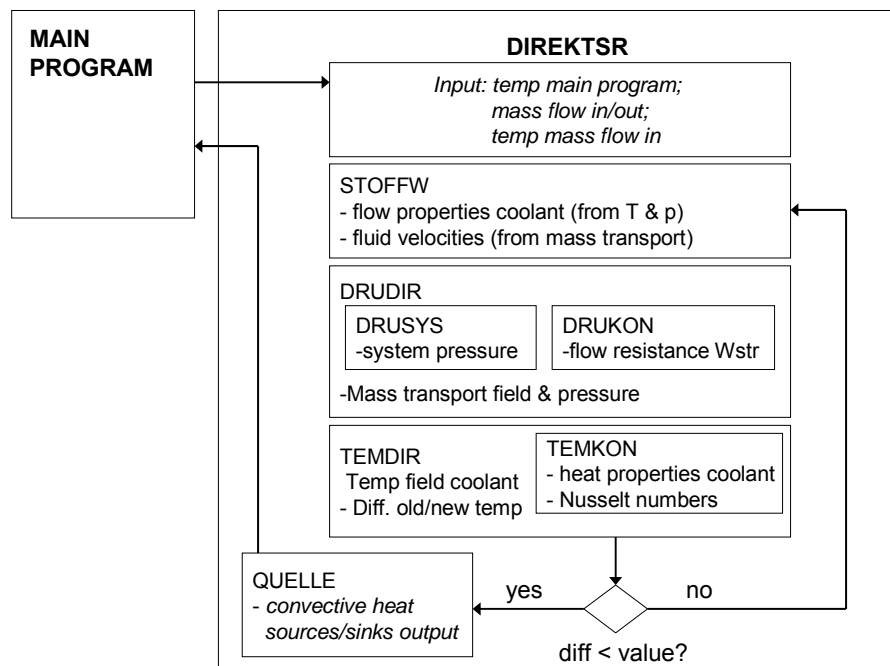


Figure 48. Simplified calculation flow chart of subroutine direktsr, the convection part of THERMIX

The continuity equation is given as (Banaschek, 1983):

$$\nabla \cdot \vec{G} = S_M \quad (\text{A.20})$$

here, S_M is a mass source or sink, \vec{G} is the mass flow density vector, the product of the velocity v and the density ρ .

$$\vec{G} = \rho \vec{v} \quad (\text{A.21})$$

The continuity equation is in cylindrical coordinates:

$$\frac{1}{r} \frac{\partial}{\partial r} (r G_r) + \frac{\partial}{\partial z} (G_z) = S_m \quad (\text{A.22})$$

with G_r and G_z components of the mass flow density \vec{G} . When integrated over a control volume, discretized in the flow model, the continuity equation is written as

$$\sum_{j=1}^4 \dot{m}_j + \dot{S}_m = 0 \quad (\text{A.23})$$

The discretization of the flow model is shown in Figure 49. (Peterson, 1983)

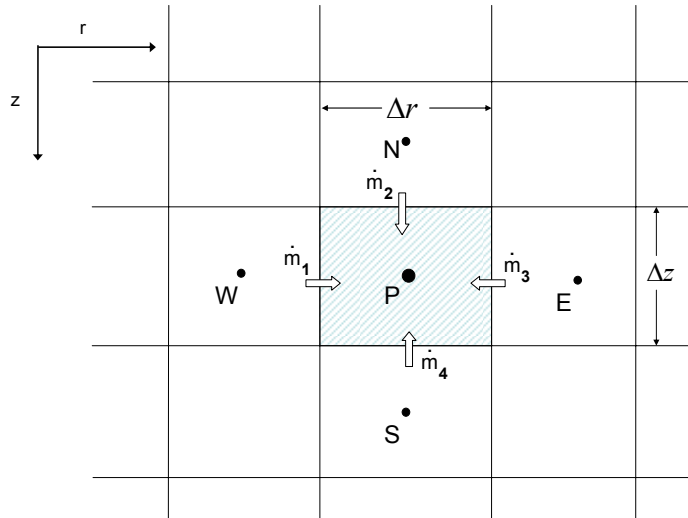


Figure 49. Discretization of the flow model

The impulse balance equation used in THERMIX is a balance between a pressure difference caused by an empirically determined flow friction term and gravitation (Banaschek, 1983).

$$\nabla p = -\vec{R} + \rho \vec{g} \quad (\text{A.24})$$

with

$$\bar{R} = \frac{\Psi}{d_p} \frac{1-\varepsilon}{\varepsilon^3} \frac{|\bar{G}|}{2\rho} (\bar{G}) \quad (\text{A.25})$$

here Ψ is a friction coefficient, ε the porosity of the bed and d_p the diameter of the pebbles used. In a pebble bed the friction coefficient Ψ is derived from the pressure drop over a pebble bed and given by (Kugeler and Schulten, 1998; Struth, 1998):

$$\Psi = \frac{320}{\text{Re}} + \frac{6}{\left(\frac{\text{Re}}{1-\varepsilon}\right)^{0.1}} \quad (\text{A.26})$$

This relation is valid through

$$1 \leq \frac{\text{Re}}{1-\varepsilon} \leq 10^5, \quad (\text{A.27})$$

$$0.36 \leq \varepsilon \leq 0.42$$

For other geometries other relations exist for the friction coefficient, these are not mentioned here. It can be noted that the impulse balance equation a highly simplified, empirical form of the Navier Stokes equation. Equation is discretized as

$$\dot{m} = \frac{\Delta p + (\rho g \Delta z)}{W_{str}} \quad (\text{A.28})$$

with, for example in the z-direction

$$W_{str} = \frac{\Psi}{d_p} \frac{1-\varepsilon}{\varepsilon^3} \frac{G}{2\rho} \frac{\Delta z}{a_z} \quad (\text{A.29})$$

here a_z is the surface through which the flow moves. When equation (A.28) is inserted in the continuity equation (A.23) a relation for the pressure field is found from which the mass flow can be calculated. After insertion of equation (A.28) and integration over the control volume the continuity equation reads:

$$\frac{p_W - p_P}{W_{str,1}} + \frac{p_N - p_P + (\rho g \Delta z)_2}{W_{str,2}} + \frac{p_E - p_P}{W_{str,3}} + \frac{p_S - p_P + (\rho g \Delta z)_4}{W_{str,4}} + S_{M_P} = 0 \quad (\text{A.30})$$

which can be rewritten to find the pressure in P:

$$p_P = \frac{\frac{p_W}{W_{str,1}} + \frac{p_N + (\rho g \Delta z)_2}{W_{str,2}} + \frac{p_E}{W_{str,3}} + \frac{p_S + (\rho g \Delta z)_4}{W_{str,4}} + S_{M_p}}{\sum_{j=1}^4 \frac{1}{W_{str,i}}} = 0 \quad (\text{A.31})$$

With the pressure field known all mass fluxes (and therefore also the velocity field) can be found with the separate impulse equations in the r and z direction.

A.2.2 The Coolant temperatures, convective heat sources

The next step in the convection part of the program is that the gas temperatures must be calculated. A (quasi) steady state heat balance is used that is dependent on the following heat transfer contributions (Peterson, 1983):

- convective heat transport from the flowing coolant (gas)
- diffusion heat flux
- the heat transport between the pebble surface and the coolant
- contribution to the heat transport by convective sinks or sources

The equation of the (quasi) steady state heat balance is then given as:

$$c_p \rho (\vec{v} \cdot \nabla) T_C = (\nabla \cdot \lambda_C \nabla T_C) + h a_s (T_S - T_C) + c_p S_M T_{S_M} \quad (\text{A.32})$$

Here T_C is the coolant temperature, T_S is the temperature of the pebble surface, T_{S_M} is the temperature of the coolant in a source or sink, c_p is the (constant) heat capacity of the coolant, ρ the density of the coolant, λ_C is the heat conductivity of the coolant, \vec{v} the velocity of the coolant, h is the convective heat transport coefficient and a_s the effective surface inside the volume element through which heat is transported. In cylindrical coordinates the balance equation reads:

$$\begin{aligned} & -c_p \rho \frac{1}{r} \frac{\partial}{\partial r} (r v_r T_C) - c_p \rho \frac{\partial}{\partial z} (r v_z T_C) + \frac{1}{r} \frac{\partial}{\partial r} \left(r \lambda_{C,r} \frac{\partial}{\partial r} T_C \right) \\ & + \frac{\partial}{\partial z} \left(\lambda_{C,z} \frac{\partial}{\partial z} T_C \right) + h a_s (T_S - T_C) + c_p S_M T_{S_M} = 0 \end{aligned} \quad (\text{A.33})$$

The first term in the balance equation, the convective heat transport, corresponds to the amount of heat transported away from or into the control volume through the faces of the control volume, see also Figure 49. When integrated over the control volume it reads:

$$\dot{m}_1 c_p (T_{C,W} - T_{C,P}) + \dot{m}_2 c_p (T_{C,N} - T_{C,P}) - \dot{m}_3 c_p (T_{C,E} - T_{C,P}) - \dot{m}_4 c_p (T_{C,S} - T_{C,P}) \quad (\text{A.34})$$

The heat conduction through the pebble bed, which is the second term in equation (A.32), is discretized and integrated over the control volume in the same way as shown for the solid material. In contradiction with the solid state model however, the heat conduction is anisotropic in the convection calculation. A different conduction coefficient is defined for conduction in the flow direction and perpendicular to the flow, because of an interweaving effect of the flow at a microscopic scale. How the conductivity is calculated exactly, could not be derived from information about THERMIX or the source code (Struth, 1998).

The calculation for the heat transport from the pebble surface to the coolant (which is the third term in equation(A.32)) deserves some extra attention. In the discretized and integrated numerical equation it is represented as:

$$ha_s(T_{S,P} - T_{C,P}) \quad (\text{A.35})$$

with $T_{S,P}$ the surface of temperature of the solid pebbles inside the control volume and $T_{C,P}$ the temperature of the coolant. This convective heat transport is communicated back to the conduction part of the program (the main program) as the q_C , the convective heat source or sink.

The relations, used to calculate the convective heat transport in the pebble bed, are shown here. The convective heat transport in other geometries is not covered. The surface F_s is the given by the surfaces of all pebbles inside the control volume (Verfondern, 1978; Struth, 1998):

$$a_s = N4\pi\left(\frac{d_p}{2}\right)^2 = \frac{V(1-\varepsilon)}{\frac{4}{3}\pi\left(\frac{d_p}{2}\right)^3}4\pi\left(\frac{d_p}{2}\right)^2 = \frac{V(1-\varepsilon)}{d_p}6 \quad (\text{A.36})$$

here, N is the number of pebbles inside the control volume, d_p the pebble diameter and V the volume of the control volume. The convective heat transport coefficient h is given by:

$$h = \frac{Nu\lambda_c}{d_p} \quad (\text{A.37})$$

here, Nu is the Nusselt number. The Nusselt number for the Pebble bed is calculated in THERMIX with two different empirical relations. The Nusselt number calculated with the method given in the VDI-wärmeatlas is (Struth, 1998):

$$Nu = (1 + 1.5(1 - \varepsilon)) \left(2 + (Nu_{lam}^2 + Nu_{tur}^2)^{\frac{1}{2}} \right)$$

$$Nu_{lam} = 0.664 Re^{\frac{1}{2}} Pr^{\frac{1}{3}} \quad (A.38)$$

$$Nu_{lam} = \frac{0.037 Re^{0.8} Pr}{1 + 2.443 Re^{0.1} \left(Pr^{\frac{2}{3}} - 1.0 \right)}$$

This relation is valid for

$$0.1 < Re < 10000.0 \quad (A.39)$$

The KTA definition of the Nusselt number (Peterson, 1983; Struth, 1998):

$$Nu = 1.27 \frac{Pr^{\frac{1}{3}}}{\varepsilon^{1.18}} Re^{0.36} + 0.033 \frac{Pr^{\frac{1}{2}}}{\varepsilon^{1.07}} Re^{0.86} \quad (A.40)$$

is valid for

$$100.0 < Re < 100000.0 \quad (A.41)$$

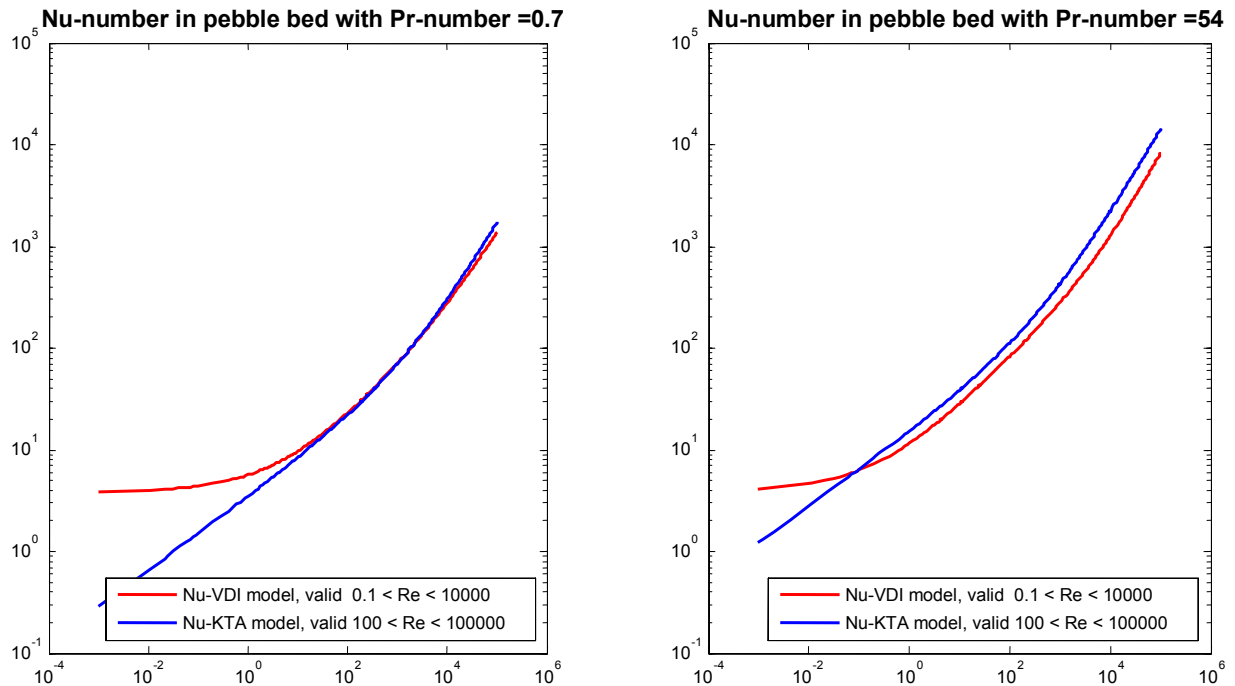


Figure 50. Nusselt numbers calculated for different Reynolds numbers with the VDI-empirical model and the KTA-empirical model. The Nusselt relations in the left picture are with $Pr = 0.7$, used for Helium. In the picture on the right, $Pr = 54$, which is the Pr-number for FLiBe at 950 °C.

After calculation of the Nusselt number with both methods, the largest Nusselt number is chosen. When the Reynolds number approaches zero, the VDI relation is the largest and used. The Prandtl number then approaches ~ 3.8 for all Prandtl numbers. The Nusselt relations used in THERMIX are empirical relations, usually used gases with low Prandtl numbers (0.7-1.0). When a liquid coolant is used the Prandtl-number is much higher (10-100). In the figure below, two relations for Nusselt numbers with different Prandtl numbers are shown. The Prandtl-number of 0.7 is a characteristic number for helium cooling and the Prandtl-number 54 is a characteristic Prandtl number for FliBe at 950 °C

A.3 Modifications of the source code of THERMIX for the application of Liquid Salt Cooling

Thermix was modified in the following subroutines/functions:

In the Main program

- subroutine : wkpt (the heat capacity calculations)
- subroutine : wkptex (shows the formulas used to calculate the heat capacity)
- subroutine : wlam (the heat conductivity calculations)
- subroutine : wlamex (output formulas used to calculate the heat conduction)

In the convection part of the program:

- function : dichte (density coolant)
- subroutine : einlk (read input of convectionpart)
- subroutine : stoffw (some properties are defined)

All modifications in the source code are accompanied with the comment “R3 liquid salt”, so the modifications can be easily checked or changed. The implementation of the coolant FliBe consisted of implementation of its thermal hydraulic properties as well as the implementation of it’s equation of state. The Fluid properties are listed below (Davis, 2005; Forsberg 2004).

Table 14. The properties of the liquid salt coolant FliBe. The properties were acquired from two articles on liquid salt applications (Forsberg, 2004 and Davis 2005) and appended to the THERMIX program.

<i>Property</i>		
Density ρ	$(kg/m^3), T(^{\circ}C), p(Pa)$	$(2279.7 - 0.4884 \cdot T)(1 + \kappa(p - p_0))$
reference p_0	(Pa)	$6.367 \cdot 10^4$
compressibility κ	$(1/Pa), T(K)$	$2.3 \cdot 10^{-11} \exp(0.001T)$
heat capacity c_p	(J/kgK)	2386
heat conductivity λ	(W/mK)	1.1
viscosity η	$(kg/ms), T(K)$	$0.000116 \cdot \exp(3755/T)$

In the THERMIX input, the use of the liquid salt coolant FliBe can be chosen. In the solid state part of the calculation, the coolant in the core has to be chosen in input line

“DI-F.10a”. In the convection part of the input the fluid must be chosen in input line “DI-K.7” The input for IFLUID in both the solid state part as the convection part of the program is 7 for FliBe. FliBe is also listed as material g07 in the heat capacity subroutine *wkpt* and the heat conductivity subroutine *wlam*.

A.4 Way-Wigner decay heat calculation (used in THERMIX)

In absence of neutron capture, the decay heat produced per fission can be described as a function of the decay time. The total decay heat function per fission event $f(t)$ is the sum of the contributions of the beta decay $b(t)$ and the gamma decay $g(t)$. If a fissile material is being irradiated for a time I with a constant neutron flux (a constant power), the decay heat at a time t' seconds following the irradiation can be calculated by regarding the irradiation as a series of fission bursts as shown in Figure 51. Fissions occur from time $t = 0$ until $t = I$.

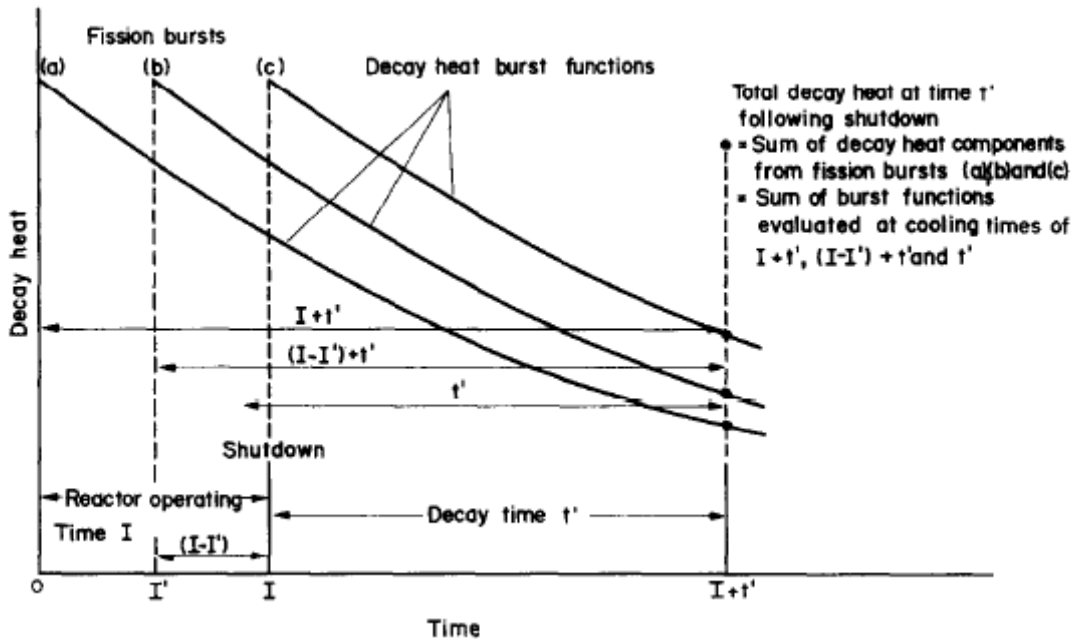


Figure 51. A finite irradiation representation by a series of fission bursts (Tobias, 1980).

The contribution to the beta decay power at time t' due to the normalized fission at $t = 0$ is given by $b(I + t')$ while the contribution to the beta decay power due to the normalized fission at $t = I$ is $b(t')$. The total beta decay power output is then given by (Tobias, 2000):

$$B(I, t') = \int_{t'}^{I+t'} b(t) dt \quad (\text{MeV} \cdot \text{fission}^{-1}) \quad (\text{A.42})$$

The same relation is valid for the gamma decay power and the total fission decay power. The beta decay power $b(t)$ and the gamma decay power $g(t)$ are given by respectively:

$$b(t) = 1.40 t^{-1.2} \quad (\text{MeV} \cdot \text{fission}^{-1}) \quad (\text{A.43})$$

$$g(t) = 1.26 t^{-1.2} \quad (\text{MeV} \cdot \text{fission}^{-1}) \quad (\text{A.44})$$

When $b(t)$ is inserted in equation (A.42) and then added to the corresponding equation for $g(t)$ the decay heat power after an operation time I is found. It is known as the Way-Wigner relation and given by (Kloosterman, 2000):

$$F(I, t) = \frac{2.66}{0.2} \left[t^{-0.2} - (t + I)^{-0.2} \right] \quad (\text{MeV} \cdot \text{fission}^{-1}) \quad (\text{A.45})$$

or expressed as a fraction of the total power of the reactor during operation:

$$F(I, t) = 0.066 \left[t^{-0.2} - (t + I)^{-0.2} \right] \quad (\text{A.46})$$

This relation is used in the thermal hydraulics code THERMIX to calculate the decay heat (Struth, 1998).

Appendix B. Even Parity Neutron Transport Code EVENT

The neutronics describe the transport of neutrons in the reactor. They are essential in describing the physical behavior of a nuclear reactor core. For example, the power profile is dictated by the neutronics and several feedback effects (like stability of a nuclear reactor) cannot be studied without knowledge of the neutronics. The distribution of neutrons in a reactor is investigated with by studying the process of neutron transport.

B.1 Neutron transport equation

The transport of neutrons in a system is described with the neutron transport equation. The neutron transport equation is found by balancing the various mechanisms by which neutrons can be gained or lost from an arbitrary volume V within the system. The gain mechanisms are (Duderstadt and Hamilton, 1976):

1. any neutron sources, including fission
2. neutrons streaming into V through the surface volume
3. neutrons of different energy's that enter the energy and direction of interest by a scattering collision

Neutron are lost by the following mechanisms

4. neutrons leaking out of the volume through the surface of the volume
5. neutrons in V suffering a collision (absorption and scattering)

In fact, mechanism 2 and 4 are the same, but each others opposite and are expressed by the same term in the equation. All effects are incorporated in the neutron transport equation. It is given by (Van Dam and Hoogenboom, 1998):

$$\frac{1}{v} \frac{\partial \phi(\mathbf{r}, E, \boldsymbol{\Omega}, t)}{\partial t} = S(\mathbf{r}, E, \boldsymbol{\Omega}, t) + \int_{\boldsymbol{\Omega}'} d\boldsymbol{\Omega}' \int_{E'} dE' \Sigma_s(\mathbf{r}, E' \rightarrow E, \boldsymbol{\Omega}' \rightarrow \boldsymbol{\Omega}, t) \phi(\mathbf{r}, E', \boldsymbol{\Omega}', t) - \boldsymbol{\Omega} \cdot \nabla \phi(\mathbf{r}, E, \boldsymbol{\Omega}, t) - \Sigma_t(\mathbf{r}, E) \phi(\mathbf{r}, E, \boldsymbol{\Omega}, t) \quad (\text{B.1})$$

here, v is the neutron velocity, $\phi(\mathbf{r}, E, \boldsymbol{\Omega}, t)$ is the angular flux density, E is the neutron energy, $\boldsymbol{\Omega}$ is the unit directional vector, $\Sigma_t(\mathbf{r}, E)$ is the total cross-section, $\Sigma_s(\mathbf{r}, E' \rightarrow E, \boldsymbol{\Omega}' \rightarrow \boldsymbol{\Omega}, t)$ is the scattering cross-section and $S(\mathbf{r}, E, \boldsymbol{\Omega}, t)$ is a neutron source, by fission or external, so:

$$S(\mathbf{r}, E, \boldsymbol{\Omega}, t) = S_{ext} + \chi(E) \int_{E'} \int_{\boldsymbol{\Omega}'} v(E') \Sigma_f(\mathbf{r}, E') \phi(\mathbf{r}, E, \boldsymbol{\Omega}, t) dE' d\boldsymbol{\Omega}' \quad (\text{B.2})$$

here S_{ext} is an external neutron source, $\chi(E)$ is the fission spectrum, v is the number of neutrons per fission and $\Sigma_f(E', \mathbf{r})$ is the fission cross section. This balance equation is

very hard to solve analytically, even in simple cases, therefore when neutronics are used in reactor physical simulations, one has to rely on computational methods. The neutronics of the reactor in this investigation are simulated with the code EVENT. To calculate solutions for neutron transport problems, EVENT uses a deterministic method (Oliveira, 1991).

The neutron transport equation is transformed into a set of linear equations by adopting the even parity method and the Ritz procedure. The computer code EVENT sets up these equations and solves the linear system.

B.2 Discretizations in EVENT

B.2.1 Multi group treatment

The energy dependence in the transport equation is discretized via the multi group approximation. The energy domain is partitioned into G intervals with ΔE_g , $g = 1, 2, \dots, G$ and equation (B.1) is integrated over ΔE_g . This results in (Oliveira, 1999):

$$\frac{1}{v} \frac{\partial \phi_g(\mathbf{r}, \boldsymbol{\Omega}, t)}{\partial t} + \boldsymbol{\Omega} \cdot \nabla \phi_g(\mathbf{r}, \boldsymbol{\Omega}, t) + \Sigma_{t,g}(\mathbf{r}) \phi_g(\mathbf{r}, \boldsymbol{\Omega}, t) - \int_{\boldsymbol{\Omega}'} d\boldsymbol{\Omega}' \sum_{g'=1}^G \Sigma_{s,g'g}(\mathbf{r}, \boldsymbol{\Omega}' \cdot \boldsymbol{\Omega}, t) \phi_g(\mathbf{r}, \boldsymbol{\Omega}', t) = S_g(\mathbf{r}, E, \boldsymbol{\Omega}, t) \quad , g = 1, 2, \dots, G \quad (\text{B.3})$$

here the source S_g is a external source or neutron source induced by fission:

$$S_g(\mathbf{r}, \boldsymbol{\Omega}, t) = S_{ext,g}(\mathbf{r}, \boldsymbol{\Omega}, t) + \frac{\chi_g}{4\pi} \sum_{g'=1}^G \nu \Sigma_{f,g'}(\mathbf{r}) \int_{\boldsymbol{\Omega}'} d\boldsymbol{\Omega}' \phi_{g'}(\mathbf{r}, \boldsymbol{\Omega}', t) \quad , g = 1, 2, \dots, G \quad (\text{B.4})$$

B.2.2 Time discretization

The time discretization is handled in the same way as shown in equation(A.7). Either implicit ($f = 1$), explicit ($f = 0$) or Crank Nicolson ($f = 0.5$) time integrating schemes are available in the EVENT code (Oliveira, 1999).

B.2.3 Angular discretization, spherical harmonics

Spherical harmonics functions are used to approximate the angular dependence of the flux. In the transport equation, the angular flux and the scattering cross-section are expanded in Legendre polynomials. The transport equation is then transformed in a set of $L+1$ equations with $L+2$ unknowns. After an approximation in the equation for $n = L$, the set of equations can be solved. The numerical implementation is general and there is no restriction on the order of the angular approximation (Boer, 2005; Oliveira 1999).

B.2.4 Spatial discretization, finite elements

The spatial variables are discretized by a finite element method. All spatial integrations are performed numerically.

B.3 Solution procedure, Even Parity method

The steady state and one group form of the neutron transport equation is given as follows:

$$\Omega \cdot \nabla \phi(\mathbf{r}, \Omega) + H\phi(\mathbf{r}, \Omega) = S(\mathbf{r}, \Omega) \quad (\text{B.5})$$

here the H is the collision operator and defined in terms of the total cross-section and the differential cross-section by [12]:

$$H\phi(\mathbf{r}, \Omega) = \Sigma_t(\mathbf{r})\phi(\mathbf{r}, \Omega) - \int_{\Omega'} d\Omega' \Sigma_s \phi(\mathbf{r}, \Omega') \quad (\text{B.6})$$

The neutron transport equation is solved using the even parity method. Therefore the transport equation must be written as a coupled pair of second order equations. The flux is described in its even & odd parity form as:

$$\phi^\pm = \frac{\phi(\mathbf{r}, \Omega) \pm \phi(\mathbf{r}, -\Omega)}{2} \quad (\text{B.7})$$

the even and odd parity form of the source is described as

$$S^\pm = \frac{S(\mathbf{r}, \Omega) \pm S(\mathbf{r}, -\Omega)}{2} \quad (\text{B.8})$$

The parity form of equation (B.5) is then given by

$$\Omega \cdot \nabla \phi^+ + C\phi^- = S^- \quad (\text{B.9})$$

$$\Omega \cdot \nabla \phi^- + G\phi^+ = S^- \quad (\text{B.10})$$

Here C and G are the even- and odd-parity components of the H operator. When equation (B.9) is entered in equation (B.10), the odd parity flux is eliminated. Now the equation to solve reads:

$$-\Omega \cdot \nabla G \Omega \cdot \nabla \phi^+ + C\phi^+ = S^+ - \Omega \cdot \nabla G S^- \quad (\text{B.11})$$

The solution of this equation is equivalent to finding the function which minimizes [12]

$$F[\phi] = (\mathbf{\Omega} \cdot \nabla \phi, G\mathbf{\Omega} \cdot \nabla \phi) + (\phi, C\phi) - 2(\phi, S^+) - 2(\mathbf{\Omega} \cdot \nabla \phi, GS^-) \quad (\text{B.12})$$

Approximate solutions are then obtained via the Ritz procedure. It uses the fact that finding the solution to the even parity equation is equivalent to the requirement that the first variation $F[\phi]$ must vanish. The even parity flux is approximated by:

$$\phi^+(\mathbf{r}, \mathbf{\Omega}) = \sum_{i=1}^M U(\mathbf{r}, \mathbf{\Omega}) \phi_i^+ = U^T \phi^+ \quad (\text{B.13})$$

Inserting this in equation (B.12) gives

$$F[\phi^+] = \phi^{+T} A \phi^+ - 2\phi^{+T} B \quad (\text{B.14})$$

with

$$\begin{aligned} A &= (\mathbf{\Omega} \cdot \nabla U^T, G\mathbf{\Omega} \cdot \nabla U) + (U, CU) \\ B &= (U^T, S^+) + (\mathbf{\Omega} \cdot \nabla U^T, GS^-) \end{aligned} \quad (\text{B.15})$$

The requirement that $\partial F[\phi^+] = 0$ leads to

$$A\phi^+ = B \quad (\text{B.16})$$

By adopting the even parity method and the Ritz procedure to the neutron transport equation, the equation is thus transformed into a set of linear equations. The computer code EVENT sets up these equations and solves the linear system.

Appendix C. The Thermal Hydraulics code HEAT

C.1 Momentum equation used in HEAT

The velocity field calculation is solved by solving the continuity equation and the momentum equation. The momentum equation in the code HEAT is given by (Lathouwers and Bellan, 2001):

$$\frac{\partial(\varepsilon\rho_C\mathbf{u})}{\partial t} + \nabla \cdot (\varepsilon\rho_C\mathbf{u}\mathbf{u}) = -\frac{(1-\varepsilon)\rho_p}{\tau_{12}}\mathbf{u} + \nabla \cdot \varepsilon\bar{\mathbf{T}} + \varepsilon\rho_C\mathbf{g} \quad (\text{C.1})$$

In this momentum equation \mathbf{u} is the velocity of the coolant, ε is the volume fraction of the coolant, ρ_C is the density of the coolant, ρ_p is the density of the fuel pebbles, \mathbf{g} is the gravity, $\bar{\mathbf{T}}$ is the stress tensor and τ_{12} is the particle-coolant interaction time scale.

For clarification, in the above equation the terms are from left to right: the local time rate of change, convective transport, friction drag force caused by the particles in the packed bed, the viscous stress, the pressure difference and molecular transport and the effect of gravity. The stress tensor $\bar{\mathbf{T}}$ is given for Newtonian fluids by:

$$\bar{\mathbf{T}} = \left(-p + \frac{2}{3}\mu\nabla \cdot \mathbf{u} \right) \bar{\mathbf{I}} + \mu(\nabla\mathbf{u} + (\nabla\mathbf{u})^T) \quad (\text{C.2})$$

Here, p is the static pressure, μ is the dynamic viscosity and $\bar{\mathbf{I}}$ is the unit tensor. The particle-coolant interaction time scale (or friction force) τ_{12} is given by:

$$\frac{1}{\tau_{12}} = \frac{\rho_C}{\rho_p} \left[\varepsilon \frac{150}{\text{Re}_p} + 1.75 \right] \quad (\text{C.3})$$

with

$$\text{Re}_p = \varepsilon \frac{\rho_C d_p \mathbf{u}}{\mu} \quad (\text{C.4})$$

The friction drag force is here defined for porous media with very small particles. In THERMIX a friction drag force term is given by equation (A.25). This relation is derived for pebbles with larger sizes and is valid over a large range of Reynolds numbers. Therefore this relation was implemented in the code HEAT. The friction drag force in the momentum equation was changed into:

$$-\frac{(1-\varepsilon)\rho_p}{\tau_{12}}\mathbf{u} = -\varepsilon\bar{R} = -\varepsilon \frac{\Psi}{d_p} \frac{\varepsilon}{\varepsilon^3} \frac{|\varepsilon\rho_C\mathbf{u}|}{2\rho_C} \varepsilon\rho_C\mathbf{u} \quad (\text{C.5})$$

The right term of the equation is equation (A.25) multiplied by the volume fraction for the coolant ε . Here Ψ is the friction coefficient which is given by equation (3.6). In HEAT this change was implemented by changing the particle-coolant interaction time scale τ_{12} . Equation (C.5) was derived to:

$$\frac{1}{\tau_{12}} = \frac{\rho_c}{\rho_p} \frac{\Psi}{d_p} \frac{|\mathbf{u}|}{2} \quad (\text{C.6})$$

This relation is then used in the momentum equation (C.1) instead of the relation described in equation (C.3).

C.2 Energy equations

The energy fields are described by three energy balances. For the coolant the energy equation is:

$$\varepsilon \rho_c c_{p,g} \frac{DT_c}{Dt} = \nabla \cdot [\varepsilon \lambda_c \nabla T_c] + h_{pg} a_{pg} [T_p - T_c] \quad (\text{C.7})$$

Here c_p is the heat capacity, T is the temperature, λ is the conductivity, h_{pg} is the heat transfer coefficient between the coolant and the pebbles and a_{pg} is the interfacial surface per unit volume of the solid particles. For the solid phase inside the core the energy balance is

$$\alpha_p \rho_p c_{p,p} \frac{DT}{Dt} = -h_{pg} a_{pg} [T_p - T_g] + P_d \quad (\text{C.8})$$

Here P_d is a volumetric heat source, in this case the decay heat. It is assumed that there is no conduction between the separate pebbles and that there is no heat transfer between pebbles by radiation. In fact, the pebbles only transfer heat to the coolant by convective heat transfer. This assumption is correct if the convective heat transfer between salt and solid material is the dominant heat transfer mechanism. It is also a conservative assumption, so results of the calculation will not give an overestimation of the capacity to transfer heat from the core. The heat transfer coefficient h is given by

$$h_{p,g} = \frac{\text{Nu} \lambda_g}{d_p} \quad (\text{C.9})$$

with

$$\text{Nu} = 2 + 0.66 \text{Re}_p^{\frac{1}{2}} \text{Pr}_p^{\frac{1}{3}} \quad (\text{C.10})$$

here, Re is the Reynolds number and Pr the Prandtl number.

For the solid phase inside the reflector the energy equation is

$$\rho_{refl} c_{p,refl} \frac{\partial T_{refl}}{\partial t} = \nabla \cdot [\lambda_{refl} T_{refl}] \quad (C.11)$$

where the subscript *refl* stands for the reflector.

C.3 HEAT Boundary conditions

Since the model is a cylindrical symmetric model with a r-z geometry, the center of the model (at $r = 0$) has the following boundary conditions:

- no flow across the center boundary
- no scalar flux across the center boundary

The boundary condition between the core and the graphite reflector is given by a wall function which describes the flow close to wall influenced by the turbulent core, a buffer layer and a turbulent core (Agung, 2005).

The boundary heat flux in the bottom wall of the reactor is given by a constant temperature ($T_{wall} = T$).

The boundary heat flux in the other outer walls (the top and side of the reflector) is obtained from a natural convection heat flux and a heat flux from thermal radiation

$$q_{boundary} = q_{conv} + q_{rad} \quad (C.12)$$

The convective heat flux at the boundary is given by

$$q_{conv} = h_w (T_{refl} - T_\infty) \quad (C.13)$$

with

$$h_w = \frac{Nu_w \lambda_{air}}{H} \quad (C.14)$$

here, λ_{air} is the conductivity of air, H is the total height of the reactor model and Nu_w is the Nusselt number for free – convection, given by (Janssen and Warmoeskerken, 1991) :

$$Nu_w = \begin{cases} 0.13 Ra^{\frac{1}{3}}, & \text{for a vertical cylinder} \\ 0.14 Ra^{\frac{1}{4}}, & \text{for a horizontal plane} \end{cases} \quad (C.15)$$

The Rayleigh number Ra is defined as

$$\text{Ra} = \text{Gr Pr} = \frac{g \beta_{air} L^3}{\mu_{air}^2} (T_w - T_\infty) \text{Pr} \quad (\text{C.16})$$

here g is the acceleration of gravitation, β_{air} is the expansion coefficient of air and μ_{air} is the dynamic viscosity of air. L is a characteristic length, that is, the total length of the reactor model at the side boundary and the diameter of the top surface.

The thermal radiation heat flux q_{rad} is given by:

$$q_{rad} = \varepsilon c_s (T_w^4 - T_\infty^4) \quad (\text{C.17})$$

with the emissivity ε and the Stefan-Boltzmann constant c_s .

Appendix D, Cross Sections of Salt Constituents, Macroscopic Scattering Cross-Sections of Candidate Salts and Carbon

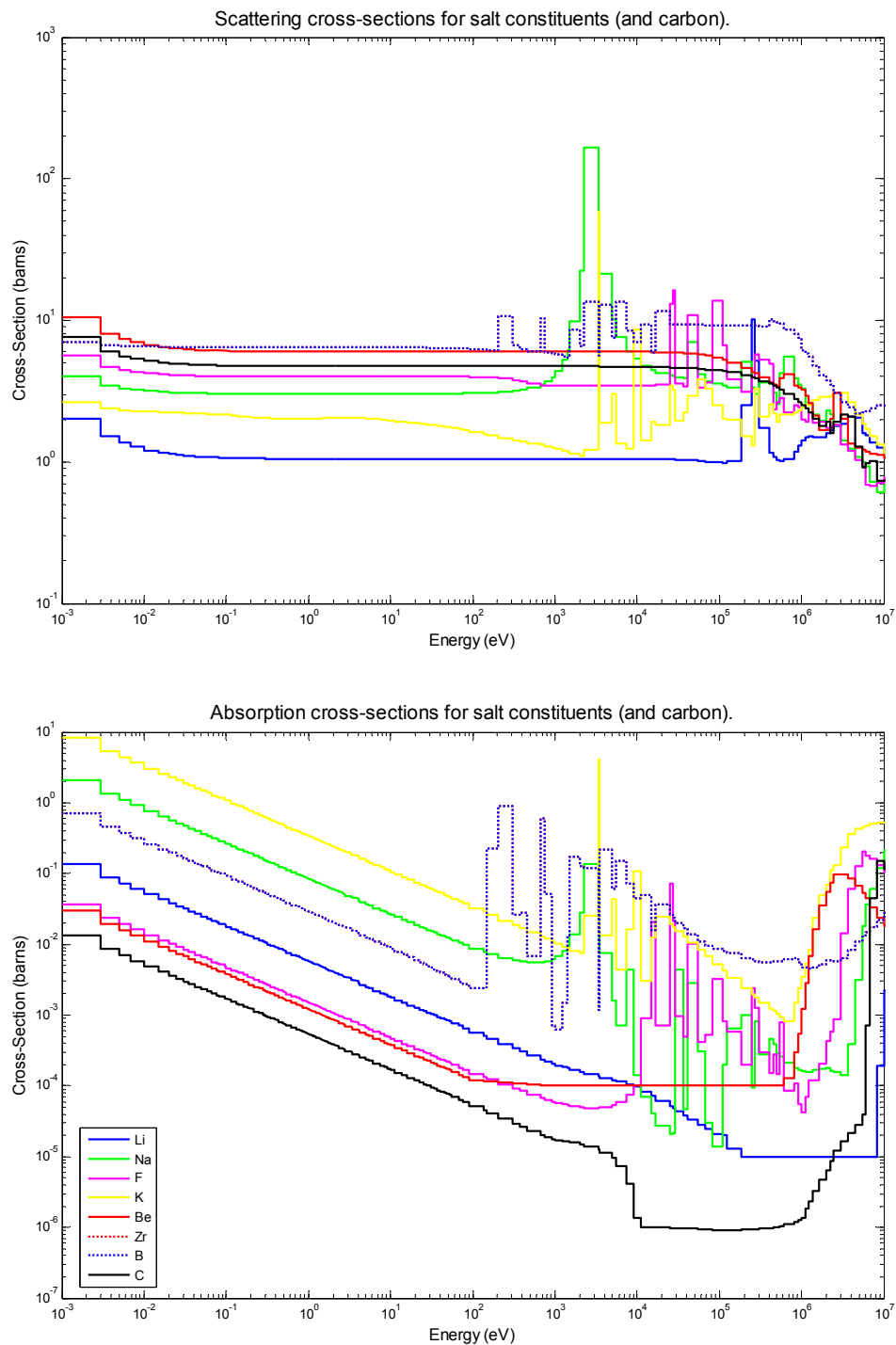


Figure 52. Scattering and absorption cross-sections salt constituents and carbon

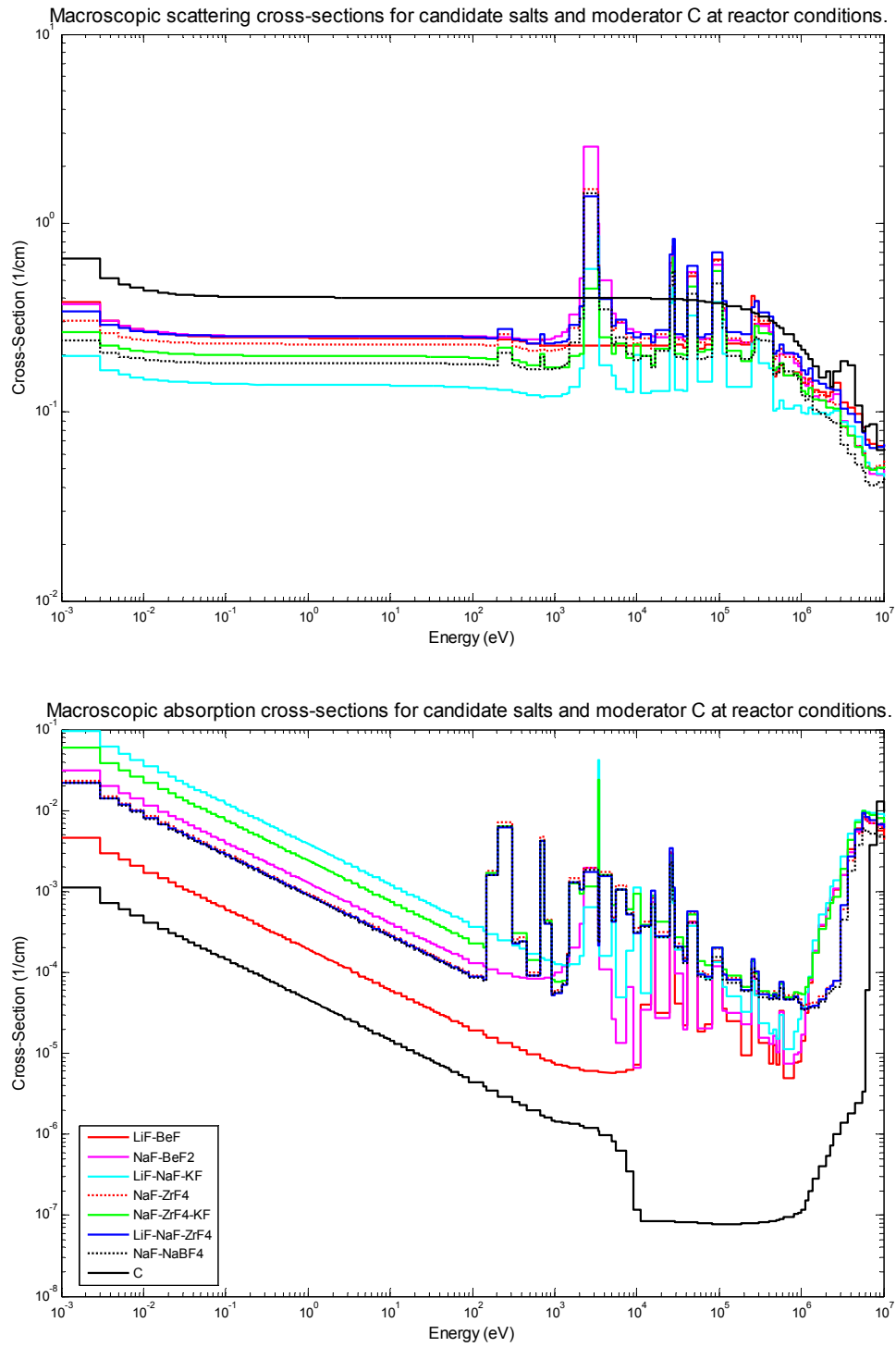


Figure 53. Macroscopic scattering and absorption cross-sections for candidate salts and Carbon

Appendix E. THERMIX and EVENT input for the cylindrical and the annular LSPBR

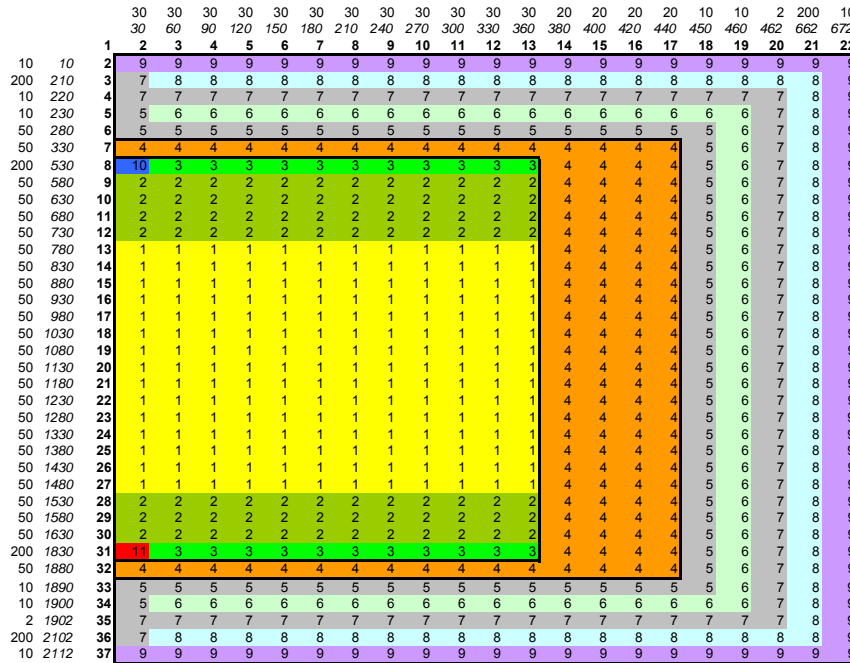
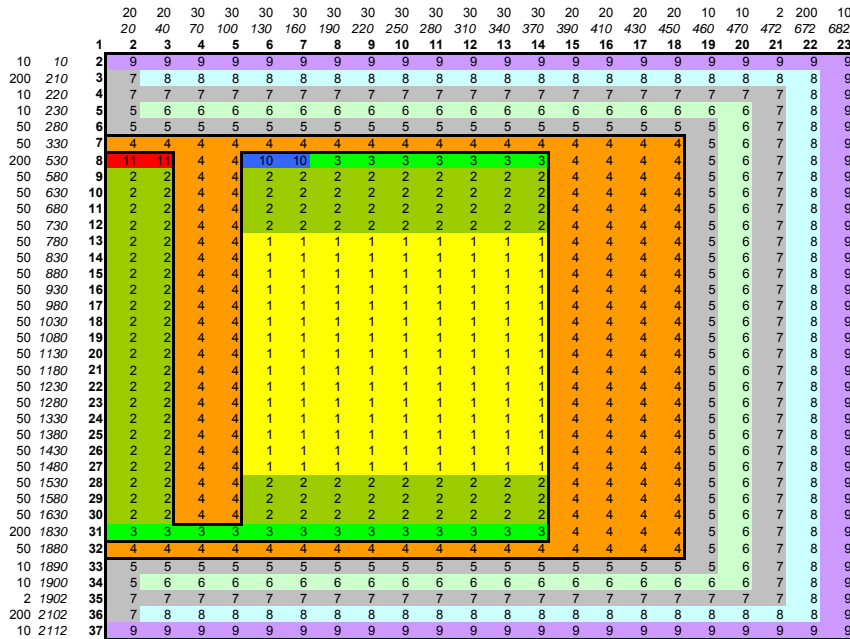


Figure 54. THERMIX and EVENT model of the cylindrical LSPBR



- Material specifications**
- 1 core region *
 - 2 top and bottom reflector (pipes) *
 - 3 salt plenum *
 - 4 graphite reflector region *
 - 5 vessel
 - 6 argon gap
 - 7 reactor guard vessel
 - 8 air outside reactor guard vessel
 - 9 boundary zone
 - 10 Inlet plenum
 - 11 outlet plenum

Figure 55. THERMIX and EVENT model for annular LSPBR (* materials used for neutronics)

Nomenclature

List of symbols

a	amplitude of fission spectrum	[-]
a_s	surface of boundary cell, surface of pebbles in pebble bed	[m ²]
A	atomic mass number	[u]
A	axial surface of the pebble bed	[m ²]
E	neutron energy	[eV]
c_s	constant of Stefan-Boltzmann	[W m ⁻² K ⁻⁴]
c_p	heat capacity	[J kg ⁻¹ K ⁻¹]
d	distance	[m]
d_p	diameter pebble	[m]
D	diameter of the core	[m]
\vec{G}	mass flow density vector	[kg s ⁻¹ m ⁻²]
H	height pebble bed	[m]
h	heat transfer coefficient	[W m ⁻² K ⁻¹]
k_∞	k-infinity	[-]
k-eff	k-effective	[-]
\dot{m}	mass flow	[kg s ⁻¹]
N	number of pebbles inside the control volume	[-]
N_{Li}	concentration of ⁶ Li	[wt %]
P	total power in the pebble bed core	[W]
q	power density	[W m ⁻³]
q_{fis}	fission power density in fuel zone	[W m ⁻³]
q''	heat flux	[W m ⁻²]
R	radius	[m]
\vec{R}	friction caused by pebble bed	[kg s ⁻² m ⁻²]
S_M	mass source or sink	[kg s ⁻¹ m ⁻²]
T	temperature	[K, °C]
v_0	velocity of coolant through the core	[m s ⁻¹]
\vec{v}	velocity of coolant	[m s ⁻¹]
W_{pump}	pumping power	[W, J s ⁻¹]
β	expansion coefficient	[K ⁻¹]
ε	emissivity	[-]
ε	porosity (coolant volume fraction)	[-]
η_{max}	Carnot efficiency	[-]
ϕ	neutron flux	[m ⁻²]
λ	conductivity	[W m ⁻¹ K ⁻¹]
μ	dynamic viscosity	[kg s ⁻¹ m ⁻¹]
ν	the number of neutrons per fission	[-]
ρ	density	[kg m ⁻³]
σ_s	microscopic scattering cross section	[barn]
σ_a	microscopic absorption cross section	[barn]

σ_t	microscopic total cross section	[barn]
Σ_s	scattering cross section	[barn]
Σ_a	absorption cross section	[barn]
Σ_t	total cross section	[barn]
Ψ	friction factor	[-]
χ	fission spectrum	[-]
ζ	lethargy gain	[-]

subscripts

F	fuel zone
G	graphite zone
S	surface of fuel
R	radiation
C	coolant
N	nuclear
C	from coolant (by convection)

dimensionless numbers (Janssen and Warmoeskerken, 1991)

Re	Reynolds number	$\frac{\text{inertia forces}}{\text{viscous forces}}$
Nu	Nusselt number	$\frac{\text{total heat transfer}}{\text{conductive heat transfer}}$
Pr	Prandtl number	$\frac{\text{hydrodynamic boundary layer thickness}}{\text{thermal boundary layer thickness}}$
Gr	Grashoff number	$\frac{\text{buoyancy forces}}{\text{viscose forces}}$
Ra	Rayleigh number	$\frac{\text{inertia forces}}{\text{surface tension forces}}$

References

- Agung, A. (2005) *Passive Removal of Post-Shutdown Decay Heat* Chapter 6 of Draft Ph.D. Thesis, Delft University of Technology, the Netherlands.
- Van den Akker H.E.A. and Mudde, R.F. (1996) *Fysische Transport verschijnselen I* Delft University Press, Delft, The Netherlands ISBN 90-407-1204-2.
- Banaschek, J. (1983) *Computation Methods and Analysis on the Dynamic Behaviour of Power Plants with High Temperature Gas Cooled Reactor*. Kernforschungsanlage Julich GmbH, Julich, Germany.
- Bende, E.E. et al. (1999) *Analytical calculation of the average Dancoff factor for a fuel kernel*. Nuclear Science and Engineering, 133(2), 147-162.
- Boer, B. (2004) *Feasibility of a High Temperature Nuclear Reactor as back up system for Wind Power* Faculty of Design, construction and Production, Delft University of Technology, The Netherlands. Report no. ET 2150
- Boer, B. (2005) *The Very High Temperature Reactor*, PNR, Delft University of Technology, The Netherlands PNR-131-2005-005
- Brown, L.C., Funk, J.F. and Showalter, S.F. (2000) *High efficiency generation of hydrogen fields using nuclear power*. GA-A23451, General Atomics Corp., San Diego, California.
- Van Dam, H, Hoogenboom, J.E. (1998) *Kernreactorkunde, collegedictaat tn391*, University of Technology, TNW, the Netherlands.
- Davis C.B. (2005) *Implementation of Molten Salt Properties into RELAP5-3D/ATHENA*, INEEL/EXT-05-02658
- DIN (1990) *Berechnung der Nachzerfallsleitung der Kernbrennstoffe von Hochtemperaturreactoren mit kugelförmigen Brennelementen*. Technical Report DIN 25 485 Deutsches institut für Normung e.V.
- Duderstad J.J. and Hamilton L.J. (1976) *Nuclear Reactor Analysis* John Wiley and Sons, Inc. ISBN 0-471-22363-8.
- Forsberg, C.W. (2004) *Reactors with Molten Salts: Options and Missions* Oak Ridge National Laboratory, USA.
- Forsberg C.W., Peterson P.F., Pickard P.S. et. al.(2004) *Status of the Preconceptual design of the Advanced High-Temperature Reactor (AHTR)*. ORNL/TM-2004/104, Oak Ridge National Laboratory, USA.

- Hoogendoorn, C.J. and Van der Meer, T.H. (1978) *Fysische Transportverschijnselen II*, Delftse Uitgevers Maatschappij, 1978 ISBN 90-6562-059-1.
- Janssen, L.P.B.M. and Warmoekserken, M.M.C.G. (1991) *Transport Phenomena Data Companion*. Delftse Uitgevers Maatschappij b.v. ISBN 90 6562074 5.
- Kloosterman, J.L. (2000) *Decay Heat Predictions: Experiments, Methods and Data, Integral Validation and Decay Heat Standards*. IRI-131-2000-005, Frederic Joliot and Otto Hahn Summer School, Cadarache, France.
- Kugeler, K. and Schulten, R. (1989) *Hochtemperaturreaktortechnik*, Springer-Verlag 1989, ISBN3-540-51535-6.
- Lathouwers, D. and Bellan, J. (2001) *Modeling of Dense Gas-Solid Reactive Mixtures Applied to Biomass Pyrolysis in a Fluidized Bed*. Int. J. Multiphase Flow, 27:2155.
- Moran M.J. and Shapiro, H.N. (1998). *Fundamentals of Engineering Thermodynamics, 3rd edition*. John Wiley & Sons Ltd, England, ISBN 0-471-97960-0
- Oliveira, C.R.E de (1991) *Finite Element Techniques for Multi Group Neutron Transport Equations with Anisotropic Scattering*. Phd Thesis, Imperial college of Science, University of London, United Kingdom.
- Oliveira, C.R.E de (1999) *EVENT A Multi Group, Finite Element-Spherical Harmonics Program for the Solution of Steady State and Time-Dependent Radiation Transport Problem in Arbitrary Geometry, User Notes and Program Listing*, Imperial college of Science, University of London, United Kingdom.
- Panaktar S.V. (1980) *Numerical Heat Transfer and Fluid Flow*, ISBN 0-89116-522-3
- Peterson K. (1983) *To the safety Conception of the High Temperature Reactor with Natural Heat Removal Decay in the case of Accidents*, Kernforschungsanlage Julich GmbH IRE, Germany.
- Pfennig, G. Klewe-Nebius, H. Seelmann-Eggebert, W. (1998) *Karlsruher Nuclidkarte 6th edition, revised reprint*, Forschungszentrum Karlsruhe GmbH, Karlsruhe, Germany
- Report on Green Paper,(2005) *Report on the Green Paper on Energy- Four Years of European Initiatives*. Energy and Transport DG, European Commission, Brussels, ISBN 92-894-8419-5.
- Roadmap Generation IV (2002) *A Technology Roadmap for Generation IV Nuclear Energy Systems, Technical Roadmap Report*. US DOE Nuclear Energy Research Advisory Committee and the Generation IV International Forum GIF-002-00.

Struth, S. (1998) *Instationaeres rechenmodell zur simulation des dynamischen verhaltens von hochtemperaturreaktoren waehrend des normalbetriebes und bei stoerfaellen*. Source code DIREKT-THERMIX, Julich GmbH, Julich, Germany.

Tobias, A. (1980) *Decay Heat*. Progress in Nuclear Energy Volume 5, 1-93.

Verfondern, K. (1978) *Experimentelle Überprüfung des thermohydraulikprogramms 'THERMIX' und rechnerische Analyse der transienten Temperatur- und Strömungsfelder im Core- Bereich des THTR- Reaktors nach Ausfall der Nachwärme abfuhr*. Technical Report KFA-IRE-IB-13/78, Forschungszentrum Julich GmbH, Julich, Germany.

Williams D.F. (2004) *Fuels for the Very High Temperature Reactor*. The F. Joliot and O. Hahn Summer School, Cadarache, France, (2004).